



Defense Threat Reduction Agency
8725 John J. Kingman Road, MS
6201 Fort Belvoir, VA 22060-6201



DTRA-TR-15-33

TECHNICAL REPORT

Li-Ion Batteries for Forensic Neutron Dosimetry

Distribution Statement A. Approved for public release, distribution is unlimited.

March 2016

DTRA1-11-1-0028

Erik B. Johnson

Prepared by:
Radiation Monitoring Devices,
Inc.
44 Hunt Street
Watertown, MA 01721

DESTRUCTION NOTICE:

Destroy this report when it is no longer needed.
Do not return to sender.

PLEASE NOTIFY THE DEFENSE THREAT REDUCTION
AGENCY, ATTN: DTRIAC/ J9STT, 8725 JOHN J. KINGMAN ROAD,
MS-6201, FT BELVOIR, VA 22060-6201, IF YOUR ADDRESS
IS INCORRECT, IF YOU WISH IT DELETED FROM THE
DISTRIBUTION LIST, OR IF THE ADDRESSEE IS NO
LONGER EMPLOYED BY YOUR ORGANIZATION.

REPORT DOCUMENTATION PAGE				<i>Form Approved</i> <i>OMB No. 0704-0188</i>	
<small>Public reporting burden for this collection of information is estimated to average 1 hour per response, including the time for reviewing instructions, searching existing data sources, gathering and maintaining the data needed, and completing and reviewing this collection of information. Send comments regarding this burden estimate or any other aspect of this collection of information, including suggestions for reducing this burden to Department of Defense, Washington Headquarters Services, Directorate for Information Operations and Reports (0704-0188), 1215 Jefferson Davis Highway, Suite 1204, Arlington, VA 22202-4302. Respondents should be aware that notwithstanding any other provision of law, no person shall be subject to any penalty for failing to comply with a collection of information if it does not display a currently valid OMB control number. PLEASE DO NOT RETURN YOUR FORM TO THE ABOVE ADDRESS.</small>					
1. REPORT DATE (DD-MM-YYYY)		2. REPORT TYPE		3. DATES COVERED (From - To)	
4. TITLE AND SUBTITLE				5a. CONTRACT NUMBER	
				5b. GRANT NUMBER	
				5c. PROGRAM ELEMENT NUMBER	
6. AUTHOR(S)				5d. PROJECT NUMBER	
				5e. TASK NUMBER	
				5f. WORK UNIT NUMBER	
7. PERFORMING ORGANIZATION NAME(S) AND ADDRESS(ES)				8. PERFORMING ORGANIZATION REPORT NUMBER	
9. SPONSORING / MONITORING AGENCY NAME(S) AND ADDRESS(ES)				10. SPONSOR/MONITOR'S ACRONYM(S)	
				11. SPONSOR/MONITOR'S REPORT NUMBER(S)	
12. DISTRIBUTION / AVAILABILITY STATEMENT					
13. SUPPLEMENTARY NOTES					
14. ABSTRACT					
15. SUBJECT TERMS					
16. SECURITY CLASSIFICATION OF:			17. LIMITATION OF ABSTRACT	18. NUMBER OF PAGES	19a. NAME OF RESPONSIBLE PERSON
a. REPORT	b. ABSTRACT	c. THIS PAGE			19b. TELEPHONE NUMBER (include area code)

UNIT CONVERSION TABLE

U.S. customary units to and from international units of measurement^{*}

U.S. Customary Units	<div style="display: flex; align-items: center; justify-content: center;"> <div style="margin-right: 10px;"> </div> Multiply by </div> <div style="display: flex; align-items: center; justify-content: center;"> <div style="margin-right: 10px;"> </div> Divide by[†] </div>	International Units
Length/Area/Volume		
inch (in)	2.54 × 10 ⁻²	meter (m)
foot (ft)	3.048 × 10 ⁻¹	meter (m)
yard (yd)	9.144 × 10 ⁻¹	meter (m)
mile (mi, international)	1.609 344 × 10 ³	meter (m)
mile (nmi, nautical, U.S.)	1.852 × 10 ³	meter (m)
barn (b)	1 × 10 ⁻²⁸	square meter (m ²)
gallon (gal, U.S. liquid)	3.785 412 × 10 ⁻³	cubic meter (m ³)
cubic foot (ft ³)	2.831 685 × 10 ⁻²	cubic meter (m ³)
Mass/Density		
pound (lb)	4.535 924 × 10 ⁻¹	kilogram (kg)
unified atomic mass unit (amu)	1.660 539 × 10 ⁻²⁷	kilogram (kg)
pound-mass per cubic foot (lb ft ⁻³)	1.601 846 × 10 ¹	kilogram per cubic meter (kg m ⁻³)
pound-force (lbf avoirdupois)	4.448 222	newton (N)
Energy/Work/Power		
electron volt (eV)	1.602 177 × 10 ⁻¹⁹	joule (J)
erg	1 × 10 ⁻⁷	joule (J)
kiloton (kt) (TNT equivalent)	4.184 × 10 ¹²	joule (J)
British thermal unit (Btu) (thermochemical)	1.054 350 × 10 ³	joule (J)
foot-pound-force (ft lbf)	1.355 818	joule (J)
calorie (cal) (thermochemical)	4.184	joule (J)
Pressure		
atmosphere (atm)	1.013 250 × 10 ⁵	pascal (Pa)
pound force per square inch (psi)	6.984 757 × 10 ³	pascal (Pa)
Temperature		
degree Fahrenheit (°F)	[T(°F) - 32]/1.8	degree Celsius (°C)
degree Fahrenheit (°F)	[T(°F) + 459.67]/1.8	kelvin (K)
Radiation		
curie (Ci) [activity of radionuclides]	3.7 × 10 ¹⁰	per second (s ⁻¹) [becquerel (Bq)]
roentgen (R) [air exposure]	2.579 760 × 10 ⁻⁴	coulomb per kilogram (C kg ⁻¹)
rad [absorbed dose]	1 × 10 ⁻²	joule per kilogram (J kg ⁻¹) [gray (Gy)]
rem [equivalent and effective dose]	1 × 10 ⁻²	joule per kilogram (J kg ⁻¹) [sievert (Sv)]

^{*} Specific details regarding the implementation of SI units may be viewed at <http://www.bipm.org/en/si/>.

[†] Multiply the U.S. customary unit by the factor to get the international unit. Divide the international unit by the factor to get the U.S. customary unit.

Executive Summary

Lithium-ion batteries are the common technology for powering portable electronics. The nuclear reactions within the batteries are sensitive to neutrons. By characterizing this dependence, neutron dose and fluence information can be determined. The dose information can be used on an individual basis to provide forensic information including evidence for exposure to special nuclear material or on a broad geographic scale, mapping out exposure conditions after a catastrophic nuclear event.

The goals of the program primarily focus on the correlations of the incident neutron spectrum to isotopic and chemical changes within the battery. These changes can be determined by mass spectrometry or gamma and beta spectroscopy of long-lived radioactive elements created from neutron interactions. The following provides the points to be addressed under this research:

- Identify correlation between exposure and nuclear changes in lithium batteries,
- Clarify potential means for read out of nuclear reactions for assessing neutron fluence, and
- Provide means for reconstructing the incident neutron spectrum.

The objectives of the program have changed very slightly in that any electronics will not be considered in the program, as the lithium batteries consist of sufficient materials to provide spectroscopic information.

Nuclear forensics are the methods used to determine the cause and means of a nuclear weapon. The world is progressing toward more proliferation, while countries with nuclear weapons that ratified the Treaty on the Non-Proliferation of Nuclear Weapons, such as the United States of America and the Russian Federation, are reducing their stockpiles. Nuclear forensics ideally should provide sufficient information for providing proper attribution of the nuclear weapon, by identifying the type, construction, and manufacturing of the weapon. This offers a deterrent for the manufacture and deployment of weapons, and the distribution of methods, materials and equipment for the manufacture of nuclear weapons.

The lithium battery consists of ${}^6\text{Li}$, which has a large thermal neutron cross section resulting in tritium. This was the primary reason why the lithium battery was selected for review in determining its feasibility for nuclear forensics. The following points summarize the major findings of the research:

- A significant drawback to neutron capture via lithium ions is tritium requires extraction from the battery such that it can be measured. This research program provides a method for tritium extraction.
- A major benefit of lithium batteries is that they are layers of metals within a sealed package. This is true for all batteries, yet this research focused on lithium batteries. The layering of the metals within a thin battery, such as a CR2023, provides a reasonable approximation of activation foils.
- The research shows that batteries can be used for spectral reconstruction using deterministic modelling.
- Significant data were collected on the batteries regarding their chemical makeup and induced activation after exposure to neutrons from reactor facilities. MCNP (Monte Carlo N Particle) models were used to demonstrate within a factor of four comparable activities of produced radioisotopes between simulations and measured data, validating modeling conclusions.
- The ratio of the ${}^{24}\text{Na}$ to ${}^{58}\text{Co}$ measured activities is an indicator of the incident neutron spectrum hardness, i.e. the spectrum has a high percentage of energetic neutrons.
- Through an MCNP simulation, a similar measurement of the ${}^{24}\text{Na}$ to ${}^{51}\text{Cr}$ as a function of distance can provide information on the spectral hardness.
- A key outcome done using MCNP shows that ${}^{56}\text{Mn}$ is a strong indicator of hardness of the neutron spectrum through measurements made at successive distances. This find is indicative of the usefulness of lithium batteries, as they will be distributed in mass, consisting of similar, if not identical, constituents.
- Neutron spectra were obtained using the lithium batteries and were compared against spectrum obtained using activation foils. The spectra were within a factor of ten over the entire spectral range.

The following is a list of presentations generated from this program:

- A. Undergraduate Honor Thesis Defense Spring 2012, ASU, Ms. Amy Kaczmarowski
- B. SORMA West 2012, Oakland, CA, Dr. Chad Whitney (RMD).
- C. American Nuclear Society Winter Meeting 2012, San Diego, CA, Mr. Tyler Stannard (Undergraduate, ASU)
- D. American Nuclear Society 2013, Atlanta, GA, Mr. Taipeng Zhang (Graduate, ASU)
- E. Division of Nuclear Physics APS Meeting 2013, Newport News, VA, Dr. Erik Johnson (RMD)
- F. American Nuclear Society Winter Meeting 2013, Washington, DC, Taipeng Zhang (Graduate, ASU)
- G. IEEE Nuclear Science Symposium 2013, Seoul, Korea, Dr. Keith Holbert (ASU)
- H. SORMA 2014, University of Michigan, Ann Arbor, MI, Dr. Erik B Johnson (RMD)

The following is a list of papers:

- 1. Amy Kaczmarowski, "Use of Lithium Ion Batteries for Nuclear Forensic Applications", Undergraduate Honors Thesis.
- 2. Erik B. Johnson, Chad Whitney, Xiao Jie Chen, Christopher J. Stapels, Keith E. Holbert, Amy Kaczmarowski, Tyler Stannard, and James F. Christian, "Li-Ion Batteries Used as Ubiquitous Neutron Sensors for Nuclear Forensics", IEEE Transactions Nuclear Science, vol. 60, pp. 644 - 651, 2013.
- 3. Keith E. Holbert, Amy Kaczmarowski, Tyler Stannard, Erik B. Johnson, "MCNP Estimation of Trace Elements in Lithium-Ion Batteries Subjected to Neutron Irradiation," Transactions of the American Nuclear Society, vol. 107, pp. 347-349, 2012.
- 4. Keith E. Holbert, Tyler Stannard, Anthony Christie, Taipeng Zhang, Erik B. Johnson, "Modeling and Exposure of LiMnO₂ Batteries to Reactor Neutrons," Transactions of the American Nuclear Society, vol. 108, pp. 282-284, 2013.
- 5. Keith E. Holbert, Tyler Stannard, Taipeng Zhang, Anthony Christie, Erik B. Johnson, "Discriminating Fission Weapons using Lithium-Ion Batteries," Transactions of the American Nuclear Society, vol. 109, pp. 501-503, 2013.
- 6. Keith E. Holbert, Taipeng Zhang, Tyler Stannard, Erik B. Johnson., "Feasibility of Using LiMnO₂ Batteries for Nuclear Forensics," IEEE Transactions Nuclear Science, 2014.
- 7. Erik B. Johnson, Chad Whitney, Keith E. Holbert, Taipeng Zhang, Tyler Stannard, Anthony Christie, Peter Harper, Blake Anderson, and James F. Christian, "Activation Analysis Study on Li-Ion Batteries for Nuclear Forensic Applications", submitted to conference record in Nuclear Instruments and Methods Section A.

Prof. Holbert has mentored five undergraduate student on this program, where the students are exposed to various concepts involved with nuclear interactions, primarily neutron capture processes. The students were involved with collecting and analyzing the data. They obtained the activities of the produced radioisotopes in the batteries and conducted the analysis involving the mass spectrometer. One undergraduate student was involved with the simulation studies using MCNP conducted with the CR2032 (CC02) LiMnO₂ battery. Prof. Holbert is mentoring a graduate student, who has taken the lead in the analysis of the batteries and activation foils, using both the MCNP and SAND-II codes. Two of these students made presentations at national technical meetings of professional societies. Dr. Johnson had the opportunity to hire an undergraduate summer intern from MIT's Nuclear Engineering program, where the undergraduate provided studies using MCNP. The program has exposed a number of students to the field of nuclear physics and engineering and the tools associated with these fields.

A. Major Activities

The research activities were broken down into three distinct periods. The initial period is a feasibility study looking at the basic principles of a lithium battery and how they can be used for neutron detection and spectral reconstruction. The second period of the study consisted of obtaining data on the composition of the lithium batteries, exposing the batteries to high flux neutron sources, and analyzing the gamma spectroscopy to determine the initial radioisotopes' activities. The last period of the research plan is designed to extracting information from the activities for neutron spectral reconstruction. The program was arranged around the three major goals:

1. Conduct a feasibility study to determine how a lithium battery can be used for nuclear forensics.
2. Collect and process data on lithium batteries to demonstrate empirical results.
3. Provide analysis on exposed batteries and formulate forensic methods.

The initial studies on the batteries consisted of using the product datasheets to determine the constituents, the threshold energy needed to capture a neutron through (n,γ) , (n,p) , (n,d) , (n,t) , $(n,^3\text{He})$, (n,α) and $(n,2n)$ reactions. This was done to provide the initial study into how a battery can be used in an activation analysis. The estimated battery constituents were paired to the potential radioisotopes produced from an unknown neutron spectrum. Two batteries models were used to demonstrate that a neutron spectrum can be reconstructed.

Once the concept of using the battery for neutron spectral reconstruction was proven, the research group began to work on an empirical demonstration. This process required making more accurate measurements of the battery constituents using mass spectrometry. Sets of batteries were placed in high neutron fields generated at test reactors. The data were collected and processed, providing information on the pathways from the initial battery constituents to radioisotopes. In this process, MCNP models are used to validate the analysis process.

The final component of this research study is to provide a reconstructed neutron spectrum from an exposed battery. The work uses the SAND-II code, which takes known nuclear cross sections, target materials, and measured radioisotope activities. These reactions can be broken down into a series of linear equations, where the sum of various reactions as a function of energy is dependent on the initial neutron spectrum.

B. Specific Objectives

The first goal of the program is to demonstrate the feasibility of methods for using lithium batteries for nuclear forensics. The objectives for this portion of the program is to obtain information on the batteries and conducting a study on the pathways for generating radioisotopes. This would entail an initial study on the battery constituents, which is done by a review of product datasheets. As the data are processed, a large dataset on the potential pathways for generating useful, long-living radioisotopes is made. This includes gathering information on the potential nuclear reactions, threshold energies, cross sections, and natural abundance of the battery constituent isotopes. A model of the battery was used to calculate the possible production of certain radioisotopes from incident neutron spectra associated with atomic or nuclear weapons. The goal is obtained by reaching the final objective to providing spectral reconstruction of the input model neutron spectra.

1. a. Generate model battery for feasibility study
1. b. Identify pathways for generation of radioisotopes from neutron exposure, generation of reaction tables for reference
1. c. Identify potential radioisotopes of interest
1. d. Gather cross sections and set up model calculations
1. e. Conduct analysis to determine if neutron spectrum can be feasibly reconstructed.

The objectives for the second goal involve the complete data collection on a set of batteries. This process includes the disassembly of test batteries to be processed through a mass spectrometer, producing a complete list of the elemental composition within each of the batteries. The analysis includes batteries of varying sizes and

a consumer electronic device (Cell04). The same type of batteries as measured in the mass spectrometer (since mass spectrometry is destructive) are then exposed to neutrons from a research reactor. The data collection also included metal foils for validating the neutron test conditions. Gamma spectra were collected from the test batteries over multiple weeks to form a complete dataset, where the objective is to process the gamma spectra to obtain activity of radioisotopes at the point right after exposure. The goal is to provide a data set of analyzed spectra for correlation of radioisotopes being produced from target nuclei within the battery. Another objective for data collection involves the extraction of tritium content within the battery, and the development of a method for this extraction as betas from tritium decay are low energy requiring the use of liquid scintillation materials.

2. a. Purchase sets of lithium batteries for testing
2. b. Disassemble a subgroup of batteries to conduct mass analysis
2. c. Conduct mass analysis to completely determine all battery constituents
2. d. Select a separate subgroup of the batteries for exposure in reactor facilities
2. e. Set up exposure measurements and expose batteries
2. f. Measure gamma spectral emission from exposed batteries over at least two time points.
2. g. Develop method for opening exposed batteries and extract internal parts without loss of electrolyte
2. h. Provide a measure of the tritium content.

As these processes for radioisotopes generation are understood, then the process for neutron spectral reconstruction can take place. Additionally, correlations (ratios) of the various radioisotopic production pathways are other forensic metrics that might be used. The data are validated by comparisons to MCNP models using both the results of the batteries and the metal foils. An analysis of the incident neutron spectrum using the metal activation foils is key for the comparison. The final objective for the program is to determine the method for full spectral reconstruction.

3. a. Develop detailed MCNP model for comparison to measured data
3. b. Determine all relevant correction terms to accurately calculate the initial radioisotope activities
3. c. Conduct analysis to determine the actual neutron exposure spectrum using activation foils
3. d. Establish comparisons between the MCNP models and data
3. e. Identify any correlations that will determine relevant spectral information regarding weapon construction
3. f. Reconstruct incident neutron spectrum using the lithium batteries exposed in the reactors.

As one might notice, these objectives are written in terms of conducting only an activation analysis on the batteries. These wasn't the original plan identified by the collaboration, as mass spectrometry was an option. It was determined through the course of the research that a mass spectrometric measurement was not practical, in terms of detection limits and exposing a mass spectrometer to radioactive materials. Inductively Coupled Plasma Mass spectrometry (ICP-MS) can only identify elements and some isotopes to the level of 10s of parts per quadrillion, where activation analysis can provide a sensitivity significantly less than that. The physical breakdown of batteries is required for analysis in an ICP-MS, where radioactive materials produced in the battery, such as tritium, would require significant and unnecessary handling for this research.

C. Technical Results

C.1. Fundamental Battery Construction

The lithium battery is a device consisting of a cathode, separator, and anode bathed in an electrolyte. The cathode typically consists of a lithium oxide, where LiCoO_2 is a commonly used material. For current collection, the oxide is attached to an aluminum foil using an adhesive, and the oxide and aluminum are pressed together

under high pressure to form the cathode element. The common material used to construct the active component of the anode is graphite, which allows lithium ions to intercalate within the graphite molecules. The graphite is adhered to a copper foil and pressed to form the anode component. A separator material is used to space the battery's cathode and anode, and this material is typically a polypropylene or polyethylene sheet. The sheet thickness is a factor in controlling the battery performance parameters. A thin separator provides a higher capacity battery, which might be used in consumer electronics, whereas a thicker separator provides more power, which might be employed in an electric vehicle. The cathode, separator, and anode are layered accordingly, adhered together, and pressed once more to fabricate a sheet of the primary battery components. The sheet is wound or folded into the preferred shape and placed in a case. The case is typically an aluminum laminate, and the case is filled with an electrolyte, most commonly a solution with LiPF_6 as the solute. Other components such as sensors, protective casing, electrode leads, and recharging circuits are added, but are considered a small part of the volume of the battery. A diagram of the major active components of the battery is shown in Figure 1.

Major Active Components of Lithium Batteries

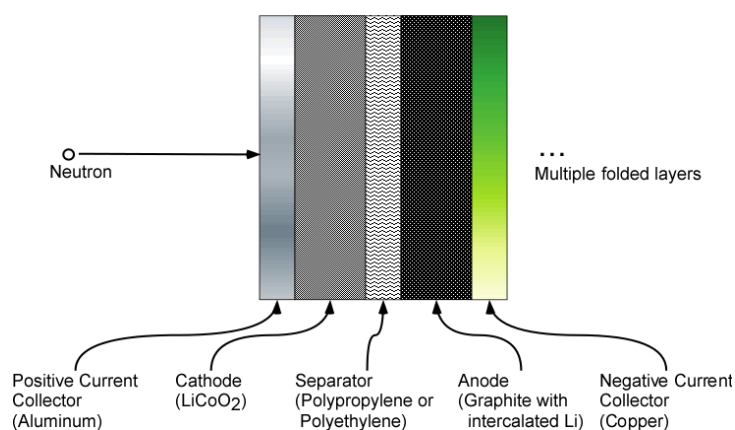


Figure 1: Diagram of a cross section of the major active components of the lithium battery. These layers are formed in a sheet which is cut and shaped to the form of the battery.

C.2. Feasibility Study to Determine Used for Nuclear Forensics

C.2.a. Setup of Model

The neutron spectra shown in Figure 2 are obtained from [1]. The abundance of high-energy neutrons from the thermonuclear device fall at a faster rate than the lower energy neutrons, but there is still a significant contribution, allowing for weapon construction discrimination. This model only uses neutrons above 0.0033 MeV, and it is understood that there will be a significant moderation of neutrons that will produce neutrons down to thermal energies. Due to the nature of the cross sections of most exothermic reactions, very low energy neutrons will cause many more nuclear reactions than indicated in the model associated with this analysis.

For batteries consisting of materials shown in appendix Table XXIV, the nuclear reaction threshold energy data were calculated for each of the naturally occurring, non-radioactive isotopes of the elements shown in the appendix Table XXV. These values were determined for (n,γ) , (n,p) , (n,d) , (n,t) , $(n,^3\text{He})$, (n,α) and $(n,2n)$ reactions. Tritium is the most common radioactive byproduct for the data that was tabulated, and as mentioned, the tritium product is related to neutron capture for neutrons of all energies. The other byproducts were also tabulated. The half-lives and daughters of the radioactive isotopes were identified. Various metastable byproducts were identified, and the Q value and threshold values were calculated based on the excited state. The Q value and threshold values for these metastable states are not much different compared to the byproduct ground state. When each of the long-lived radioisotopes is identified through any neutron capture process, the full range of sensitivity in neutron energy is known for the production of each radioisotope. This is illustrated in Figure 2 as

horizontal grey bars, where the beginning of the bar indicates the energy required of incident neutrons necessary to produce the long-lived radioisotope.

One of the most common lithium batteries is fabricated with a LiCoO_2 cathode. For this study, only the major winding components are used for the battery model. This is a simplified analyte for a nuclear forensics scientist, where a battery is opened, the electrolyte is removed, and one layer of the winding is considered. This model only considers a fully discharged state of the battery, when all of the lithium is present in the cathode. Models where the electrolyte is included are considered in work presented later in this report. This model considers the winding to be placed on a detector system that measures the gamma or beta spectra. Since tritium production in the battery is expected to be high, the low-energy beta particles emitted from tritium decay may be significant, but they require a detector systems, such as liquid scintillators, where the tritium is in direct contact, since the highest energy 18.6 keV beta particles only have a range of ~6.5 mm in dry air at sea level.

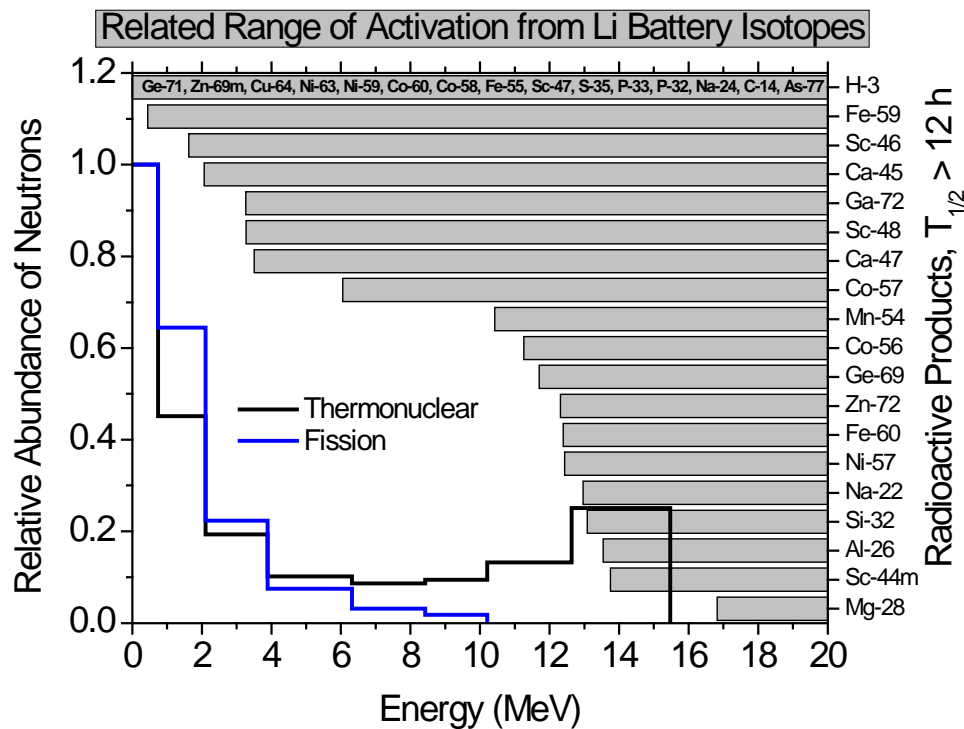


Figure 2: Plot shows the initial neutron spectra from a fission or fusion nuclear weapon referenced to the left axis. This is plotted with the range of sensitivity, shown as horizontal grey bars, for all nuclear neutron capture processes that produced the radioactive elements along the right axis. These radioactive products are a sample of possible products over a number of battery types from the data in Table XXV.

C.2.b. Common LiCoO_2 Cathode Batteries

In this model, the winding consists of aluminum (cathode current collector), LiCoO_2 (cathode), polypropylene, $(\text{C}_3\text{H}_6)_n$ (separator), carbon, C_6 (anode), and copper (anode current collector). It is important to note that only the lithium ions in the electrolyte would be removed from the system after the battery is opened. The lithium ions that are used during the charging of the battery are intercalated within the carbon lattices of the anode. Table I shows the physical properties of the battery and the relevant quantities used in calculating the number of nuclear reactions. The number of isotopes per unit volume is provided for each battery component. These number densities cannot be added across battery components, until the thickness of each component is known. The model considers neutrons that traverse normally to the surface of each component over the specified thickness.

TABLE I
PHYSICAL PROPERTIES OF THE LITHIUM ION BATTERY MODEL AND ISOTOPIC NUMBER DENSITIES

Part	Density (g/cm ³)	Molar Mass (g/mol)	Thickness (μm)	Isotope	Natural Abundance (%)	Number Density (atoms/cm ³)
Al	2.7	26.98	20	²⁷ Al	100	6.03×10 ²²
LiCoO ₂	5.05	97.87	100	⁶ Li	7.5	5.83×10 ²⁰
				⁷ Li	92.5	7.19×10 ²¹
				⁵⁹ Co	100	7.77×10 ²¹
				¹⁶ O	99.8	1.55×10 ²²
				¹⁷ O	0.04	6.21×10 ¹⁸
				¹⁸ O	0.2	3.11×10 ¹⁹
(C ₃ H ₆) _n	0.5	42.08	16	¹² C	98.9	2.34×10 ²¹
				¹³ C	1.11	2.62×10 ¹⁹
				¹ H	99.9	4.72×10 ²¹
				² H	0.02	7.08×10 ¹⁷
C ₆	1.55	12.01	100	¹² C	98.9	7.69×10 ²²
				¹³ C	1.11	8.63×10 ²⁰
Cu	8.94	63.55	20	⁶³ Cu	69.2	5.86×10 ²²
				⁶⁵ Cu	30.8	2.61×10 ²²

C.2.c. Calculation of Produced Radioactivity

The list of components is reduced to the materials identified within this section, giving the relevant information in Table I. Each of the cross sections as a function of incident neutron energy was obtained from the ENDF online resources [2]. Table II provides the maximum cross section and the energy where the maximum is obtained, illustrating the relevance for each reaction at increasing neutron energies. The equivalent threshold plot for this model using a LiCoO₂ cathode is shown in Figure 3. The threshold bars are plotted with a modeled neutron fluence after traversing through 1 km of air at sea level.

The model developed here can provide a very simple spectrum by identifying the number of nuclear reactions that occurred with respect to each radioactive isotope generated. The number of isotopes created from the nuclear event depends on knowing the properties of the starting material, and measuring the radioactive decay from the radioactive isotopes created. The only isotopes that are considered are those with a half-life greater than 12 hours. The gamma and beta spectra from the decays can be related to the isotopes of interest, and the activity of each isotope can be used to identify the number of nuclear reactions that occurred to generate the isotopes. The activity for each isotope is then converted into a neutron fluence.

The neutron spectra from the mock nuclear events at 1 km, calculated and provided in [1], were used as the input in the neutron reaction calculations. The spectra were multiplied by 100 to represent a 100 kT device for either type of weapon. An area of 1 in. × 1.5 in. was used for one layer of the battery winding, giving a total number of incident neutrons. The spectra bins shown in Figure 3 were subdivided into ten bins each, and the counts were equally distributed over those ten bins. It should be noted that from the data, the production of ⁵⁸Co or ²⁶Al relative to other byproducts, boosting might be identified, when careful consideration of all battery constituents is made. This is one of the initial indicators that suggested that utilizing production ratios might be advantageous. The cross sections for the relevant reactions were determined for each midpoint for those energy bins. The number of reactions was calculated for the volume of battery material. The known half-lives were applied to give the initial activity for each isotope, after the sums of the radioactive isotopes were determined. The induced activity from each weapon was calculated after one day and one week of the exposure and is shown in Figure 4.

TABLE II
RADIOACTIVE ISOTOPES WITHIN EXPOSED LiCO₂ CATHODE BATTERY COMPONENTS

Isotope	Half-Life	Threshold (MeV)	Reaction	Max. Cross Section (barns)	Energy at Max. (MeV)
²⁶ Al	7.2e5 y	13.5	²⁷ Al (n,2n) ²⁶ Al	0.115	20*
⁵⁸ Co	70.8 d	10.6	⁵⁹ Co (n,2n) ⁵⁸ Co	0.81	18
¹⁰ Be	1.4e6 y	4.1	¹³ C (n,α) ¹⁰ Be	0.076	18.5
²⁴ Na	15.0 h	3.3	²⁷ Al (n, α) ²⁴ Na	0.125	13
⁵⁹ Fe	44.5 d	0.8	⁵⁹ Co (n,p) ⁵⁹ Fe	0.052	13.5
³ H	12.3 y	0	⁶ Li (n,t) α	940	25×10 ⁻⁹
³ H	12.3 y	0	² H (n,γ) t	5×10 ⁻⁴	25×10 ⁻⁹
³ H	12.3 y	>8.282	Various reactions	0.001	20*
⁶⁴ Cu	12.7 h	0	⁶³ Cu (n, γ) ⁶⁴ Cu	4.5	25×10 ⁻⁹
⁶⁴ Cu	12.7 h	10.1	⁶⁵ Cu (n,2n) ⁶⁴ Cu	1.09	18
⁶³ Ni	101.2 y	0	⁶³ Cu (n,p) ⁶³ Ni	0.069	5.5
⁶³ Ni	101.2 y	8.8	⁶⁵ Cu (n,t) ⁶³ Ni	2×10 ⁻⁴	20*
⁶³ Ni	101.2 y	12.5	⁶⁵ Cu (n, ³ He) ⁶³ Co (1)	2×10 ⁻⁵	20*
⁶⁰ Co	1925.3 d	0	⁵⁹ Co (n, γ) ⁶⁰ Co (2)	37.4	25×10 ⁻⁹
¹⁴ C	5700 y	0	¹³ C (n, γ) ¹⁴ C	0.001	25×10 ⁻⁹
¹⁴ C	5700 y	0	¹⁷ O (n, α) ¹⁴ C	0.236	25×10 ⁻⁹
¹⁴ C	5700 y	13.8	¹⁸ O (n,p) ¹⁸ N (3)	0.006	20*

* Data set ends at specified energy.

- ⁶³Co decays to ⁶³Ni (branching ratio, BR = 100%) with a half-life 27.4 s.
- May also produce ^{60m}Co, which decays to ⁶⁰Co (BR = 99.776%) with a half-life 10.467 m.
- ¹⁸N decays to ¹⁴C (BR = 12.2%) with a half-life of 0.62 s.

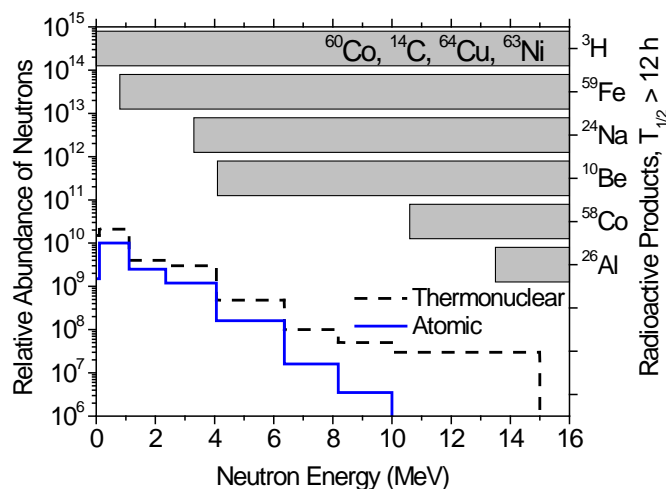


Figure 3: The plot shows the energy bin over which the radioactive isotope can be produced for nuclear reactions involving neutrons incident on the model LiCO₂ battery components. The isotopes are referenced on the right axis, and for comparison, the neutron spectrum for a thermonuclear or atomic bomb is shown and referenced to the left axis.

The activity measured in the 1 in. × 1.5 in. battery winding, ~0.88 g, is sufficiently large to measure the gamma and beta spectra. The activity after one day shows that the ⁶⁴Cu decay products dominate the spectra.

When the activity is calculated one week after the exposure, the high activity isotopes significantly drop, allowing for more isotopes to be used in the analysis. From Figure 4, the low activities of ^{26}Al , ^{10}Be , and ^{14}C are relatively too small to provide information for the analysis.

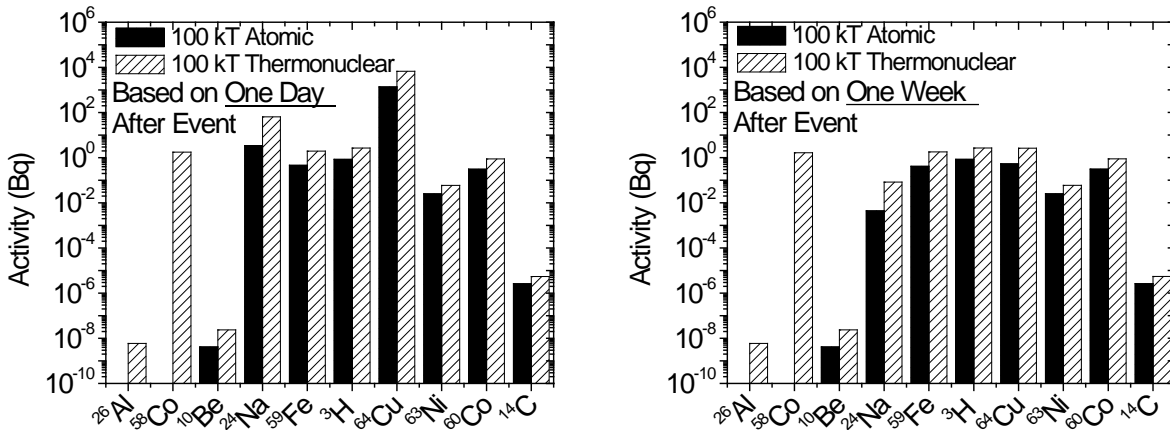


Figure 4: After a day (left plot) from the initial event, the activity of the small part of the battery is sufficiently high for a number of the isotopes for both atomic (black solid) and thermonuclear weapons (hatched). The right plot shows the activities after 1 week.

TABLE III

THE PRODUCTION RATES FOR VARIOUS GAMMA RAYS AND BETA PARTICLES FROM THE LONG-LIVED RADIOISOTOPES

Isotope	Energy (keV)		Intensity (%)	Production Rate (s^{-1})			
				Atomic		Thermonuclear	
				1 Day	1 Week	1 Day	1 Week
^{58}Co	811	γ	99.5	0	0	1.74	1.64
	511	γ	29.8	0	0	5.22×10^{-1}	4.92×10^{-1}
	864	γ	0.686	0	0	1.20×10^{-2}	1.13×10^{-2}
^{24}Na	1369	γ	100	3.45	4.45×10^{-3}	64	8.25×10^{-2}
	2754	γ	99.9	3.45	4.44×10^{-3}	64	8.24×10^{-2}
	3866	γ	7.4×10^{-2}	2.55×10^{-3}	3.29×10^{-6}	4.74×10^{-2}	6.11×10^{-5}
^{59}Fe	1099	γ	56.5	2.59×10^{-1}	2.36×10^{-1}	1.11	1.01
	466	β	53.1	2.44×10^{-1}	2.22×10^{-1}	1.04	9.49×10^{-1}
	274	β	45.3	2.08×10^{-1}	1.89×10^{-1}	8.89×10^{-1}	8.10×10^{-1}
	1292	γ	43.2	1.98×10^{-1}	1.81×10^{-1}	8.48×10^{-1}	7.72×10^{-1}
	192	γ	3.08	1.41×10^{-2}	1.29×10^{-2}	6.04×10^{-2}	5.51×10^{-2}
	131	β	1.31	6.01×10^{-3}	5.47×10^{-3}	2.57×10^{-2}	2.34×10^{-2}
	143	γ	1.02	4.68×10^{-3}	4.26×10^{-3}	2.00×10^{-2}	1.82×10^{-2}
^3H	19	β	100	8.39×10^{-1}	8.39×10^{-1}	2.69	2.69
^{64}Cu	579	β	38.5	528	2.04×10^{-1}	2600	1.01
	511	γ	35.2	483	1.86×10^{-1}	2380	9.19×10^{-1}
	1346	γ	0.475	6.51	2.51×10^{-3}	32.1	1.24×10^{-2}
^{63}Ni	67	β	100	2.52×10^{-2}	2.52×10^{-2}	5.97×10^{-2}	5.97×10^{-2}
^{60}Co	1332	γ	100	3.11×10^{-1}	3.11×10^{-1}	8.81×10^{-1}	8.79×10^{-1}
	318	β	99.9	3.11×10^{-1}	3.10×10^{-1}	8.80×10^{-1}	8.78×10^{-1}
	1173	γ	99.9	3.11×10^{-1}	3.10×10^{-1}	8.80×10^{-1}	8.78×10^{-1}

For simplification, only the rates above $1 \times 10^{-2} \text{ s}^{-1}$ for the radiation generated is provided. γ indicates a gamma-ray of the specified energy, while β indicates beta particles with the associated end point energy.

The highest energy electron that might be produced from this battery model is 1.565 MeV from the decay of ^{59}Fe . These electrons only have a range of 0.36 cm at most in aluminum, and these electrons lose energy primarily from collision loss. The radiative loss is minimal. When the battery is collected after a day from the event, and the radiation is measured, the most dominate beta particles are from ^{64}Cu with a mean energy of 190.7 keV (end point 579.4 keV). The number of expected betas from ^{64}Cu is at least three orders of magnitude greater than the next most active beta source, washing out all the other signals, particularly since the other sources have energies less than 579 keV. When the battery is retested in a week, the ^{64}Cu has significantly decayed away. At this point, an attempt can be made to measure the electrons from tritium (mean energy = 5.69 keV), which is primarily produced from the $^6\text{Li} (n,\alpha) \text{t}$ reaction.

An important note is that the tritium production will be highly dependent on the input spectrum, and this model only uses neutrons down to 3.3 keV, which are still fairly energetic. The quoted 940-barn cross section for the ^6Li reaction is for 0.025 eV neutrons, and in real world conditions, these low energy neutrons will have significant contributions to the neutron spectrum. These contributions may be large, but it is not expected to be larger than three orders of magnitude for the tritium betas to be identified above the betas from ^{64}Cu one day after the event. The tritium activity will be measurable within a week.

Another issue with the low energy beta particles from tritium is that their range in materials is around a few micrometers. To be measured, the battery winding will need to be dissolved or pulled apart in some fashion such that the tritium particles are directly exposed to a radiation detector.

C.2.d. Spectral Reconstruction

The activity of each of the isotopes identified is directly proportional to the number of nuclear reactions that occurred, and depending on the reaction cross section, the activity can be roughly correlated to the incident neutron fluence. Since the battery winding is very thin, we estimate the probability of isotope production as a sum of the products of the cross sections and the number of isotopes per unit area within the battery volume. These probabilities are shown in Figure 5. The probabilities for ^{24}Na and ^{59}Fe slowly decrease to zero, which will cause a significant deviation in the reconstructed spectrum if the entire region of sensitivity is used to define each bin. This is because the isotope production is dominated by the higher energy neutrons. The final bins use a region where the probability is high and fairly uniform. In this model, an upper limit of 15 MeV is used.

The probabilities in Figure 5 are only partially related to the input spectrum, and the probability of a single isotope alone cannot provide a means for spectral reconstruction, as the only measurable quantity is the activity for each of the long-lived isotopes. This activity can be easily converted to an initial number of isotopes generated from the nuclear event. The total number of the relevant isotopes generated is then correlated to the number of incident neutrons. The spectrum can be reconstructed by using the three algorithms described below.

1. The first algorithm uses a conversion factor (A_i) to determine the total number of incident neutrons within the modified range of sensitivity for each of the isotopes. The lower bin edge of modified range is indicated in Table IV, where the upper limit is 15 MeV for each bin. The modified range only defines the region over which the input neutrons are summed. The total isotope production (I_i) is over the full range of sensitivity. The neutron total from the ^{58}Co conversion gives the total number of isotopes in the highest bin (10.6 MeV to 15 MeV). The neutron total from the ^{24}Na minus the total from the ^{58}Co provides the number of neutrons for the next bin. The process is repeated for each isotope, providing a reconstructed spectrum, where each spectral bin has n_i neutron counts.

$$\begin{aligned} n_1 &= A_1 \cdot I_{\text{Co-58}} \\ n_i &= (A_i \cdot I_i) - (A_{i-1} \cdot I_{i-1}) \end{aligned} \tag{1}$$

2. The second algorithm generates a different conversion factor (B_i) that directly transforms the number of isotopes generated into the number of incident neutrons for each spectral bin. This factor eliminates the step of subtracting the total number of neutrons determined from each isotope from each other.

$$n_i = B_i \cdot I_i \tag{2}$$

TABLE IV
MODIFIED RANGE OF SENSITIVITY FOR EACH ISOTOPE

Isotope	Lower Bin Edge (MeV)
⁵⁸ Co	10.6
²⁴ Na	7
⁵⁹ Fe	4
³ H	0
⁶⁴ Cu	0
⁶⁰ Co	0

3. The third algorithm uses the A_i conversion factors to provide the total number of incident neutrons over the modified range of sensitivity. A second factor C_i is applied to provide the number of neutrons within the spectral bin (see Table IV). The C_i term is defined as the fraction of probabilities within the spectral bin, i.e. the ratio of the sum of probabilities for the spectral bin over the entire range of sensitivity.

$$n_i = C_i \cdot A_i \cdot I_i \quad (3)$$

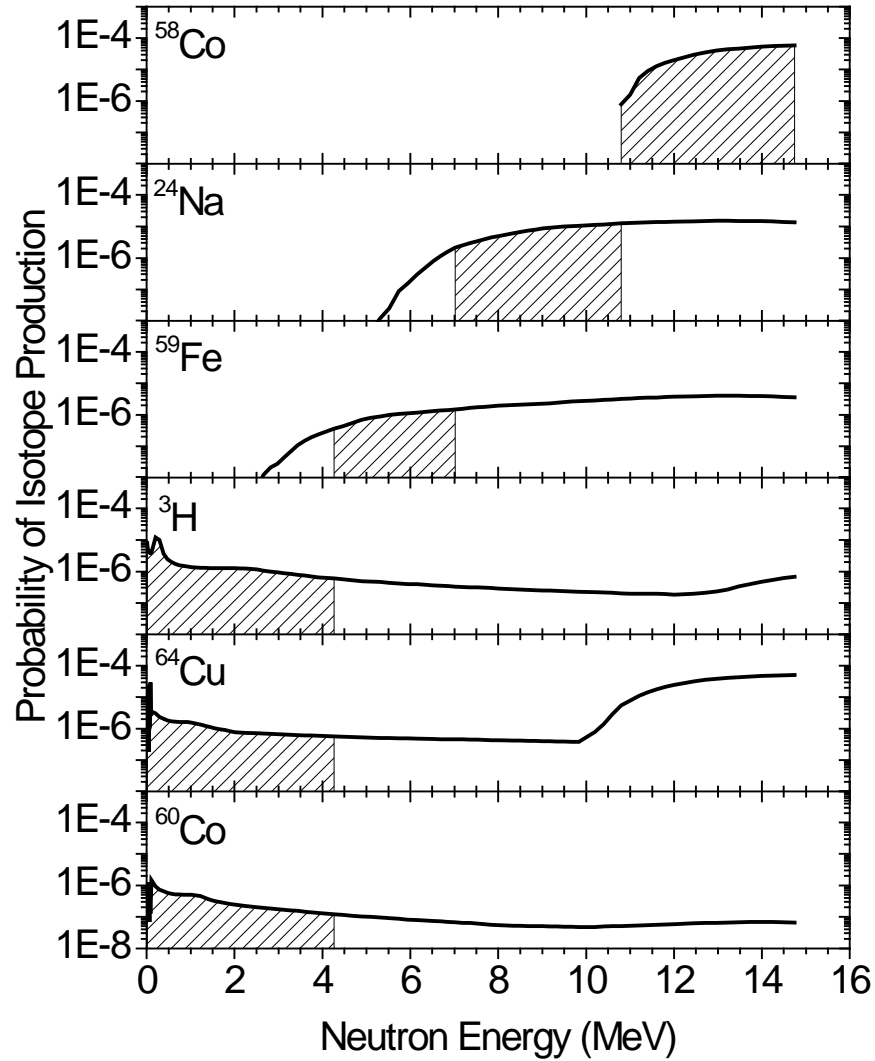


Figure 5: The plot shows the probability of isotope production for each of the relevant radioisotopes generated in the lithium ion battery. The hatched areas indicate the bin regions used in reconstruction of the spectrum.

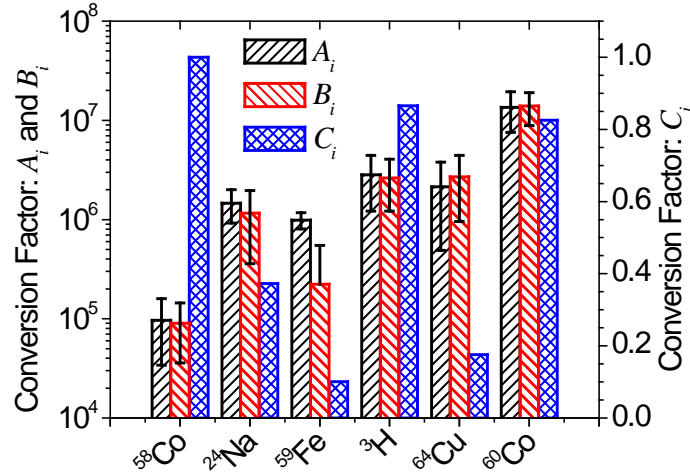


Figure 6: The ratio of the isotopes produced to the number of incident neutrons over the spectral range for A_i and B_i are shown with respect to the left axis. The right axis is referenced to the C_i factor.

The conversion factors A_i and B_i are determined numerically. Under the condition that the input spectrum is not known, we consider randomly generated spectra to correlate the radioactive isotope production to any input spectrum. The spectral binning is done exactly the same way as for calculating the activities, each of the bins is subdivided into ten sub-bins. The contents for each of eight random spectra were a uniform distribution of numbers from 10^2 to 10^{13} by using a uniform random number generator (U) from 0 to 1. The random number for each spectral bin is generated by $U \times 10^{(U \times 9 + 4)}$. The sum for input over the specified range was determined, and the conversion factors A_i and B_i were calculated. The mean and standard deviation of the conversion factors were determined over eight random spectra. The random input spectrum is utilized to generate an uncorrelated conversion factor to the simulated fission and fusion spectrum in Figure 3. It is expected that the conversion factors cannot be absolute, as information is lost by compressing the spectral data into one measurable value, the isotope production. The three conversion factors are presented in Figure 6. The conversion factor C_i does not have an error bar as it is based on the isotope production probabilities shown in Figure 5.

The concept for measurement in the real world will consist of measuring the nuclear spectra from an activated battery, particularly components of the battery such as the battery winding. The spectra can be used to determine isotope identification and activity. The activity can be measured at various times to obtain an accurate measure of the initial isotopic concentration within the analyte. The isotope concentrations will then be converted into an incident neutron spectrum using the algorithms discussed.

The LiCoO_2 cathode battery model was used to reconstruct the incident neutron spectra, which are shown in Figure 7. The model only has a resolution of four energy bins, but the battery has the ability to roughly reconstruct the incident neutron fluence. The same methods were applied to a battery with a Li-FeS_2 cathode. The Li-FeS_2 cathode model included an electrolyte, unlike the LiCoO_2 model. As shown in Figure 7, once all the neutron capture reactions are accounted for, the battery is able to produce a rough estimate of the incident neutron fluence over only four energy bins. In this simplified model, the LiCoO_2 battery has an advantage over the Li-FeS_2 in that the ^{58}Co production has a very high threshold of 10.6 MeV, providing a clear signal.

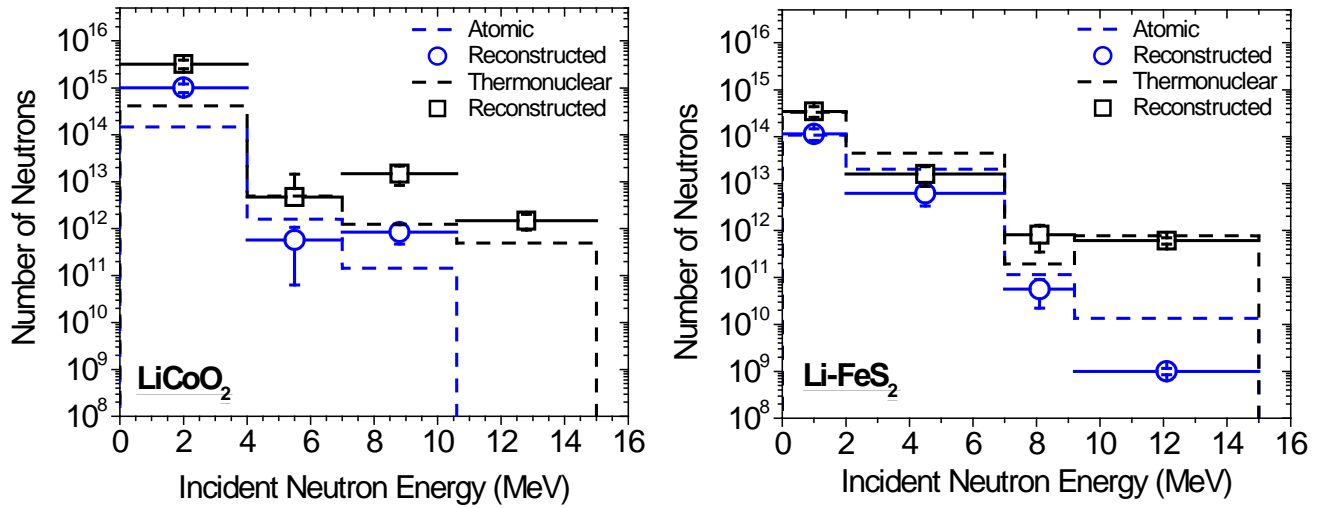


Figure 7: The reconstructed spectrum is shown as data points, whereas the input spectrum is shown as the dashed lines. The data points account for all neutrons over the bin specified by the input spectrum, and the points are placed in the center of the bin.

To obtain a high resolution for the spectral reconstruction, the spectra in Figure 7 are combined. The threshold reactions for either model are sensitive to neutrons of different energy ranges. Each spectrum in Figure 7 is divided into smaller energy bins, such that the subdivided energy bins for both models are identical. The rebinning subdivided existing bins, where new bins that span across the original bin were filled with a weighted value based on the fraction of area spanned by the new bin over the original bins. The rebinning allows for a straight forward averaging of the spectrum from each of the batteries. The \log_{10} of the values in the bins was taken and averaged, then 10 to the power of the average is used to generate the new plot. The “higher resolution” energy spectra are shown in Figure 8. When combining the battery models in this way, the incident neutron spectra are accurately reconstructed. It is expected that as more battery types are used, the results will improve with decreasing errors. We note here that the spectral resolution is still fairly rough, as the resulting spectra only has effectively seven energy bins.

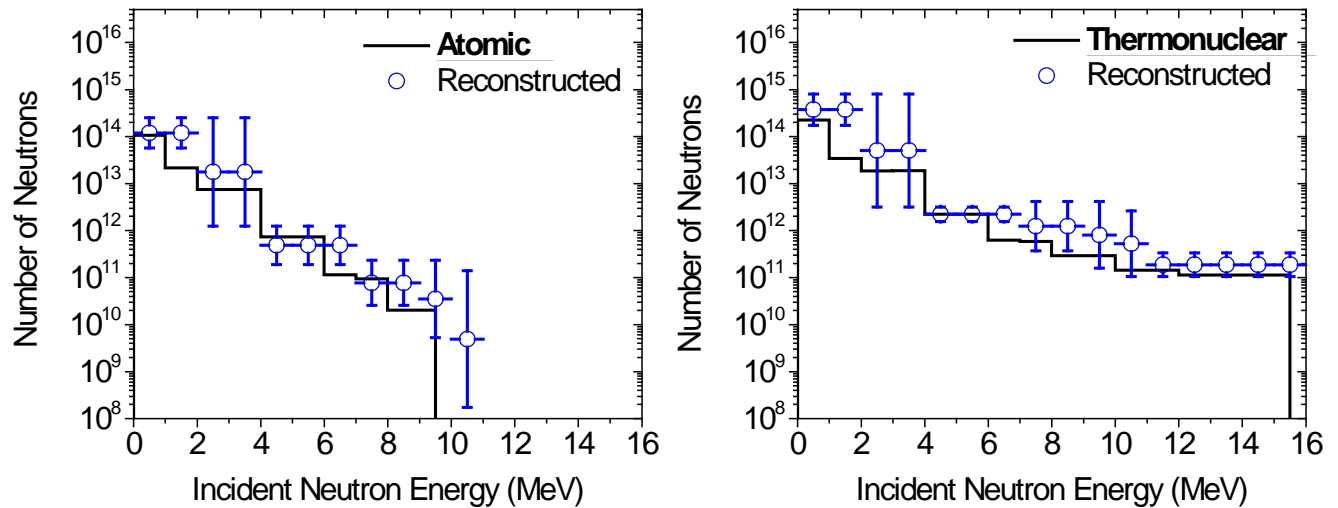


Figure 8: The reconstructed spectrum is shown as data points, whereas the input spectrum is shown as the solid lines. The data points account for all neutrons over the bin specified by the input spectrum, and the points are placed in the center of the bin.

C.3. MCNP Study for Feasibility of Inductively-Coupled Plasma Mass Spectroscopy

This analysis is a study on the potential to use Inductively-Coupled Plasma Mass Spectroscopy (ICP-MS) for determining the end products within a lithium battery after exposure.

C.3.a. Battery Models Considered

This study focused in on three common types of batteries, defined by their cathode materials: 1) LiCoO_2 (lithium cobalt oxide), LiMn_2O_4 (lithium manganese oxide), and LiFePO_4 (lithium iron phosphate). The LiCoO_2 batteries have the most desirable characteristics when considering manufacturing; hence, their widespread use in powering cellular phones and laptop computers. However, cobalt metal is about ten times more expensive than manganese or nickel, while iron phosphate is non-toxic and lower in price. Other battery materials of interest include the electrolyte salt (e.g., lithium hexafluorophosphate, LiPF_6 , or lithium tetrafluoroborate, LiBF_4), the anode (carbon black) and current collectors (aluminum and copper foils for the cathode and anode, respectively).

C.3.b. Production of Trace Elements

A screening of the possible reactions of interest was first performed. This work was followed by MCNP simulations to estimate the production of trace elements due to neutrons emitted from the detonation of a nuclear device using fissile material. ICP-MS has a detection limit of parts per billion (ppb). For those reactions producing (near) stable products, the ICP-MS determination of the trace elements could permit computing neutron exposure levels and energy spectra. Standard ICP-MS requires dissolving the sample in a solvent, but there are attachments, such as methods that use laser ablation, to instantaneously prepare solid samples.

The battery material isotopes and their abundances, and the reaction Q -values and cross-sections provided a preliminary list of candidate reactions for study. The information collected was used to evaluate 21 isotopes in the aforementioned elements for the following reactions: (n,γ) , (n,p) , (n,d) , (n,t) , $(n,^3\text{He})$, and (n,α) . Initial calculations focused on an instantaneous thermal neutron fluence of 10^{12} n/cm^2 based on weapon yields on the order of 10 kt at a distance of 750 m. Table V contains the data on those isotopes and reactions that an analyst may find most useful in forensic battery evaluation.

The ^6Li isotopic abundance was first investigated as a candidate for forensic evaluation by ICP-MS. The concentration of ^6Li is decreased by approximately 0.0706 ppb of Li due to the $^6\text{Li}(n,\alpha)$ reaction and the neutron fluence of 10^{12} n/cm^2 . Noteworthy is that the IUPAC Commission on Atomic Weights and Isotopic Abundances has found mole fractions for ^6Li to vary from 72.2×10^6 to 77.3×10^6 ppb in naturally occurring terrestrial materials [3]. Since a naturally occurring isotopic change of 5.1×10^6 ppb is far larger than the range of parts per billion due to the neutron exposure, it is determined that isotope ratio mass spectrometry cannot be used for fluence predictions without an identical battery as a standard for comparison.

TABLE V
SAMPLING OF REACTION SCREENING RESULTS

Reaction	Threshold Energy (MeV)	Reaction Product Half-Life	Decay Product
$^1\text{H}(n,\gamma)^2\text{H}$	0	stable	^2H
$^6\text{Li}(n,\gamma)^7\text{Li}$	0	stable	^7Li
$^6\text{Li}(n,p)^6\text{He}$	3.2	*	^6Li
$^6\text{Li}(n,d)^5\text{He}$	2.8	*	^4He
$^6\text{Li}(n,\alpha)^3\text{H}$	0	12 y	^3H
$^7\text{Li}(n,\gamma)^8\text{Li}$	0	*	2 ^4He
$^7\text{Li}(n,t)^5\text{He}$	3.8	*	^4He
$^7\text{Li}(n,\alpha)^4\text{H}$	6.1	*	$^4\text{H} \rightarrow \beta + ^3\text{He}$
$^{10}\text{B}(n,\alpha)^7\text{Li}$	0	stable	^7Li
$^{27}\text{Al}(n,\gamma)^{28}\text{Al}$	0	2.2 m	^{28}Si
$^{27}\text{Al}(n,t)^{25}\text{Mg}$	11.3	stable	^{25}Mg
$^{27}\text{Al}(n,\alpha)^{24}\text{Na}$	3.2	15 h	^{24}Mg
$^{31}\text{P}(n,\gamma)^{32}\text{P}$	0	14 d	^{32}S
$^{55}\text{Mn}(n,\gamma)^{56}\text{Mn}$	0	2.6 h	^{56}Fe
$^{59}\text{Co}(n,\gamma)^{60}\text{Co}$	0	5.3 y	^{60}Ni
$^{56}\text{Fe}(n,\gamma)^{57}\text{Fe}$	0	stable	^{57}Fe
$^{58}\text{Ni}(n,\gamma)^{59}\text{Ni}$	0	760 ky	^{59}Co
$^{60}\text{Ni}(n,\gamma)^{61}\text{Ni}$	0	stable	^{61}Ni
$^{62}\text{Ni}(n,\gamma)^{63}\text{Ni}$	0	100 y	^{63}Cu
$^{63}\text{Cu}(n,\gamma)^{64}\text{Cu}$	0	12.7 h	61.5% ^{64}Ni ; 38.5% ^{64}Zn
$^{65}\text{Cu}(n,\gamma)^{66}\text{Cu}$	0	*	^{66}Zn
$^{65}\text{Cu}(n,^3\text{He})^{63}\text{Co}$	12.5	*	^{63}Ni

* An asterisk indicates a half-life of less than one hour. The decay products are from the radioisotopes on the left of the parenthesis.

The $^{10}\text{B}(n,\alpha)$ reaction occurring in the LiBF_4 solvent is also evaluated because of its 3840 b cross section. This reaction produces a stable product of ^6Li , which is (unfortunately) already present within the LiBF_4 electrolyte. For comparison, the ^6Li content of the original LiBF_4 is 4.82×10^{20} atoms/cm³ such that the ^6Li increases by 0.764 ppb from a 10^{12} n/cm² fluence. Using the change in ^{10}B to ^{11}B ratio is not an option since the ^{11}B isotopic abundance has been found to vary from 796.1×10^3 to 810.7×10^3 ppb [3]. Similar to the cathode, the increased abundance of ^6Li in the solvent from the reaction cannot be used for fluence estimation.

Another aspect investigated is the use of specific reaction products as identifiers to determine whether the battery was exposed to neutrons from an exclusively fission weapon versus a thermonuclear device. Table V shows that some of the reactions require threshold energies for activation above the normal Watt fission spectrum. The 14.1 MeV neutrons could produce isotopes normally foreign to the battery components. For example, the $^{27}\text{Al}(n,t)$ reaction creates ^{25}Mg , which may be detectable in the aluminum current collector.

C.3.c. MCNP Simulation Input

The U-235 fission spectrum from a 10 kt device is modeled in MCNP5 [4]. Although varying distances from the device were simulated, the results presented here are at 1 km from the point of detonation in air. A

comparison of the source neutron energy spectrum to that of the neutrons at 1 km, where the fluence was 4×10^{12} n/cm², is provided in Figure 9.

Three different cathode materials (LiCoO₂, LiMn₂O₄, and LiFePO₄) were employed in separate simulations. An electric or hybrid car was used for the simulation, and due to the size of the car battery and resultant number of individual material layers, it would be impractical to model the battery in MCNP without the use of lattices. In order to simplify the analysis, the car battery was left as a solid mix.

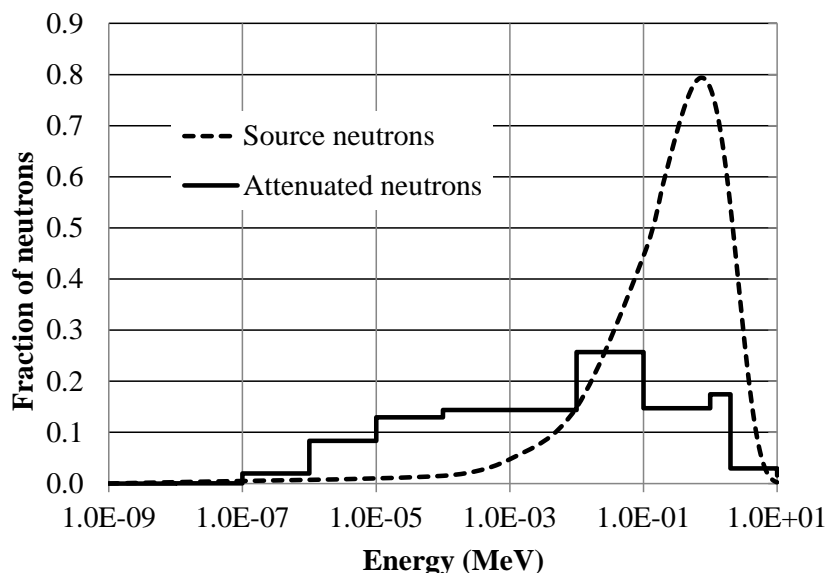


Figure 9: Neutron spectra from the source and incident to the Li-ion batteries (the latter is from an MCNP5 simulation).

C.3.d. Simulation Output

The list of important reaction products are shown in Table VI. Besides the reactions in those tables, nickel based variants of Li-ion batteries produce stable ⁶¹Ni, and radioactive ⁵⁹Ni and ⁶³Ni. Although the concentrations are small, all statistical checks passed in the MCNP5 runs for the results presented using 500 million histories for the DXTRAN sphere created to surround the battery.

Many of these product concentrations are quite low. In fact, product concentrations that are $\leq 1.0 \times 10^{-5}$ ppb are generally beyond the current capabilities of trace analysis using ICP-MS. In addition, about half of the products are gases at ambient temperature. Notwithstanding, there have been studies concerning the diffusion of helium in various materials, primarily for studies on the effects of He embrittlement and for fusion reactors that demonstrate the tendency of He to form microstructure bubbles embedded in the materials.

The only perhaps unexpected new reaction is that of ¹H(n, γ) from the hydrogen reactant present in the electrolyte solvent and polyethylene separator. The use of deuterium as an analyte would be limited as it exists in most batteries due to its natural abundance (0.02%), thereby making it difficult to determine the quantity produced versus that already present in the battery.

TABLE VI
STABLE REACTION PRODUCT CONCENTRATIONS

Reaction	Quantity in LiCoO ₂ Battery (ppt)	Quantity in LiMnO ₂ Battery (ppt)	Quantity in LiFePO ₄ Battery (ppt)
¹ H(n,γ) ² H	0.083	0.081	0.084
⁶ Li(n,γ) ⁷ Li	0.00019	0.00015	0.00016
⁶ Li(n,d)[⁴ He]	0.00027	0.00026	0.00023
⁷ Li(n,γ)2[⁴ He]	0.0011	0.00063	0.00069
⁷ Li(n,α)[³ He]	0.00021	0.00014	0.00013
⁵⁶ Fe(n,γ) ⁵⁷ Fe	n/a	n/a	0.0050

For the purposes of this table, *stable* is defined as having a half-life of less than 1 second such that a reaction product shown in square brackets is actually the decay product.

The trace elements produced from the neutron radiation are on the order of 0.1 ppt and include ⁶⁰Co, ⁵⁶Fe, ²⁸Si, ⁶⁴Ni and ⁶⁴Zn; see Table V. In addition to being among the most prevalent isotopes produced, these products cover the diversity of batteries that may be collected after an incident. Specifically, the ²⁸Si, ⁶⁴Ni, and ⁶⁴Zn produced as a result of (n,γ) reactions with the aluminum and copper electrode supports can be found in any type of battery presently on the market. The ⁶⁰Co and ⁵⁶Fe provide additional coverage for LiCoO₂ and LiMnO₂ batteries, respectively, as well as the LiMnCoNiO₂. The ⁵⁶Fe is produced from the beta decay of ⁵⁶Mn produced by an (n,γ) reaction with ⁵⁵Mn. Each of these products is stable on the timescales being considered for analysis and are also easily identifiable in that they are linked to only one reaction with one element in a given battery. The general ICP-MS detection limits for these elements are given in Table VII.

Given the detection limits shown in Table VII, the quantities of specific isotopes observed in car batteries exposed to a 10 kt nuclear explosion at a distance of 1 km are below or very near the general limits of detection for ICP-MS. However, the concentrations shown in Table VI are average values across a rather large solid car battery mixture. The product concentrations in the outside mesh layer are on the order of 10¹² cm⁻³ whereas interior concentrations are three orders of magnitude smaller.

TABLE VII
GENERAL LIMITS OF DETECTION FOR ICP-MS [5].

Element	Detection Limits (ppt)
Cobalt	< 0.05
Silicon	5 – 10
Iron	1
Nickel	< 0.05
Zinc	0.05 – 0.1

C.4. MCNP Analysis of CR2032 (CC02) LiMnO₂ batteries to Discriminate Fission Weapons

C.4.a. Model Setup

The neutron spectra from Little Boy and Fat Man [6] were incorporated into an MCNP5 [4] model of a point source surrounded by a series of concentric spheres at varying distances from the source. The model was filled with dry air at a temperature of 15 °C. Surface flux (f2) tallies with fine energy bins were set on spheres at distances of 800 m, 1 km, and 1.2 km from the source. The tally results from these, shown in Figure 10, models were placed into the source specification for an inward spherically distributed source surrounding a coin-cell sized CR2032 (CC02) LiMnO₂ battery. The two-step MCNP5 calculation was designed to simulate battery collection

points at reasonable distances from the point of detonation. The exposed Li-ion batteries are assumed to be gathered in the vicinity of 1 km from the blast point given the level of damage at closer distances. Table VIII presents results for reactions providing statistically significant numbers of activation products for the composition of the selected Li-ion battery. With the intent being to utilize gamma spectroscopy in the post-detonation analysis, further investigation reveals that some of activation products (e.g., ^{28}Al) would have low emission rates and/or decay too rapidly to be of use.

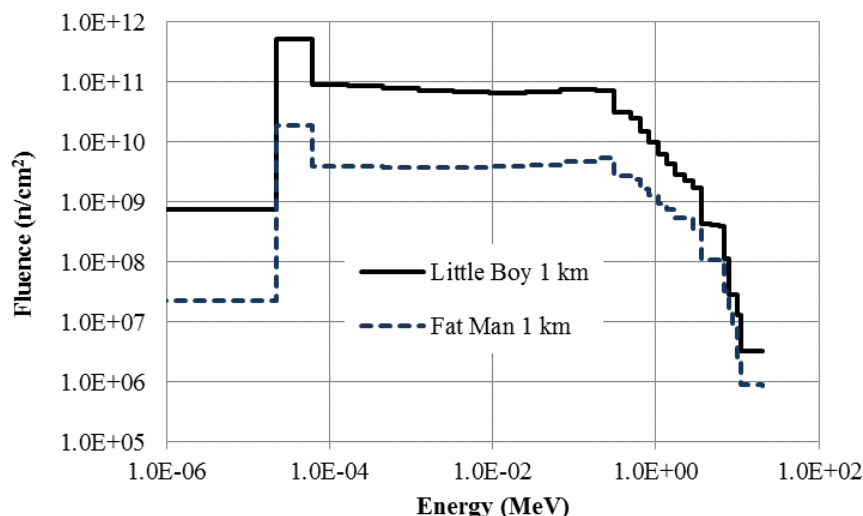


Figure 10: Tally results of Fat Man and Little Boy source spectra with 10 kT equivalent weapon size at 1 km from the detonation point.

TABLE VIII
SIGNIFICANT NEUTRON REACTIONS IN LiMnO_2 BATTERY FROM FISSION WEAPON OUTPUT SPECTRUM AT 1 KM

Reaction	Product Half-life	Induced Activity (Bq)	
		Little Boy	Fat Man
$^{58}\text{Fe}(n,\gamma)^{59}\text{Fe}$	44.5 d	0.345	0.0155
$^{55}\text{Mn}(n,\gamma)^{56}\text{Mn}$ $^{56}\text{Fe}(n,p)^{56}\text{Mn}$	2.58 h	213,000	8,950
$^{50}\text{Cr}(n,\gamma)^{51}\text{Cr}$	27.7 d	7.58	0.295
$^{27}\text{Al}(n,\gamma)^{28}\text{Al}$	2.3 m	217	8.59
$^{23}\text{Na}(n,\gamma)^{24}\text{Na}$	15.0 h	6.51	0.273
$^{59}\text{Co}(n,\gamma)^{60}\text{Co}$	5.27 y	0.00155	0.0000652

C.4.b. Activity Ratios

The moment of detonation will very likely be known to great precision and with the availability of GPS, the location of battery samples collected can be pinpointed to significant accuracy. Using the measurable activity after collection, along with the distance and time knowledge, the activity at the instant after detonation can be calculated.

Since the parent nuclei of each radioactive isotope found have unique reaction cross sections, a different neutron spectrum could cause the activity ratio between the formed radionuclides to change. Activity ratios for the LiMnO_2 battery in response to the neutron spectra from 10 kT size weapons of the Fat Man and Little Boy types at distances of 800 m, 1 km, and 1.2 km were calculated and compared. The 1 km ratios for the two weapons are shown in Table IX.

To determine which ratios are useful for determining weapon type, the separation between ratios was first examined. The ratios with the largest separation were considered most useful because they may be the least

likely to be washed out by statistical error in counting. The $^{59}\text{Fe}/^{51}\text{Cr}$ activity ratios are 14.6% different at 1 km distance from the detonation point (air zero), which makes them the most useful for this battery in ascertaining the types of fission weapon employed. The next most useful ratio as judged by percent difference is $^{51}\text{Cr}/^{60}\text{Co}$ with its 8.1% separation between ratios. However, due to counting complications the optimal ratios must be evaluated on more factors than the percent difference alone.

TABLE IX
INITIAL ACTIVITY RATIOS OF SELECTED RADIONUCLIDES AT 1 KM FROM DETONATION POINT

Ratio	Little Boy Ratio	Fat Man Ratio	Percentage Difference
$^{59}\text{Fe}/^{56}\text{Mn}$	0.00101	0.00108	7.1%
$^{59}\text{Fe}/^{24}\text{Na}$	0.159	0.170	7.0%
$^{59}\text{Fe}/^{51}\text{Cr}$	0.0460	0.0532	14.6%
$^{59}\text{Fe}/^{60}\text{Co}$	220	235	6.5%
$^{56}\text{Mn}/^{24}\text{Na}$	157	157	0.1%
$^{56}\text{Mn}/^{51}\text{Cr}$	45	49	7.5%
$^{56}\text{Mn}/^{60}\text{Co}$	217,500	216,400	0.5%
$^{24}\text{Na}/^{51}\text{Cr}$	0.290	0.313	7.6%
$^{24}\text{Na}/^{60}\text{Co}$	1390	1380	0.4%
$^{51}\text{Cr}/^{60}\text{Co}$	4780	4410	8.1%

The transient behavior of the ratios was also examined. Figure 11 displays the activity ratios for $^{59}\text{Fe}/^{51}\text{Cr}$ for the first five days after detonation. As expected, the activity ratio for radioisotopes with sufficiently long half-lives remains roughly constant. While the ratios shown in Figure 11 are for a LiMnO_2 battery, the ^{51}Cr and ^{59}Fe originates in the steel casing of the battery. Each battery made for personal use has a steel casing, although the alloy may be different between batteries. Hence, these results are extensible to other battery types.

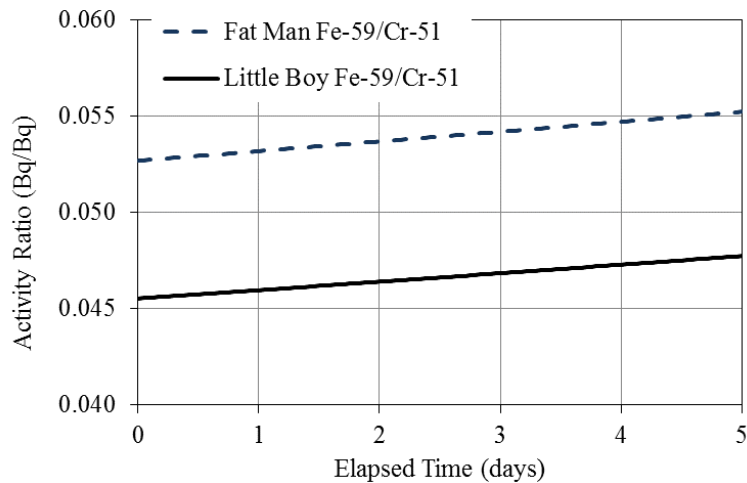


Figure 11: $^{59}\text{Fe}/^{51}\text{Cr}$ activity ratios for the two different weapon types 1 km from the detonation point.

In similar fashion, the ratio dependency on distance was studied. Figure 12 exhibits the $^{24}\text{Na}/^{51}\text{Cr}$ ratios for the simulated distances. As can be seen, the ratios demonstrate a nearly constant trend. Not all of the ratios provided sufficient separation as they had overlapping error bars unlike those shown in Figure 12.

Some of the ratios mentioned in this discussion may prove even more useful for other battery compositions. The Co-60 was present as an activated impurity in the LiMnO_2 battery, but in the more popular LiCoO_2 batteries, cobalt is present in much higher mass. In fact, scoping calculations with a simplified LiCoO_2

battery and a 10 kT weapon show an activity of 165 Bq for the Little Boy spectra and 1.86 Bq for the Fat Man spectra compared to <0.01 Bq in Table IX for LiMnO_2 . Thus, the Co-60 activity ratios found useful in LiMnO_2 batteries may be even more informative from LiCoO_2 batteries.

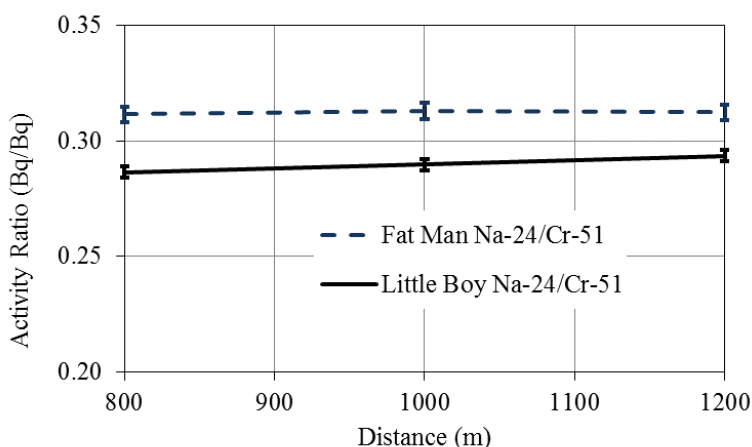


Figure 12: $^{24}\text{Na}/^{51}\text{Cr}$ activity ratio as a function of distance one day after exposure.

C.5. Collection of Data for Empirical Studies

C.5.a. Exposure of Lithium Batteries

A collection of lithium batteries was selected for exposure. The batteries were selected based on varying composition of cathode materials used and whether the battery is common. In addition, the consumer electronic device (Cell04) and a battery from the consumer electronic device (Cell03) were exposed. The batteries were exposed at two facilities, the TRIGA reactor at Oregon State University, and the Fast Neutron Irradiator (FNI) at University of Massachusetts Lowell. The on-site staff for both of these facilities provided significant and appreciated assistance in the setup and execution of the exposure plans, while providing facilities or time to collect gamma spectra of the exposed batteries. The corresponding estimates of the neutron spectra are shown in Figure 13. The TRIGA facility allows the batteries to be vertically placed in an in-core cell. The first run at TRIGA was taken where the batteries were vertically stacked and exposed at once within the in-core irradiation tube. The second run at TRIGA the batteries were exposed one at a time using a pneumatic transfer tube, termed Rabbit. The FNI at UMass is a vessel placed next to the research reactor core, where the vessel is lined with shielding material to attenuate gammas and slow neutrons. The effect is a hardened neutron spectrum with a low gamma flux. The vessel allows for a large area of material to be exposed to a uniform flux of neutrons, where in these experiments one run was used to expose multiple batteries at a single time. The FNI results allowed for greater uniformity of exposure from battery to battery, and there was sufficient area left on the foam holder (a square piece of foam with cut out areas to insert batteries) to place activation metal foils. These foils are $\frac{1}{2}$ " in diameter, elementally pure, and provided with accurate measurements of their mass and thickness. A table of the batteries and the calculated fluence is provided in Table X. The second run at FNI includes batteries models exposed at TRIGA for comparison.

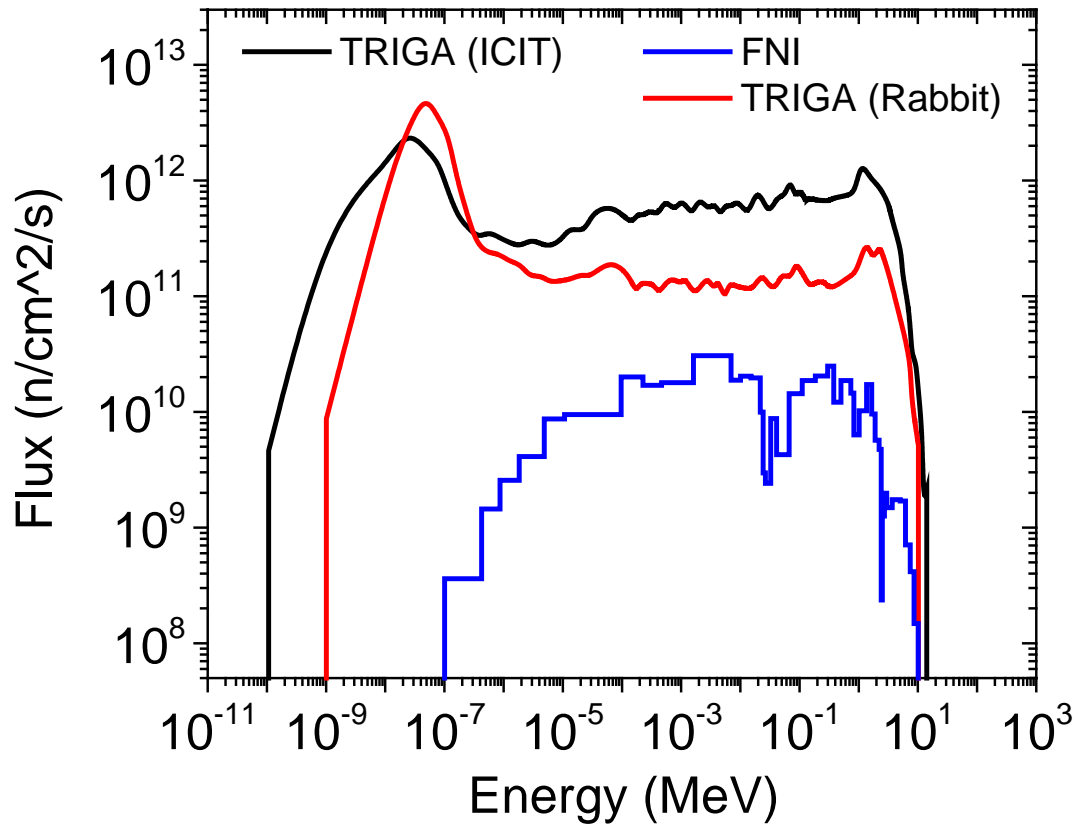


Figure 13: The spectra of the TRIGA (Oregon State) and the FNI (UMass Lowell) [7] facilities. Note that the spectra are not shown as a differential flux, suggesting that the absolute numbers are dependent on the bin width. The total flux from the FNI is less than TRIGA. These spectra are obtained from data generated at these facilities and may be similar but not exactly the same spectra during the exposure of the batteries.

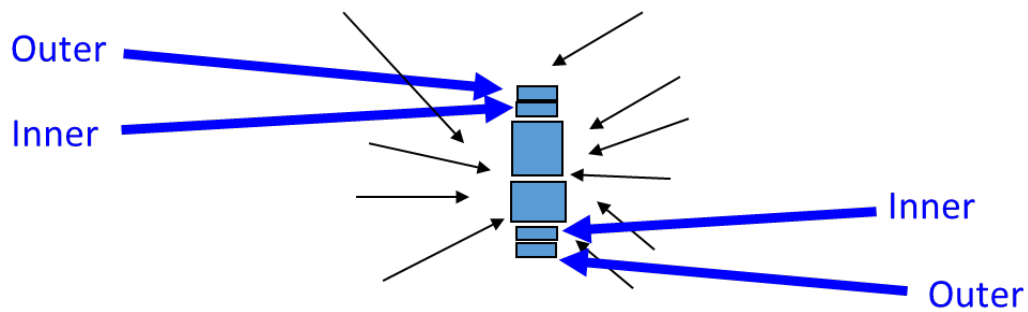


Figure 14: Diagram of the battery stack geometry for exposure in the TRIGA reactor, where the batteries are placed in the ICIT (Inner Core Irradiation Tube). Inner refers to interior to the stack vertically. The black arrows are drawn to represent neutrons.

TABLE X

BATTERIES AND ACTIVATION FOILS THAT HAVE BEEN EXPOSED TO NEUTRONS AT EITHER THE TRIGA OR FNI FACILITIES.

Qty	Model [Foil Material]	Cathode	Neutron Facility	Fluence* n/cm ²	Run Number	ID
2	LIR2032, 3.6V, 40 mAh	LiCoO ₂	TRIGA	8.9×10 ¹³	1	CC01
2	CR2032, 3.0V, 240 mAh	LiMnO ₂	TRIGA	8.9×10 ¹³	1	CC02
1	18650, 3.7V, 2000 mAh	LiMnNiO ₂	TRIGA	8.9×10 ¹³	1	18650A
1	RCR123A, 3.2V, 450 mAh	LiFePO ₄	TRIGA	8.9×10 ¹³	1	RCR01
2	Li AA, 1.5 V, 3Ah	Li-FeS ₂	FNI	5.2×10 ¹⁴	1	AA01
2	RCR123A, 3.2V, 450mAh	LiFePO ₄	FNI	5.2×10 ¹⁴	1	RCR02
2	18650, 3.7V, 2.6Ah	LiMnNiO ₂	FNI	5.2×10 ¹⁴	1	18650B
2	Li AA, 3.6V, 2.6Ah	Li-SOCl ₂	FNI	5.2×10 ¹⁴	1	AA02
2	ML-2020, 3V, 45 mAh	LiMnO ₂	FNI	5.2×10 ¹⁴	1	CC03
2	VL-2020, 3V, 20 mAh	V ₂ O ₅	FNI	5.2×10 ¹⁴	1	CC04
2	Cell Phone Bat, 3.7V, 1.15 Ah	LiCoO ₂	FNI	5.2×10 ¹⁴	1	Cell01
2	Small-Profile, 4V, 1mAh	LiCoO ₂	FNI	5.2×10 ¹⁴	1	Cell02
10	Activation Foils: Fe, Zr, Mg, V, Al, In, Au, Cu, Ni		FNI	5.2×10 ¹⁴	1	
1	Electronic Device Battery		TRIGA	8.9×10 ¹³	2	Cell03
1	LIR2032, 3.6V, 40 mAh	LiCoO ₂	TRIGA	8.9×10 ¹³	2	CC01
1	CR2032, 3.0V, 240 mAh	LiMnO ₂	TRIGA	8.9×10 ¹³	2	CC02
1	Electronic Device		TRIGA	8.9×10 ¹³	2	Elec01
1	Electronic Device		FNI	5.3×10 ¹⁴	2	Elec01
1	RCR123A, 3.2V, 450 mAh	LiFePO ₄	FNI	5.3×10 ¹⁴	2	RCR01
2	LIR2032, 3.6V, 40 mAh	LiCoO ₂	FNI	5.3×10 ¹⁴	2	CC01
2	CR2032, 3.0V, 240 mAh	LiMnO ₂	FNI	5.3×10 ¹⁴	2	CC02
1	Electronic Device Battery		FNI	5.3×10 ¹⁴	2	Cell03
1	Li AA, 3.6V, 2.6Ah	Li-SOCl ₂	FNI	5.3×10 ¹⁴	2	AA02
1	18650, 3.7V, 2.6Ah	LiMnNiO ₂	FNI	5.3×10 ¹⁴	2	18650B
1	Li AA, 1.5 V, 3Ah	Li-FeS ₂	FNI	5.3×10 ¹⁴	2	AA01
1	18650, 3.7V, 2000 mAh	LiMnNiO ₂	FNI	5.3×10 ¹⁴	2	18650A
10	Activation Foils: Fe, Zr, Mg, V, Al, In, Au, Cu, Ni		FNI	5.3×10 ¹⁴	2	

*Fluence numbers are based on reference materials provided by the reactor facilities.

C.5.b. Acquisition of Gamma Spectra

The gamma spectra from the TRIGA exposures were collected by on-site staff using calibrated Ge detectors, where the battery samples were placed in the system to measure the spectrum. The ADC channel to energy conversion terms were provided by OSU staff as well as the detector efficiencies.

RMD was responsible for the data sets from UMass using a stand-alone Ge detector. The batteries were placed at a measured distance from the face of the detector. Test sources were used to calibrate the spectrum into energy terms. Due to the geometry of the battery and Ge, a c++ code was used to calculate the geometrical efficiency of intercepting gamma rays emitted from the battery. The only assumption in this code is that all of the gamma rays are emitted over the entire volume of the battery. For clarification purposes, the hit pattern on the face of the Ge detector is shown in Figure 15 for two different battery geometries, giving noticeably different efficiency. Once a gamma ray is intercepted by the Ge detector, the detector has a defined efficiency for

completely stopping the gamma ray, providing a full energy peak in the spectrum. Test sources with known activities were placed a long distance from the face of the Ge detector, simulating a point source. After the gamma spectra were collected, the efficiency was calculated (see Figure 16) and revisited after the second exposure at UMass. The data in Figure 16 show the measured efficiency from the first run (black squares) and the second run (blue circles). The red star is an extrapolated estimate at 2754 keV from the aluminum activation foils based on the known efficiency at 1368 keV. The point at 7 MeV is an estimate of the efficiency at germanium's minimum attenuation coefficient, which is used to keep the fit low. Data above 2754 keV or below 122 keV are not analyzed, as this is outside the region of calibration.

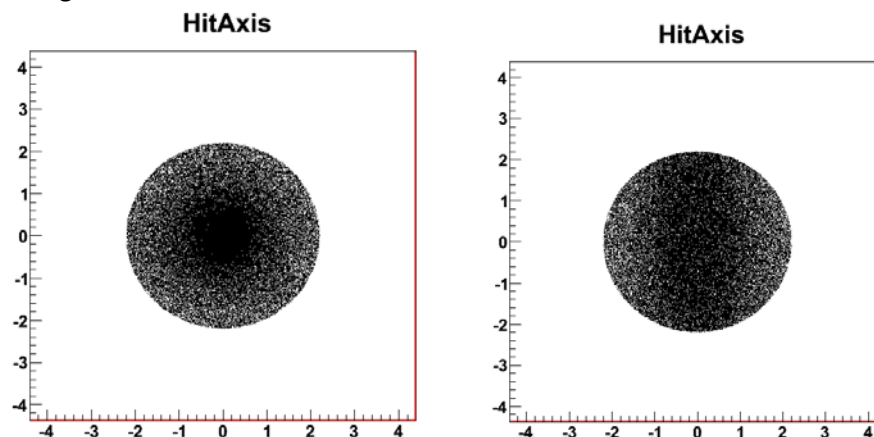


Figure 15: Example hit patterns simulated on the face of the Ge detector for a disk (left) and rectangle (right).

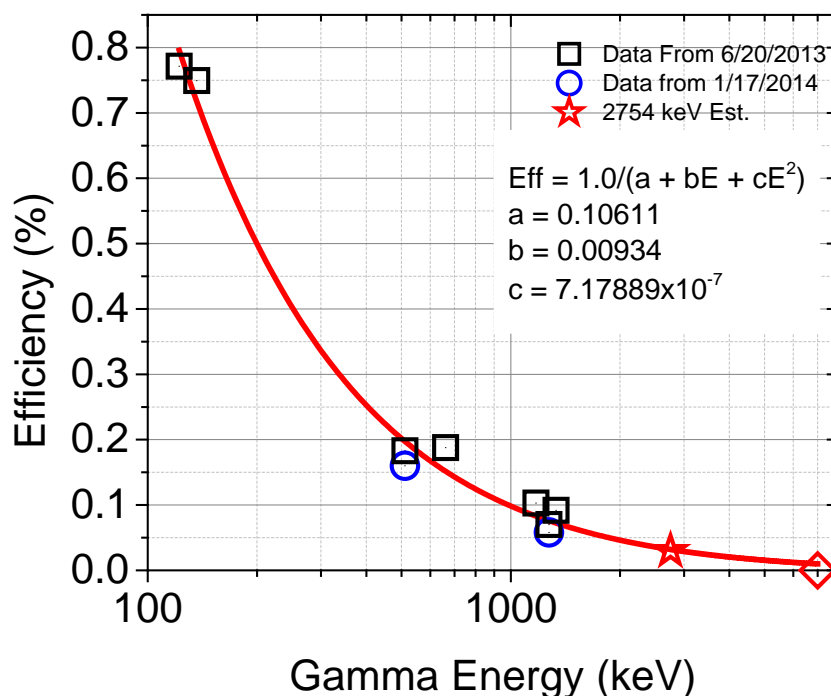


Figure 16: Detection efficiency of the germanium detector.

The gamma spectra were collected over multiple days. This allows for measurements of radioisotopes with differing half-lives. Longer lived half-live isotopes can be obscured by highly active materials. At least two spectra were collected from each battery, while the collection times were recorded to allow for calculation of the

initial activities of the batteries right after exposure. An example of the spectra after 1 day and 3 days is shown in Figure 17, allowing for a measure of the activity of more isotopes.

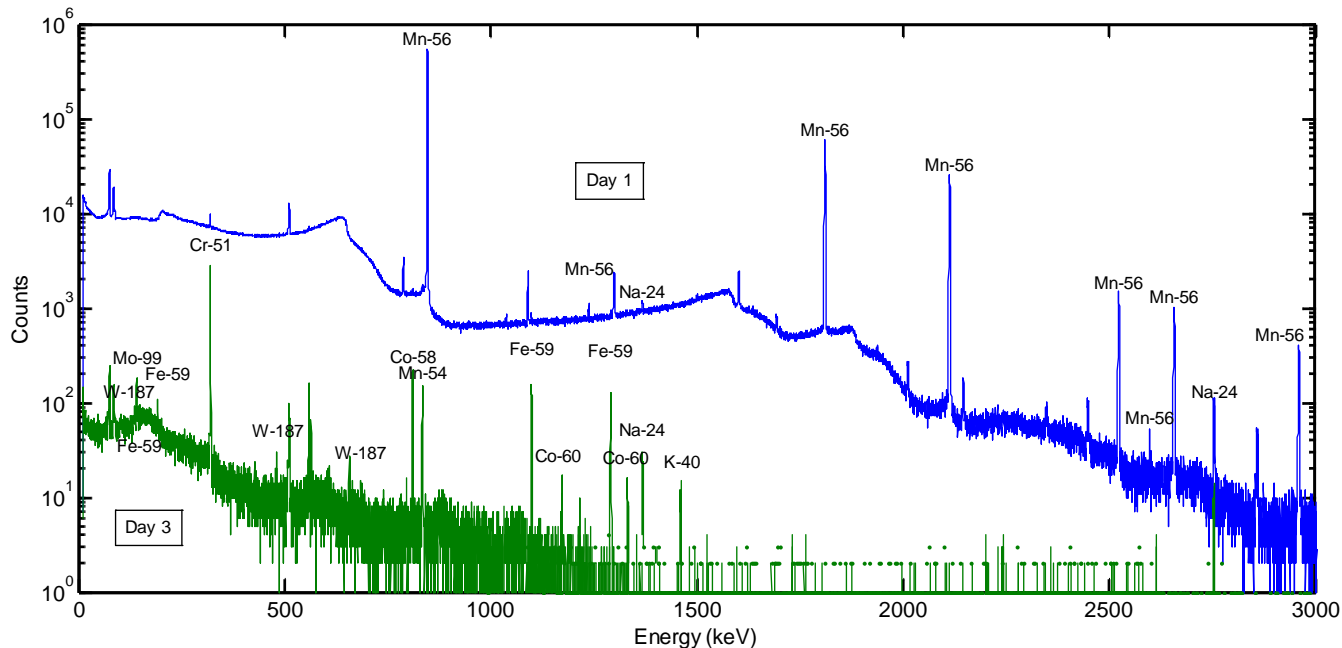


Figure 17: Gamma spectra obtained 1 and 3 days after irradiation for one LiMnO_2 battery.

C.5.c. Detection of Tritium Decay

Tritium decays by emitting beta particles with an end point energy of 18.59 keV and a mean energy of 5.69 keV. The range of these particles in all media is very short, and they will not escape from the battery. To extract the tritium information from the battery, the battery needs to be pried open and inserted into a scintillation medium. We chose Universol liquid scintillator cocktail from MP Biomedical.

The first attempt at extracting the tritium from the battery was not successful. The procedure was to pry open the battery at room temperature, remove the parts individually and place them into vials filled with liquid scintillator. In one instance, the battery cathode from the VL2020 (CC04) battery was placed in the vial. A vial, termed blank, with exactly the same amount of liquid scintillator and nothing else was used as a means to measure the ambient background in the room. Three initial measurements were made to illustrate the issue of the procedure. Spectra with the vial filled with the cathode, the blank vial (background), and without any liquid scintillator (PMT only) were collected and are shown in Figure 18. The data show that each of the spectrum is similar, indicating that no signal is being measured. The histogram of spectrum collected just with the PMT without any scintillator is given for reference. The electronics are setup correctly, as one sees dark counts from the PMT. When these vials of scintillator are exposed to gammas (60 keV) from ^{241}Am , a distinct peak is observed, and the issue is that the majority of the tritium escaped during the process.

The second attempt corrects these problems. First off, a major component of the battery is the electrolyte, which is where the major portion of the tritium will be located. This is because lithium ions will be diffused in the electrolyte, where some will be located in the anode or cathode depended on the power charge state of the battery. The electrolyte has a high vapor pressure at room temperature, indicating that the electrolyte will evaporate when the battery is opened. To overcome this obstacle, the entire battery was placed in a dry ice and methanol bath. Once a battery was frozen, it was pried apart and placed in a vial of liquid scintillator.

The same procedure was used to collect signal and background spectrum. The presence of the battery in the vial attenuates the light signal from the liquid scintillator, and separate ADC to energy calibrations were made for the battery and blank vials. The spectra were then rebinned, and the differential spectra are shown in

Figure 19. There was a noticeable signal in this second measurement. There are some noticeable issues with the second spectrum that will be cleaned up in the future before tritium counting is done. For the blank vial, the 60 keV peak from the ^{241}Am source is noticeable and significantly above the baseline background, while for the vial with the battery inside, this is not the case. The electrolyte diffuses into the scintillator giving it a brownish color, and with the battery, the light yield is low for this system. As shown in Figure 19, there are signals with fairly high energies. Part of this issue is that the resolution is poor. The resolution for the blank vial is 36% at 60 keV, suggesting that counts above 40 keV in the Signal (blue) histogram are from other radiation sources in the battery. This analysis is ongoing, and more information will be provided in the final report.

Initial Procedure for Coin Cell Batteries:

These batteries are assembled by mechanically pressing the anode and cathode terminals together. The following is the plan used for Figure 19.

1. Place battery in ethanol and dry ice bath for 15 min.
2. Place tips of tools used to pry open battery into dry ice bath for 15 min.
 - a. Needle nose pliers were used.
 - b. The tips should be cold as to keep battery frozen.
3. Fill glass jar with liquid scintillator cocktail (MP Biomedical Universol Liquid Scintillator)
4. Measure back ground spectrum with no batteries.
5. Use tools to pry open battery.
 - a. This should be done slowly.
 - b. Dip into the dry ice bath repeatedly.
6. When battery is open, place in liquid scintillator.
 - a. An open battery implies that the anode and cathode are physically separated.
 - b. The bubbles formed immediately when the battery was placed in the scintillator.
7. Cap the jar immediately.
8. Wrap the exterior with Teflon tape.
9. Use optical grease (BC630) to couple to a PMT.
10. Measure spectra.

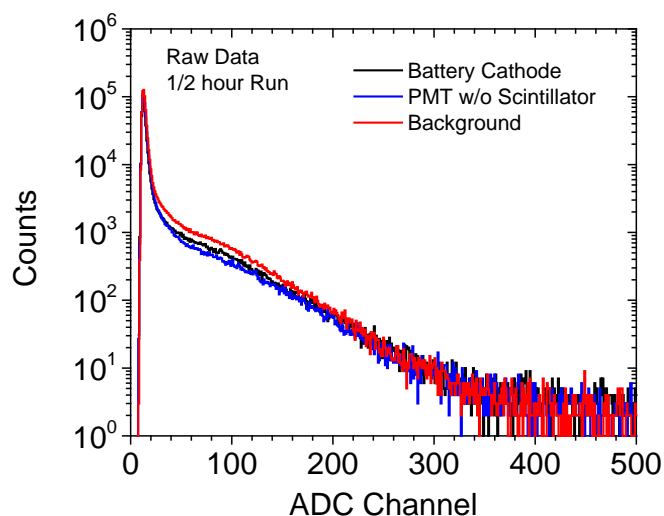


Figure 18: Spectra of three different measurements made with liquid scintillator. The battery cathode is placed in a vial with liquid scintillator, as the background is measured with no material in a vial filled with liquid scintillator. The PMT without a scintillator is also provided for reference.

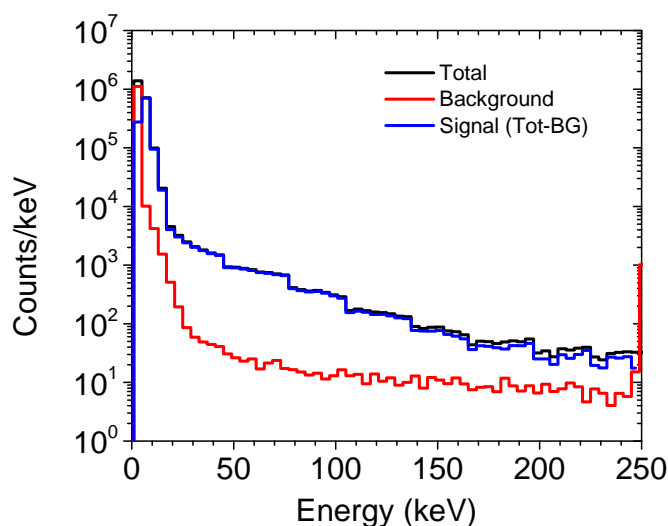


Figure 19: Differential spectra obtained using the more advanced method for extracting tritium information from the battery. The blue curve is the background subtracted signal, which may have contribution from tritium and other sources.

The procedure used to generate the data in Figure 19 includes gamma emission from the batteries in the signal spectrum. To achieve a more accurate account of the beta emission, the batteries were placed in the liquid scintillation material prior to being opened. The second issue mentioned is that the batteries attenuate the light output (transferred) to the photomultiplier tube. A new procedure is used for the remaining coin cell batteries to correct these issues. The batteries were placed in the filled glass jar while they are taped to the lid of the jar using white electrical tape. Note that low energy gamma rays (<20 keV) emitted from the battery will penetrate the electrical tape, but they may not penetrate the metal lid or glass. The gamma emission spectrum of an opened battery will be different compared to the closed battery due to self-attenuation. For the analysis conducted at this point, this effect is not accounted for here. A picture of a coin cell battery attached to the lid of the jar using electrical tap is shown in Figure 20. The jar is then wrapped with Teflon tape and placed on a 2-inch PMT. The liquid scintillator does react to the glue on the tape at a slow rate, and the measurements were taken immediately after the jar was filled with scintillator. When the measurement was completed, the battery and tape was removed from the scintillation material.

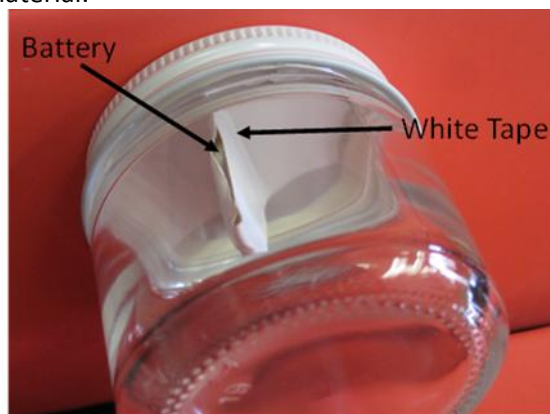


Figure 20: Picture of a coin cell battery placed in a glass jar. The battery is taped to the lid of the jar with white electrical tape. The jar is not filled with liquid scintillator.

The process of opening the battery was then approached. This process included freezing the battery in a dry ice/methanol bath. The battery was opened by bending the formed metal casing away from the battery

package on a cold plate, as shown in Figure 21. The casing is pried open using a small, hardened screwdriver with a small enough tip to get between the top and bottom casings of the battery and driven with a hammer. The process included repeated dipping of the batteries and tools to maintain cold conditions, as well as ensuring the cold plate remained cold, particularly around the battery. Once the battery was pried open, it was placed in the bath until the glass jar was ready for the battery.

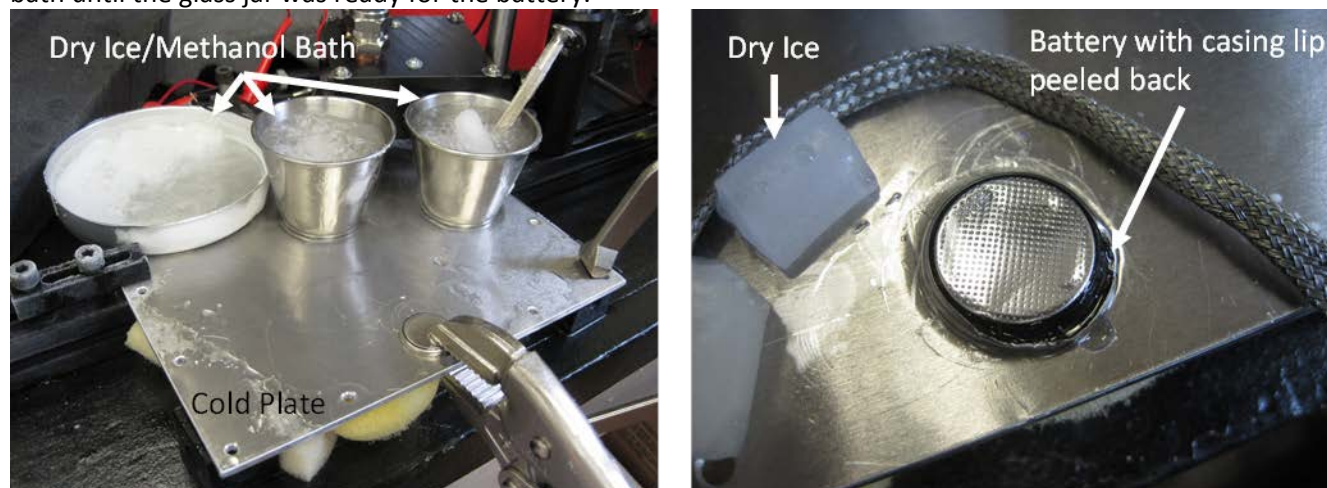


Figure 21: The left picture is the cold plate that was constructed for prying open the battery. The plate is covered with a thin layer of ethanol to maintain good thermal conduction, and the battery is clamped with a vice grip pliers. The right picture shows the battery partially opened. The procedure includes placing dry ice near the battery as the battery is opened.

The batteries were then placed in the glass jar by affixing them to the lid of the jar using super glue. A vicious glue was selected to form a thick layer to allow the battery to be placed on the lid and adhere properly. Each of the battery parts was removed from the bath and placed in the glue bead on the lid. The metal casings were placed first on the lid, with the inner components placed last. The coin cell batteries have only a few parts, and a picture of the assembled jar is shown in Figure 22. The picture is taken from the bottom of the jar up toward the battery components affixed to the jar lid after the jar was wrapped with Teflon tape. The assembled sample was then placed on a PMT for measuring the emission spectrum.

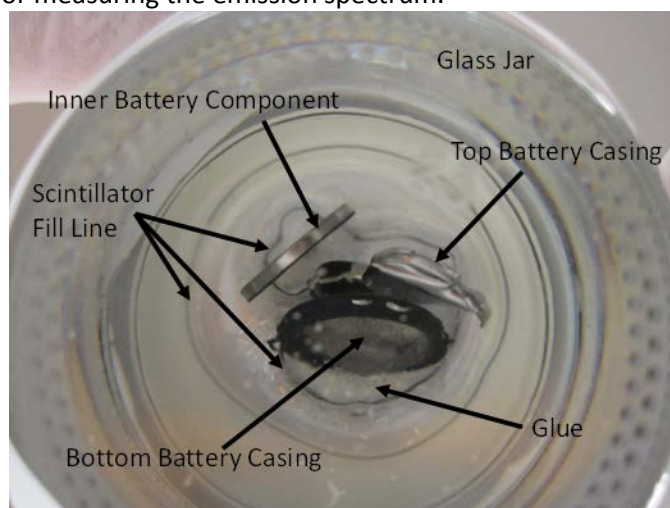


Figure 22: The picture is taken looking up into the assembled sample. The glass jar is marked with dimples around the edge. The battery parts are glued to the lid of the jar, which was wrapped with Teflon tape. The jar lid uses a rubber-like seal around the edge, while the glue and batteries are submerged into the liquid scintillator. These two structures provide the fill line marked in the picture, where a small air bubble surrounds the battery.

Final Tritium Extraction Procedure and Setup:

Spectrum Collection Setup Materials and Settings:

1. The glass jar (Uline S-15846M) is filled with liquid scintillator (Grainger 6LTX7, MP Universol Liquid Scintillator Cocktail).
2. The glass jar is wrapped with Teflon Tape (McMaster Carr 4591K14)
3. The batteries are affixed to the lid using instant bonding adhesive (McMaster Carr 7608A55)
4. The glass jar is optically coupled to the PMT, photomultiplier tube (Hamamatsu R6231-100) using optical silicone grease (Saint-Gobain BC630).
5. Additional wrapping of the glass jar to the PMT is done at the joint between the two with Teflon tape.
6. The PMT is biased to -900 V using a standard NIM crate HV module.
7. The PMT signal is connected to a charge-sensitive preamplifier (Cremat CR-111) through a interfacing PCB (Cremat CR-150).
8. The bias input to the CR-150 is terminated through 50 Ω .
9. The output on the CR-150 is terminated through 50 Ω at the input to a standard NIM module shaping amplifier.
10. The shaping amplifier is set to a shaping time of 250 ns.
11. The pulse height of the shaped signals are captured using a MCA, multi-channel analyzer (Amptek MCA8000A)
12. The data was transferred to a computer using Amptek's interface GUI and analyzed.

Procedure for Opening Coin Cell Batteries:

1. Fill jar with liquid scintillator to the lip of the jar.
 - a. The jar must be glass, as the scintillator will react with some plastics.
 - b. The jar must use a metal lid.
 - c. The plastisol liner on the lid provides a leak proof seal.
2. Label jars with battery identifier
3. Tape battery to lid using white electrical tape.
4. Screw lid/battery onto jar, submerging battery into scintillator.
5. Wrap jar with Teflon tape around the sides.
6. Apply silicone grease to jar's bottom to interface with the PMT.
7. Place the jar on the PMT and wrap Teflon around the jar and PMT at the joint between the two.
8. Surround the PMT with lead to reduce ambient background.
9. Enclose the PMT in a dark box and apply HV.
10. Collect 15 min of data.
11. Take a second run while exposing the assembly with a known test source, such as ^{241}Am , for calibration of the spectrum into keV.
12. Remove the Teflon tape, battery and electrical tape from jar.
13. Setup a cold plate and dry ice/methanol bath.
14. Freeze tools and batteries in dry ice bath.
15. Clamp the battery to the plate and pry back the battery casing to open the battery.
 - a. Place dry ice on the cold plate to ensure the battery remains cold during the prying process.
 - b. Repeatedly dip the battery and tools in the dry ice bath to keep the battery cold.
 - c. Use a film of ethanol on the cold plate to maintain good thermal conductivity.
16. Once the casing is pried back, place the battery parts into the dry ice bath.
17. Place the jar lid on the cold plate.

18. Score the jar's lid to allow of adhesion with the glue to the lid.
19. Put a large bead of glue on the lid such that glue will form up and around the battery's edge that is adhering to the lid.
20. Wait for a few minutes as the glue begins to set.
21. Attach the battery parts to the lid
 - a. Remove the casing or external parts of the battery first from the dry ice bath, as the electrolyte is expected to be primarily within the internal parts of the battery.
 - b. Shake off any excess ethanol from the battery parts.
 - c. Place the parts standing up, such that when the lid is secured the majority of the part is submerged into the liquid.
 - d. The adhering process is precarious, and the parts may need to set against each other to ensure they are standing up during the adhesion process.
 - e. Though not used in this procedure an accelerator might be used to speed up the curing process.
22. Screw the lid to the jar.
23. Repeat steps 5 – 11 to collect spectrum of the opened battery.

The spectrum was then analyzed to obtain a measure of the tritium content. The spectrum from ^{241}Am exposure is used to calibrate the battery spectra into keV. A plot of one of the ^{241}Am spectra is shown in Figure 23. The fit on the peak provides the scaling factor 60 keV/peak in ADC channels. The fit parameters are shown, as the fit is Gaussian and line to approximate the background underneath the 60 keV peak. Note that w is 1σ for the Gaussian distribution, indicating a resolution of 39% (FWHM) at 60 keV. This implies that the tritium betas with a mean energy of 5.69 keV (end point of 18.59 keV) will be distributed over a region extending up to 30 keV or more.

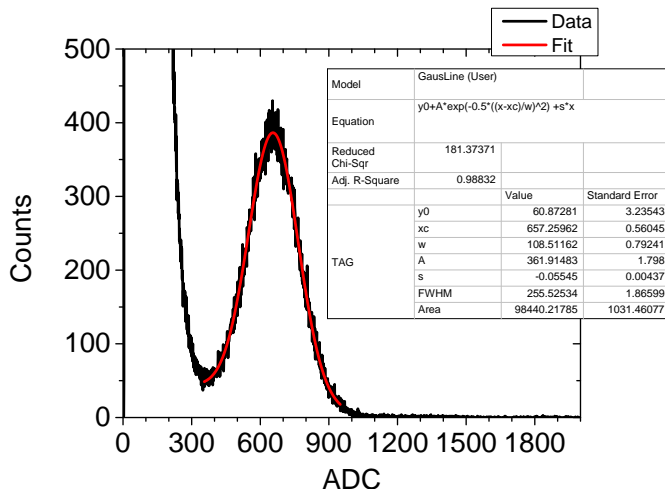


Figure 23: Plot of the 60 keV peak in the ^{241}Am spectra measured from the liquid scintillator assembly.

The signal data was then rebinned into 4 keV bins for both the opened and closed battery spectrum. This is done to allow proper subtraction of one spectrum from the other. The light yield per 60 keV gamma is less for the open batteries compared to the closed ones, to the absorption surfaces from the exposed batteries. The differences between the real and live times (due to dead time in the spectrum collection process) is accounted for to maintain a correct number of counts for each spectral bin. The results from one of the batteries is shown in Figure 24.

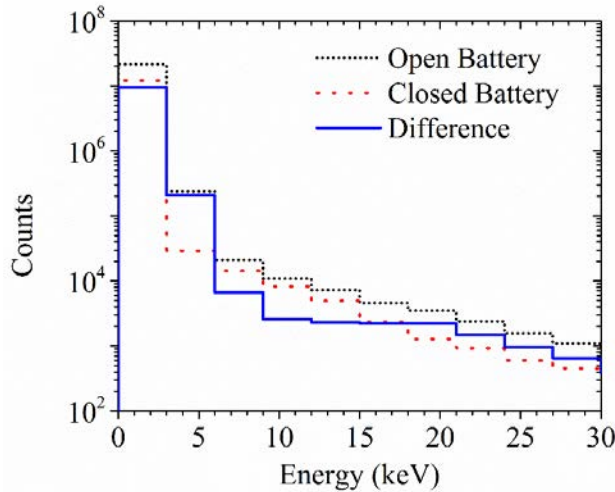


Figure 24: The black histogram is the total counts when the battery was opened within the scintillator, and the red histogram is when the battery is closed. The blue histogram is the difference.

The results provide only an indication of the tritium content. The battery is encased with a steel case, which will attenuate some of the low energy gammas generated within the battery when the battery is closed. As the battery is open, these gammas have a chance to generate a light flash within the scintillator. The tritium content with the battery should dominate though for two reasons. The first is that the tritium production is very high, not only from the lithium content but from other isotopic parents. The half-life is 12.32 years, indicating that the tritium content has not diminished significantly since the time of exposure. During the analysis process, the number of counts above 51 keV was measured to determine if the process successfully removed the background gammas. To estimate the tritium content, we also provide a measure of the number of counts from 3 to 30 keV to correlate with MCNP simulations. The 3 keV threshold is used to remove fluctuations from noise in the PMT/electronics. The data in Table XI provides these results. Each of the batteries was exposed at the UMass FNI facility.

TABLE XI
TOTAL DIFFERENTIAL COUNTS FROM OPENED BATTERIES

Model	Run	ID	Indicator	Counts 3-30 keV	Counts >51 keV	MCNP ³ H Counts	Ratio
VL-2020	1	CC04	Blue	224,571	-2,989	24,880	9.03
ML-2020	1	CC03	Gold	728,644	41	67,178	10.85
CR2032	2	CC02		568,937	27	185,999	3.06
CR2032	2	CC02	Orange	29,591	-418	186,086	0.16
LIR2032	2	CC01		353,687	-56,492	89,341	3.96
LIR2032	2	CC01	Orange	542,614	-37,297	89,341	6.07
Mean ± Error							6 ± 2

The MCNP counts are a total number of counts from the tritium production (FM4) tally. Ratio is the ratio of the 3-30 keV counts to the MCNP counts.

C.5.d. Mass Spectroscopy Analysis on Test Batteries

Material data were obtained by performing (destructive) inductively coupled plasma mass spectrometry (ICP-MS) on the batteries. As shown in Figure 25 and Figure 26, the batteries were disassembled into each of the assembled parts. As mentioned, battery assembly typically is the insertion and compression of materials with a diffuse separator, backfilled with an electrolyte. Once the case is pried open, these parts are easily separated from

each other and analyzed separately. Specific components were separated into smaller pieces and dissolved into acids in preparation for the ICP-MS analysis. Note that the electrolyte evaporated before the analysis was conducted and the organic compounds such as separator and gasket are not measurable by ICP-MS. Other components required back calculation (via stoichiometry and mass) to determine the mass content, while using particle induced x-ray emission and Rutherford backscatter spectrometry for carbon and oxygen content, respectively. Figure 27 shows the percentage of atoms within the battery volume for elements with a large content for a select few of the batteries. Further details of these results are shown in Table XXVI in the appendix. Typical natural abundances are used to determine isotopic content.



Figure 25: The CR2032 (CC02) LiMnO_2 battery and its components. Left to right: the positive side battery case, inside the positive side battery case, inside the negative side battery case, the MnO_2 electrode and the separator.

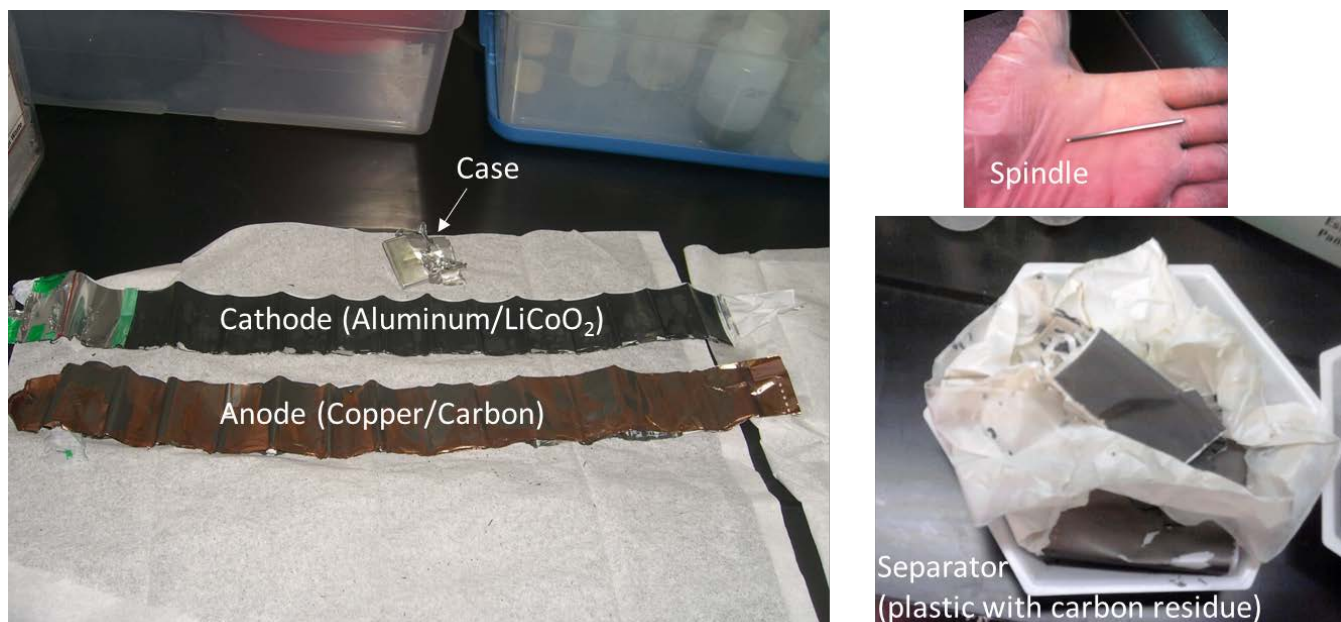


Figure 26: Disassembly of the Cell Phone (Cell01) battery. The anode and cathode are removed from the aluminum case and unrolled. A spindle used for the winding is shown in the upper left, as the separator is shown below. The black material on the separator is anode carbon that has been transferred to the separator.

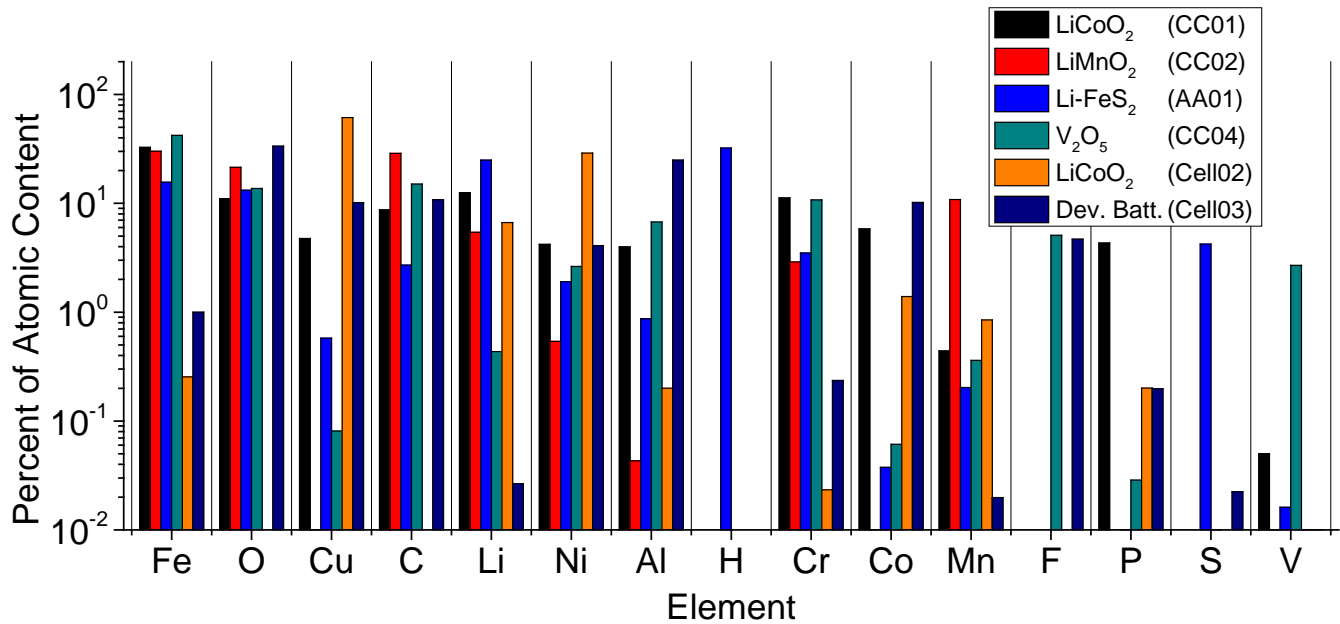


Figure 27: Chart of the elemental content within a select group of batteries measured with ICP-MS. The percentage of the total number atoms for each element is shown for the highest content elements.

C.6. Na-24 to Co-58 Activity Ratio

The spectra from the TRIGA and the FNI were collected for both of the 18650 batteries (18650A for TRIGA and 18650B for FNI) and are shown in Figure 28. Both of the spectra were collected roughly 24 hours after the exposure, and the 511 keV and 2754 keV peaks are noticeable in the spectra. The live time of the data collection was 1 hour for the TRIGA data and ½ hour for the FNI data. There are a few other lines that are visible in both spectra, but the relative intensity for the majority of the lines is distinct between each battery. The two batteries are made by two different manufacturers, which can account for some of the differences. We will provide more detailed information regarding the constituents for each battery once the mass spectrometry has been completed. There are a number of emission lines between 500 and 750 keV that are clearly visible in the FNI spectra but not in the TRIGA spectrum. These might be attributed to the slightly different alloys used in the battery. When we reduce the data to the nickel and aluminum content, the concentrations of these materials can be fairly close from battery to battery due to the basic consideration of the 18650 design. That is to say each 18650 should produce the same voltage and consist of the same types of safety features. If we make this assumption, then the ratio of the yield of 811 keV gammas from ^{58}Co , which arises from nickel reactions, to the yield of 2754 keV gamma from ^{24}Na (aluminum reactions) should be distinctly different. This ratio was determined for each battery, and it is expected that the FNI spectra should have a higher ratio, as ^{24}Na production has a higher associated threshold (3.25 MeV) than ^{58}Co (0 MeV). The ratio for the FNI spectra is 0.32 and is 0.12 for the TRIGA. The assumption here is that we are only considering the following neutron capture reactions associated with the production of ^{24}Na and ^{58}Co :

- $^{58}\text{Ni} (n,p) ^{58}\text{Co}$
- $^{60}\text{Ni} (n,t) ^{58}\text{Co}$
- $^{27}\text{Al} (n,a) ^{24}\text{Na}$

There are trace elements that may contribute to the production of ^{24}Na , but the battery is primarily made from aluminum. The production of ^{58}Co made also seeded from $^{59}\text{Co} (n,2n) ^{58}\text{Co}$ reaction, yet these reactions have a threshold energy ~ 10 MeV and with low cross sections.

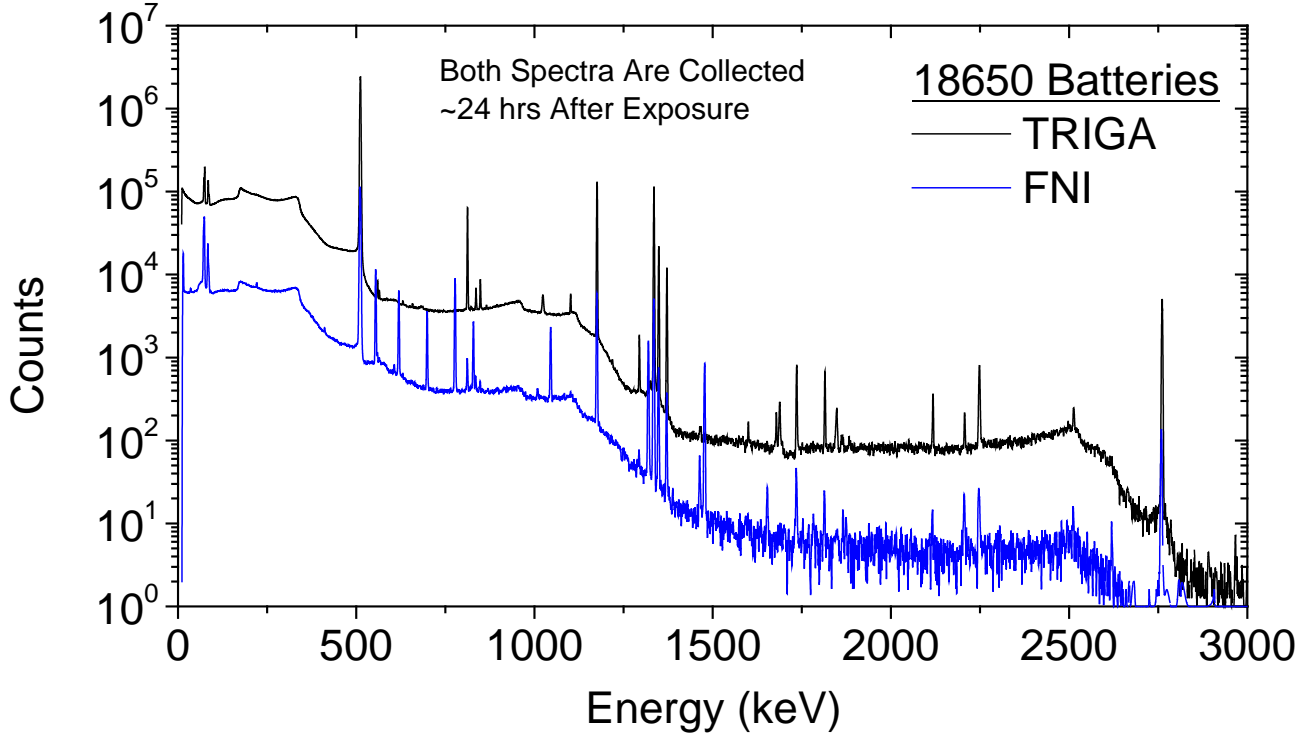


Figure 28: Gamma spectroscopy results obtained from both of the 18650 batteries. The blue line is associated with the FNI exposure, and the black line is from the TRIGA exposure. The spectra were collected roughly 24 hours after the exposure, but the live times are 1 and ½ hr for the TRIGA and FNI spectra, respectively. The geometry and distance from the Ge detectors are different as well.

C.7. Activation Analysis Study on CR2032 (CC02) LiMnO₂ Batteries

This study looks are further validating the method by explicitly looking at the CR2032 (CC02) battery. The objective being that once the model was validated, subsequent MCNP simulations could be carried out to assess the feasibility of using the batteries in a post-detonation role.

Brode estimates the fluence from a nuclear weapon using [8]

$$\Phi = \frac{2 \times 10^{22} \text{ n/cm}^2 \cdot Y}{r^2} e^{\frac{-\rho r}{2.38 \times 10^4 \text{ g/cm/L}}} \quad (4)$$

where Y is the yield in kt; r is the distance; and ρ is the air density ($1.225 \times 10^{-3} \text{ g/cm}^3$). Accordingly, at distances from 800 to 1600 m, the fluence from a 10 kt detonation ranges from 3×10^{13} to $8 \times 10^{12} \text{ n/cm}^2$.

C.7.a. Exposure Conditions

An initial test had the batteries placed in the in-core irradiation tube (ICIT) of a TRIGA reactor that operated at 10 kW for 27 minutes. These irradiation parameters produced a thermal neutron fluence of approximately 10^{14} n/cm^2 . In order to eliminate the shielding effect obtained from the first experiment, each sample was placed individually in a pneumatic transfer tube (rabbit) and exposed to the reactor running at full power (1 MW) for 30 seconds to obtain a fluence of about 10^{14} n/cm^2 to match the first experiment. Since the activity level at the third day from the first experiment was too low, two sets of sample counting were conducted 1 day and 2 days after irradiation. All sample counting used the same detector system to remove the differences introduced by the multiple detector efficiencies, as observed in the first experiment.

C.7.b. MCNP5 Model Setup

IA heterogeneous model was realized by disassembling and paying close attention to the geometry of the real batteries. For the non-rechargeable LiMnO₂ battery, the geometry was simple and accurately reflected using

caliper measurements. The images of the disassembly of the battery are seen in Figure 25. With the information obtained from ICP-MS (see Table XXVI in the appendix), the material specification of the battery model was established within MCNP5. Figure 29 presents the LiMnO_2 heterogeneous battery model.

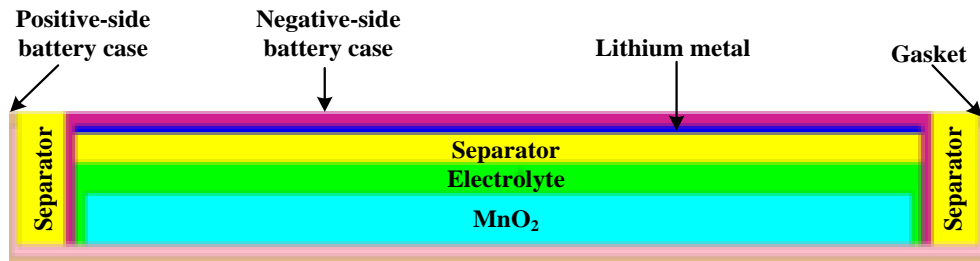


Figure 29: MCNP model of LiMnO_2 coin-cell battery. From top to bottom, the interior layers are negative-side battery case, lithium metal electrode, separator, electrolyte, MnO_2 electrode, and steel ring around MnO_2 (which is essentially too thin to be seen). The outer circumference is the gasket, and the thin peripheral covering is the positive-side battery case.

C.7.c. Reactor Experiment Modeling

The neutron source depiction chosen for the reactor battery simulations was an inward spherical distribution of radius 27.35 cm. The spherical distribution is believed to accurately reflect the environment of the nuclear reactor irradiation positions, in which neutrons would likely be travelling from all directions. The 27.35 cm radius was chosen because it would fit the stack of batteries and leave space around them, in addition to giving a similar size to the height of the ICIT. The experimental fluence was matched by using an f5 point flux tally in the center of the sphere to measure the simulated flux. The f5-tally-simulated flux was equated to the experimental flux and the initial source weight to determine the proper source weight. The reactor source spectrum came from foil measurements and STAYSL reconstruction data [9].

All of the battery models were run with 500 million particle histories to maintain consistency between models and allow most statistics to pass. The specific reaction tallies were selected with the gamma spectra from the reactor experiments in mind. The possible parent nuclei were considered for each radioisotope, and the possible reactions with the largest cross-sections were tallied using f4 cell flux tallies with material tally multipliers. Table XII provides the number of reactions estimated for the outer and inner LiMnO_2 batteries in the first experiment as well as the sole LiMnO_2 battery in the second reactor experiment. These three batteries are designated LiMnO_2 -1, LiMnO_2 -2 and LiMnO_2 -3, respectively.

Non-zero threshold reactions would permit limited reconstruction of the original neutron spectrum as they would serve as threshold detectors. Table XII shows that $^{55}\text{Mn}(n,\gamma)$ reaction produces about 4500 times more ^{56}Mn than does the $^{56}\text{Fe}(n,p)$ reaction; thereby rendering the 3.0 MeV threshold of the latter reaction of little use for spectral reconstruction. Likewise, the $^{23}\text{Na}(n,\gamma)$ reaction overwhelms the $^{27}\text{Al}(n,\alpha)$ reaction in the production of ^{24}Na , hence eliminating the latter reaction as an effective threshold detector.

TABLE XII
MCNP ESTIMATED NEUTRON REACTIONS IN LiMnO₂ BATTERY

Reaction(s)	Number of Reactions		
	LiMnO ₂ -1	LiMnO ₂ -2	LiMnO ₂ -3
⁵⁸ Fe(n,γ) ⁵⁹ Fe	8.46E+09*	7.53E+09*	7.98E+09*
⁵⁶ Fe(n,p) ⁵⁶ Mn	1.35E+09	1.27E+09	5.96E+08*
⁵⁵ Mn(n,γ) ⁵⁶ Mn	6.36E+12	5.54E+12	9.69E+12
⁵⁰ Cr(n,γ) ⁵¹ Cr	8.70E+10	7.71E+10*	1.30E+11*
²⁷ Al(n,γ) ²⁸ Al	1.09E+08	1.06E+08	1.89E+08
²⁷ Al(n,α) ²⁴ Na	4.21E+05	4.28E+05*	1.97E+05
²³ Na(n,γ) ²⁴ Na	1.18E+09	1.02E+09*	1.81E+09*
⁵⁹ Co(n,γ) ⁶⁰ Co	4.79E+08	4.89E+08*	5.76E+08*

Results for a 10¹⁴ n/cm² fluence in the TRIGA. * Denotes tallies that did not pass all ten statistical checks in MCNP, which used 300 to 600 million histories.

The number of reactions occurring in the batteries during simulated reactor neutron exposure is obtained and converted to an activity as listed in Table XIII. The measured activity is also recorded for comparison. For ²⁸Al, the half-life is only 2.3 min, so it had decayed significantly by the time counting was performed. The difference in the measured activities of batteries 1 and 2 can be attributed to the fact that all six batteries were stacked together when exposed in the reactor. The LiMnO₂ batteries were on the bottom of the stack, topped by the LiFePO₄, LiMnNiCoO₂, and LiCoO₂ batteries. Hence, the batteries on the periphery partially shield interior batteries, leading to a higher activity for the bottom battery (LiMnO₂-1) compared with the other (LiMnO₂-2) cell. Another reason causing the difference is the efficiency of the HPGe detectors. The measurements were subject to available counters and these two LiMnO₂ batteries were counted by two different detector systems. The detector used for the outside battery (LiMnO₂-1) had twice the efficiency as the one used for the interior battery (LiMnO₂-2). These results imply that in the actual utilization of this approach, a portable detection system with a higher efficiency is preferred. Other differences in the measured and simulated activities for the batteries are attributed to the assumptions made in the MCNP modeling (e.g., material densities were taken as standard values and components of less than 1 ppm concentration were omitted, and the geometry of Figure 25 is somewhat idealized), the ICP-MS measurement error (~10%), and the statistical error in the MCNP simulations. In addition, ICP-MS was not performed on the plastic or cellulose battery components, rather they were assumed to be polypropylene. To double-check the measurement of the MnO₂ cathode, the complementary techniques of Particle Induced X-ray Emission (PIXE) and Rutherford Backscatter Spectrometry (RBS) were performed. For instance, PIXE found 21 wt% of carbon, while by process of elimination, ICP-MS implied 26 wt% C.

TABLE XIII
COMPARISON OF ACTIVITIES FROM EXPERIMENTAL MEASUREMENTS (TIME CORRECTED) AND MCNP SIMULATION

Radionuclide	LiMnO ₂ - 1 (Outer)		LiMnO ₂ - 2 (Inner)		LiMnO ₂ - 3 (Alone)	
	Measured Activity (μCi)	MCNP Estimated Activity (μCi)	Measured Activity (μCi)	MCNP Estimated Activity (μCi)	Measured Activity (μCi)	MCNP Estimated Activity (μCi)
Mn-56	14,600	12,200	11,800	9,800	16,300	20,600
Cr-51	0.671	0.565	0.564	0.548	0.741	0.747
Na-24	0.0855	0.388	0.074	0.310	0.113	0.466
Fe-59	0.025	0.040	0.0187	0.029	0.04	0.028
Al-28	< MDA	14.0	< MDA	11.6	<MDA	19.4
Co-60	0.00127	0.00005	0.00110	0.00005	0.001	0.00005

Batteries number 1 and 2 are the results from the first experiment. Battery number 3 is the results from the second experiment. MDA = minimum detectable activity.

C.7.d. Weapon Exposure Modeling

The LiMnO_2 model was then subjected to three different 10 kt nuclear weapon spectra. The simulations were divided into two calculations. The first computation, which utilized deterministic transport (DXTRAN), found the neutron spectrum as a function of distance from air zero—the point of detonation. A second calculation employed an inward spherical source based upon the DXTRAN results.

The source spectra for the DXTRAN simulations were obtained from the literature. The weapon output spectra for the Little Boy (U-235 gun-type device) and Fat Man (Pu-239 implosion device) were taken from [6]; the spectrum from a thermonuclear device was found in [1]. The spectra from these three bombs at 1 km are compared in Figure 30. As seen in the graph and as noted by Whalen, the output neutron spectrum from Little Boy was harder than Fat Man because the latter employed “tons of high explosives” that moderated the output neutron spectrum significantly [6].

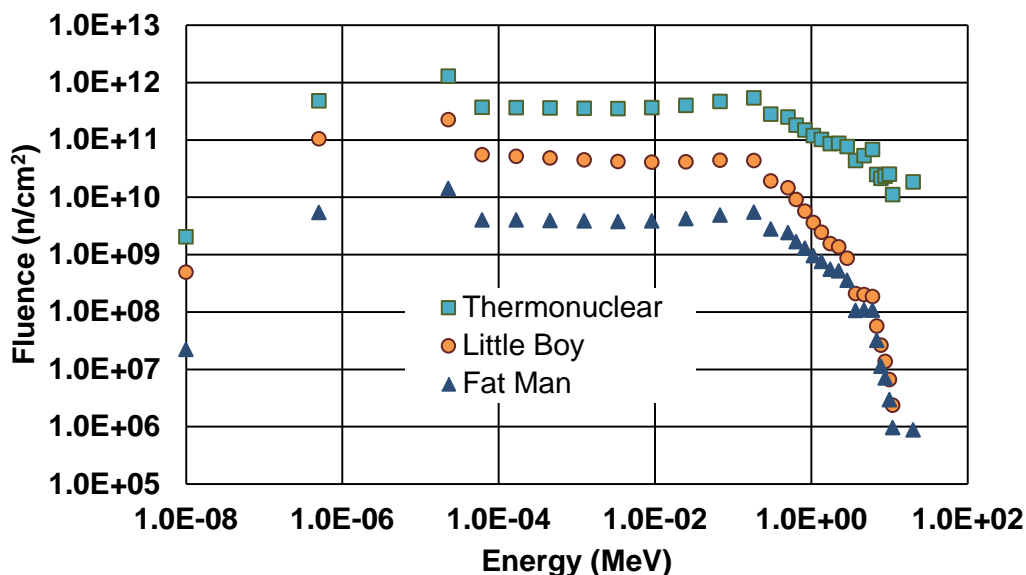


Figure 30: Simulated neutron spectra from Little Boy, Fat Man and thermonuclear devices at 1 km.

The distance at which a lithium battery will receive a significant fluence of neutrons is determined by the weapon type, as well as the number of obstacles between the battery and the epicenter. Varying distances from the point of the 10 kt nuclear weapon detonation are simulated and the results show that 1 km is a reasonable distance because it is close enough for batteries to absorb sufficient numbers of neutrons, yet it is far enough that batteries will not be destroyed.

Subsequently, the LiMnO_2 battery model (Figure 29) was exposed to each neutron spectrum. Similar to the reactor experiment, the number of reactions in the main battery materials were computed, and these are presented in Table XIV. As a first observation, the number of reactions induced by the nuclear weapons at 1 km are very roughly an order of magnitude smaller than those from the reactor experiments (Table XII). This implies lower count rates and the need for longer gamma spectra measurement periods. Second, the number of reactions from the non-zero threshold reactions are even more so negligible as compared to the thermal reactor experiment results. The fact that most of the statistical checks for the non-zero threshold reactions were not all passed becomes unimportant in the computation of the induced activities of those radionuclides, since they are several orders of magnitude smaller than the zero threshold reactions.

TABLE XIV
MCNP ESTIMATED NEUTRON REACTIONS IN LiMnO₂ BATTERY

Reaction(s)	Number of Reactions from 10 kt Device at 1 km		
	Gun Type	Implosion Type	Thermonuclear
⁵⁸ Fe(n,γ) ⁵⁹ Fe	2.08E+09*	1.60E+09*	1.26E+09*
⁵⁶ Fe(n,p) ⁵⁶ Mn	1.82E+07*	1.42E+08*	5.05E+09*
⁵⁵ Mn(n,γ) ⁵⁶ Mn	2.18E+12	1.52E+12	1.36E+12
⁵⁰ Cr(n,γ) ⁵¹ Cr	2.39E+10*	1.55E+10*	1.39E+10*
²⁷ Al(n,γ) ²⁸ Al	3.69E+07	2.48E+07	2.30E+07
²⁷ Al(n,α) ²⁴ Na	3.90E+03*	3.17E+04*	1.84E+06
²³ Na(n,γ) ²⁴ Na	3.72E+08	2.52E+08	2.28E+08*
⁵⁹ Co(n,γ) ⁶⁰ Co	2.32E+08*	1.95E+08	1.66E+08

* Denotes tallies that did not pass all ten statistical checks in MCNP, which used 500 to 700 million histories.

Table XV converts the reactions of Table XIV into equivalent initial activities. As expected, the ⁵⁶Mn activity is the most significant. The induced activity in the other nuclides is somewhat low, which leads to larger measurement error and limited viable radionuclides at this distance. In fact, the activities for several do not compare well to the minimum detectable activity (MDA) or lower limit of detection (LLD) for reasonable count times and delay time between detonation and battery measurement.

TABLE XV
MCNP ESTIMATED INDUCED ACTIVITIES IN LiMnO₂ BATTERY

Reaction(s)	Induced Activity (μCi) from 10 kt Device at 1 km		
	Gun Type	Implosion Type	Thermonuclear
⁵⁸ Fe(n,γ) ⁵⁹ Fe	1.01E-02*	7.80E-03*	6.14E-03*
⁵⁶ Fe(n,p) ⁵⁶ Mn	3.67E-02*	2.86E-01*	1.02E+01*
⁵⁵ Mn(n,γ) ⁵⁶ Mn	4.40E+03	3.07E+03	2.75E+03
⁵⁰ Cr(n,γ) ⁵¹ Cr	1.87E-01*	1.21E-01*	1.09E-01*
²⁷ Al(n,γ) ²⁸ Al	5.14E+00	3.45E+00	3.20E+00
²⁷ Al(n,α) ²⁴ Na	1.35E-06*	1.10E-05*	6.40E-04
²³ Na(n,γ) ²⁴ Na	1.29E-01	8.76E-02	7.91E-02*
⁵⁹ Co(n,γ) ⁶⁰ Co	2.61E-05*	2.19E-05	1.87E-05

The LiMnO₂ battery is capable of determining both the device yield as well as the type of weapon.

C.7.e. Weapon Yield

Brode provided a single equation for the neutron fluence as a function of distance without revealing the weapon type. We find that the results from Eq. (4) deviate from the MCNP simulations. Therefore, three equations were developed separately for the Little Boy (LB), Fat Man (FM) and thermonuclear (TN) devices, shown as Eqs. (5), (6), and (7) respectively, in dry air. These equations have a difference of less than 6% in the ranges of 800–1600 m, 900–1700 m and 800–1900 m, respectively, for LB, FM and TN. The total fluence calculated using the equations from 900 m to 1300 m is plotted in Figure 31 and compared to the MCNP simulation results.

$$\text{LB: } \phi = \frac{7.42 \times 10^{23} \text{ n/cm}^2 \cdot \gamma}{r^2} e^{\frac{-\rho r}{1.80 \times 10^4 \text{ g/cm/L}}} \quad (5)$$

$$\text{FM: } \phi = \frac{1.21 \times 10^{22} \text{ n/cm}^2 \cdot \gamma}{r^2} e^{\frac{-\rho r}{2.38 \times 10^4 \text{ g/cm/L}}} \quad (6)$$

$$\text{TN: } \phi = \frac{5.73 \times 10^{23} \text{ n/cm}^2 \cdot \gamma}{r^2} e^{\frac{-\rho r}{2.77 \times 10^4 \text{ g/cm/L}}} \quad (7)$$

In a similar fashion, an empirical relationship between the number of reactions and the yield is developed with the assistance of the MCNP simulations. For the dominant radionuclide ^{56}Mn , the number of (n,γ) reactions as a function of distance for the two fission devices is

$$\text{LB: } N = \frac{9.86 \times 10^{21} r x s \cdot Y}{r^2} e^{\frac{-\rho r}{1.66 \times 10^4 \text{ g/cm/L}}} \quad (8)$$

$$\text{FM: } N = \frac{3.72 \times 10^{19} r x s \cdot Y}{r^2} e^{\frac{-\rho r}{2.64 \times 10^4 \text{ g/cm/L}}} \quad (9)$$

where r is in cm and Y is in kt. In the range 800–1200 m, these fitted relations are within 1.5% of the simulated results. Hence, using measured activities that are time corrected to the detonation time permits determination of the device yield, that is, the initial activity $A(0) = \lambda N$ where λ is the decay constant.

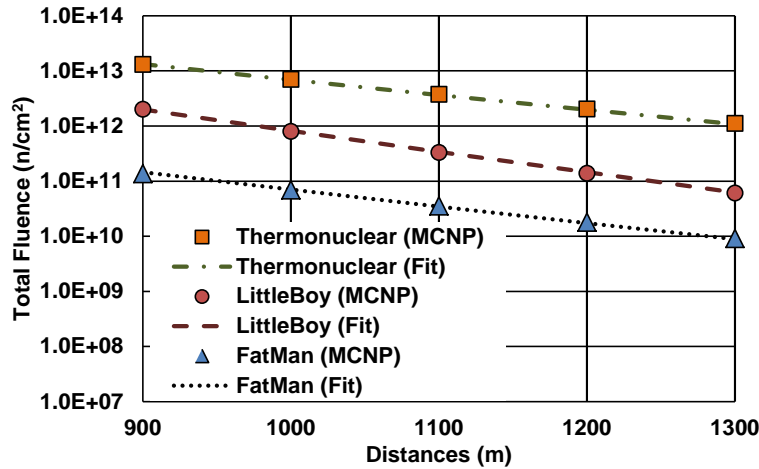


Figure 31: Comparison of MCNP computed fluence (symbols) and the fitted equation calculated total fluence (lines) for 10 kt Little Boy, Fat Man and thermonuclear devices.

C.7.f. Device Type

The device type can be inferred by measuring the activities of multiple batteries collected at various distances for particular radionuclides (i.e., reactions). For example, Figure 32 compares the number of induced reactions at 800 m to 1200 m from Little Boy and Fat Man. The graph clearly shows that the slopes of these two lines are different, specifically, the gun-type (Little Boy) device exhibits a steeper decline with increasing distance in comparison to the implosion (Fat Man) weapon. In particular, the LB results show a decrease by a factor of 43 from a distance of 800 to 1200 m, while FM only experiences a decrease of only a factor of 14. This means that one may distinguish the type of fission weapon, specifically whether the explosion is from a gun-type or an implosion device. This discrimination is a prerequisite to calculating the yield, as one must select from Eqns. (8) and (9).

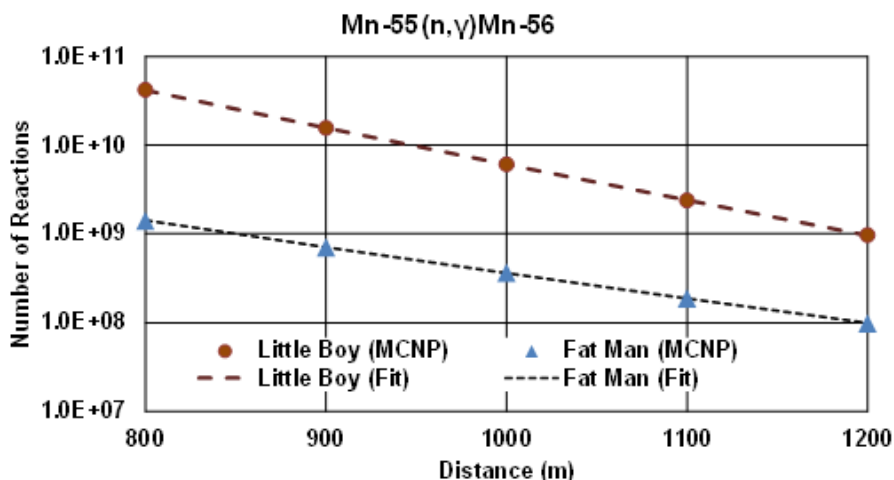


Figure 32: Comparison of the total number of $^{55}\text{Mn}(n,\gamma)$ reactions as computed by MCNP (symbols) and the fitted equation (lines) for 10 kt Little Boy and Fat Man type devices.

C.8. Spectral Reconstruction

C.8.a. Comparisons of the Gamma Spectra between MCNP and Data

Using the ICP-MS results, the geometry of each battery was built in MCNP. When taking each battery apart into its constituents, the weight and dimension of each part were recorded. The dimensions of some parts were measured using a caliper while other components were distorted. Therefore, the some of the dimensions of those parts were approximated. Various parts were inserted into the MCNP model for simulation, while some of the battery components, such as gaskets and the electrolyte constituents, were approximations.

While constructing the geometry, some difficulties appeared that might have led to error(s) in the results. The most challenging part is the electrolyte. As mentioned before, the electrolyte evaporates upon battery disassembly. Therefore, it is hard to identify its material and the mass. The mass was estimated as the difference between the weights measured before and after taking the battery apart. The material was assumed according to literature review of the most popular electrolyte material in similar kinds of batteries. For the LIR2032 (CC01) and ML2020-H1CN (CC03), the electrolyte is taken to be LiPF_6 . Because the small profile battery (Cell02) uses a solid-state electrolyte, it is assumed that the electrolyte material is included in the ICP-MS results. Another place that might cause error is that when taking the batteries apart, some parts are brittle and easily break into fine particles. It is possible that not all the tiny parts were collected to measure the weight and used for ICP-MS.

Once the geometry and the material of the batteries are determined, the input for the MCNP simulation can be completed. The LIR2032 (CC01) and iPod shuffle battery (Cell03) were irradiated in the Oregon State University TRIGA reactor. Whereas the small profile battery (Cell02) and VL-2020 (CC04) experiment was performed in the UMass Fast Neutron Irradiation facility. The neutron spectra of both reactors were obtained (see Figure 13) and used as the source spectrum in the MCNP input. F4 tallies were used in order to quantify possible reactions and activities of the reaction products. Table XVI to Table XVIII compare the MCNP simulated activities and the experimentally measured activities for batteries number CC01, Cell02, and CC04, respectively. During the MCNP simulation runs, one of the challenges that occurred is that for some reactions, it was difficult to pass all ten statistical checks. Some reactions passed all statistical checks at a low number of points (nps) but did not pass when the nps was high, while some reactions behave in the opposite manner. The solution for this problem was to run multiple simulations with increasing nps (from 200 million nps to 4,000 million nps). The final results were selected from those runs that passed all the statistical checks or had the smallest errors at different nps for each reaction.

The tables show that the percentage difference between the MCNP simulation and experimental measurements are as good as 3%. However, some of the errors are as large as 99%. This may be caused by the approximations of the dimension and density made when building the geometry. Another possible reason is that the actual source spectra that batteries were exposed to were different from what we obtained from the literature. This motivated us to reconstruct the source spectrum using SAND-II with some foil data obtained from the experiment to examine if the spectrum that was used is accurate and if the results could be improved.

TABLE XVI
MCNP ACTIVITY AND EXPERIMENT ACTIVITY COMPARISON FOR LIR2032 (CC01)

Product	MCNP Activity (uCi)	Experiment Activity (uCi)	Percent Difference
Mn-56	5.25E+02	5.61E+02	-7%
Cu-64	2.42E+02	1.43E+02	52%
Cr-51	2.65E+00	1.85E+00	36%
Co-60	5.11E-01	8.10E-01	-45%
Na-24	4.53E-01	2.52E-01	57%
Mo-99	6.27E-03	2.15E-02	-110%
Co-58	1.24E-02	2.37E-02	-62%
Fe-59	2.99E-02	2.55E-02	16%
W-187	1.68E-01	4.07E-01	-83%

TABLE XVII
MCNP ACTIVITY AND EXPERIMENT ACTIVITY COMPARISON FOR SMALL PROFILE BATTERY (CELL02)

Product	MCNP Activity (uCi)	Experiment Activity (uCi)	Percent Difference
Cu-64	2.11E+01	8.82E+00	82%
Co-60	3.64E-03	1.17E-03	103%
Co-58	3.03E-04	3.19E-03	-165%
Au-198	2.76E-03	4.83E-05	193%
Sb-122	2.38E-04	1.25E-01	-199%
Sb-124	3.46E-06	2.68E-03	-199%

TABLE XVIII
MCNP ACTIVITY AND EXPERIMENT ACTIVITY COMPARISON FOR VL-2020 (CC04)

Product	MCNP Activity (uCi)	Experiment Activity (uCi)	Percent Difference
Fe-59	6.34E-03	4.18E-04	175%
Mn-54	1.22E-04	3.84E-04	-103%
Cr-51	1.28E-01	9.99E-03	171%
Co-58	5.72E-04	1.63E-03	-96%
Mo-99	3.94E-02	4.08E-02	-3%
Nb-92m	1.06E-05	4.73E-05	-127%
Co-60	2.87E-03	2.31E-04	170%
Sn-117m	1.76E-03	1.58E-05	196%
W-187	1.85E-01	4.46E-02	122%
Ta-182	6.50E-05	8.44E-05	-26%
Na-24	8.63E-03	2.34E-03	115%
As-76	1.01E-01	1.22E-02	157%
Sb-122	8.30E-03	9.62E-04	158%
Sb-124	1.23E-04	2.56E-05	131%
Au-198	3.17E-03	7.39E-05	191%

C.8.b. Deviations Referenced Spectrum

In reconstruction of the spectrum, the spectrum that is being reconstructed should be well known for comparison. The spectra shown in Figure 13 are obtained from the respective laboratory resources and are provided for rough estimates. The data collected from UMass included activation foils such that we can measure the spectrum again to obtain a more accurate measure for comparative purposes.

The gamma spectra and activities from the foils was measured. The foil geometries and masses are well known, provided by the vendor Shield Werx. The foil geometries were encoded into MCNP, as was the input spectra shown in Figure 13. After accounting for all of the efficiency terms, the counts at select gamma lines for each of the foils was obtained from the MCNP simulations and the data, providing in Table XIX. The table provides the foil metal, and the data associated with the gamma lines. The factor of error is the ratio of the data (net area counts) over the simulated counts. The relevant reaction and threshold energy is provided for reference. The interesting observation from the data shows that the counts resulting only from non-zero threshold reactions ($E > 3.2$ MeV) the average factor of error (4.9 ± 1.0) seems larger compared to counts resulting from exothermic reactions (2.4 ± 1.0). This difference suggests that the higher energy counts is slightly higher than expected with an overall larger number of incident neutrons across the full energy range. The SAND-II code was then used to attempt to make a full reconstruction of the incident neutron spectrum from the UMass reactor using the activation foils.

TABLE XIX
COMPARISON OF ACTIVATION FOIL DATA TO MCNP RESULTS

Gamma Energy (keV)	Sim. counts	Net Area counts	Factor of Error	Reaction	Threshold Energy (MeV)
Aluminum					
1368	174	787	4.5	$^{27}\text{Al}(\text{n},\alpha)^{24}\text{Na}$	3.25
2754	80	310	3.9	$^{27}\text{Al}(\text{n},\alpha)^{24}\text{Na}$	3.25
Copper					
511	20,625	45,009	2.2	$^{63}\text{Cu}(\text{n},\gamma)^{64}\text{Cu}$	0
				$^{63}\text{Cu}(\text{n},2\text{n})^{62}\text{Cu}$	11.03
				$^{65}\text{Cu}(\text{n},\text{p})^{65}\text{Ni}$	1.376
				$^{65}\text{Cu}(\text{n},2\text{n})^{64}\text{Cu}$	10.064
Titanium					
983.5	61	353	5.8	$^{48}\text{Ti}(\text{n},\text{p})^{48}\text{Sc}$	3.276
				$^{49}\text{Ti}(\text{n},\text{d})^{48}\text{Sc}$	9.315
				$^{50}\text{Ti}(\text{n},\text{t})^{48}\text{Sc}$	14.087
1037.5	56	316.9	5.7	$^{48}\text{Ti}(\text{n},\text{p})^{48}\text{Sc}$	3.276
				$^{49}\text{Ti}(\text{n},\text{d})^{48}\text{Sc}$	9.315
				$^{50}\text{Ti}(\text{n},\text{t})^{48}\text{Sc}$	14.087
1312	45	237.8	5.2	$^{48}\text{Ti}(\text{n},\text{p})^{48}\text{Sc}$	3.276
				$^{49}\text{Ti}(\text{n},\text{d})^{48}\text{Sc}$	9.315
				$^{50}\text{Ti}(\text{n},\text{t})^{48}\text{Sc}$	14.087
Gold					
411	4,989,759	1,221,169	0.24	$^{197}\text{Au}(\text{n},\gamma)^{198}\text{Au}$	0
675.8	25,254	5,656	0.22	$^{197}\text{Au}(\text{n},\gamma)^{198}\text{Au}$	0
Iron					
834.8	45	191	4.2	$^{54}\text{Fe}(\text{n},\text{p})^{54}\text{Mn}$	0
				$^{56}\text{Fe}(\text{n},\text{t})^{54}\text{Mn}$	12.148
1099	92	67	0.7	$^{58}\text{Fe}(\text{n},\gamma)^{59}\text{Fe}$	0
1291	59	64	1.08	$^{58}\text{Fe}(\text{n},\gamma)^{59}\text{Fe}$	0
Magnesium					
1368.626	12	67	5.6	$^{24}\text{Mg}(\text{n},\text{p})^{24}\text{Na}$	4.933
2754	5	17	3.4	$^{24}\text{Mg}(\text{n},\text{p})^{24}\text{Na}$	4.933
Zirconium					
724.192	315	985	3.1	$^{94}\text{Zr}(\text{n},\gamma)^{95}\text{Zr}$	0
				$^{96}\text{Zr}(\text{n},\text{d})^{95}\text{Zr}$	9.398
				$^{96}\text{Zr}(\text{n},2\text{n})^{95}\text{Zr}$	7.939
743.36	3,049	8,269	2.7	$^{96}\text{Zr}(\text{n},\gamma)^{97}\text{Zr}$	0
756.725	369	1,209	3.3	$^{94}\text{Zr}(\text{n},\gamma)^{95}\text{Zr}$	0
				$^{96}\text{Zr}(\text{n},\text{d})^{95}\text{Zr}$	9.398
				$^{96}\text{Zr}(\text{n},2\text{n})^{95}\text{Zr}$	7.939

Gamma Energy (keV)	Sim. counts	Net Area counts	Factor of Error	Reaction	Threshold Energy (MeV)
Nickel					
511	3,399	9,442	2.8	$^{58}\text{Ni}(n,p)^{58}\text{Co}$ $^{60}\text{Ni}(n,t)^{58}\text{Co}$	0 11.699
810.75	7,065	20,705	2.9	$^{58}\text{Ni}(n,p)^{58}\text{Co}$ $^{60}\text{Ni}(n,t)^{58}\text{Co}$	0 11.699
863.95	46	146	3.2	$^{58}\text{Ni}(n,p)^{58}\text{Co}$ $^{60}\text{Ni}(n,t)^{58}\text{Co}$	0 11.699
1674.7	17	49	2.9	$^{58}\text{Ni}(n,p)^{58}\text{Co}$ $^{60}\text{Ni}(n,t)^{58}\text{Co}$	0 11.699
Indium					
190.27	30,416	112,703	3.7	$^{113}\text{In}(n,\gamma)^{114\text{m}}\text{In}$	0
558.43	2,155	6,098	2.8	$^{113}\text{In}(n,\gamma)^{114\text{m}}\text{In}$	0
725.24	1,649	4,345	2.6	$^{113}\text{In}(n,\gamma)^{114\text{m}}\text{In}$	0
1299.83	39	80	2.1	$^{113}\text{In}(n,\gamma)^{114\text{m}}\text{In}$	0

C.8.c. Input Spectrum Calibration

The activation foils data were utilized to reconstruct the reactor neutron spectrum for comparison to the UMass stated reference spectrum. The reconstructed spectrum was then employed in MCNP with battery models to determine whether the reconstructed spectrum might serve as a better representation of the experimental conditions for further MCNP simulations.

The SAND-II code was used to reconstruct the UMass FNI source neutron spectrum from activation foil results of the first experiment at UMass. Ten (10) foils were exposed and 13 reactions produced radionuclides with significant activities. Initially, all 13 reactions and the measured activities were input into SAND-II along with the source spectrum obtained from UMass as an initial spectrum; however, the code stopped after only 3 iterations with deviations between the measured-to-calculated activities ranging from 15% to 605% as shown in Table XX. SAND-II ceases its iterative solution process once the measured-to-calculated activities become stable (to within less than one percent change per iteration).

TABLE XX
SAND-II OUTPUT FOR 13 REACTIONS AFTER 3 ITERATIONS

Reaction	Saturated Measured Activity (DPS/Nuc.)	Saturated Calculated Activity (DPS/Nuc.)	Nominal 5% Activity Limits (MeV)		Ratio Measured to Calculated Activities	Deviation of Measured from Calculated Activity (%)
			Lower	Upper		
$^{58}\text{Fe}(n,\gamma)^{59}\text{Fe}$	3.900E-19	6.242E-19	2.000E-4	2.700E-1	0.6248	-37.52
$^{58}\text{Ni}(n,p)^{58}\text{Co}$	9.110E-20	3.685E-19	1.800E+0	1.490E+1	0.2472	-75.28
$^{197}\text{Au}(n,g)^{198}\text{Au}$	3.790E-16	8.879E-16	1.500E-4	1.000E-2	0.4269	-57.31
$^{63}\text{Cu}(n,g)^{64}\text{Cu}$	2.470E-16	4.341E-16	5.750E-4	8.400E-3	0.5690	-43.10
$^{54}\text{Fe}(n,p)^{54}\text{Mn}$	1.080E-20	2.573E-19	1.800E+0	1.630E+1	0.0420	-95.80
$^{24}\text{Mg}(n,p)^{24}\text{Na}$	6.800E-20	5.902E-20	8.800E+0	1.720E+1	1.1521	15.21
$^{46}\text{Ti}(n,p)^{46}\text{Sc}$	7.460E-21	9.614E-20	8.400E+0	1.750E+1	0.0776	-92.24
$^{47}\text{Ti}(n,p)^{47}\text{Sc}$	6.150E-19	8.729E-20	1.900E+0	1.610E+1	7.0456	604.56
$^{48}\text{Ti}(n,p)^{48}\text{Sc}$	1.180E-20	2.568E-20	1.000E+1	1.760E+1	0.4595	-54.05
$^{27}\text{Al}(n,\alpha)^{24}\text{Na}$	5.560E-20	3.374E-20	9.100E+0	1.710E+1	1.6480	64.80
$^{113}\text{In}(n,g)^{114}\text{In}$	6.750E-17	1.877E-16	2.400E-5	2.000E-3	0.3596	-64.04
$^{94}\text{Zr}(n,g)^{95}\text{Zr}$	1.460E-19	4.509E-19	2.000E-3	7.600E-2	0.3238	-67.62
$^{96}\text{Zr}(n,g)^{97}\text{Zr}$	1.950E-16	8.148E-15	1.500E-1	1.640E+1	0.0239	-97.61
Standard Deviation of Measured Activities (%)						187.30

In order to reduce the deviation of the activities, the inter-consistency of different foils and reactions was evaluated by eliminating and/or adding one or more reactions to the SAND-II input. After trial and error, a best solution was found using 6 foils and 6 reactions. Those results are shown as Table XXI. The code stopped running after 34 iterations by achieving the goal of deviations in the measured-to-calculated activities of less than 0.01%. The spectrum result was plotted and compared with the data obtained from UMass, shown as Figure 33. The graph shows that the reconstructed flux is typically an order or two smaller than the UMass reference value. The mid energy range reconstructed fluxes might benefit from a curve-smoothing algorithm.

TABLE XXI
SAND-II OUTPUT FOR 6 REACTIONS AFTER 34 ITERATIONS

Reaction	Saturated Measured Activity (DPS/Nuc.)	Saturated Calculated Activity (DPS/Nuc.)	Nominal 5% Activity Limits (MeV)		Ratio Measured to Calculated Activities	Deviation of Measured from Calculated Activity (%)
			Lower	Upper		
$^{58}\text{Fe}(n,\gamma)^{59}\text{Fe}$	3.900E-19	3.900E-19	4.250E-3	1.000E+0	1.0000	0.00
$^{58}\text{Ni}(n,p)^{58}\text{Co}$	9.110E-20	9.110E-19	1.200E+0	1.650E+1	1.0000	0.00
$^{197}\text{Au}(n,g)^{198}\text{Au}$	3.790E-16	3.791E-16	4.000E-4	5.250E-2	0.9999	-0.01
$^{63}\text{Cu}(n,g)^{64}\text{Cu}$	2.470E-16	2.470E-16	5.750E-4	8.400E-3	1.0001	0.01
$^{48}\text{Ti}(n,p)^{48}\text{Sc}$	1.180E-20	1.180E-20	1.080E+1	1.790E+1	1.0000	0.00
$^{94}\text{Zr}(n,g)^{95}\text{Zr}$	1.460E-19	1.460E-19	2.000E-3	7.200E-2	1.0000	0.00
Standard Deviation of Measured Activities (%)						0.01

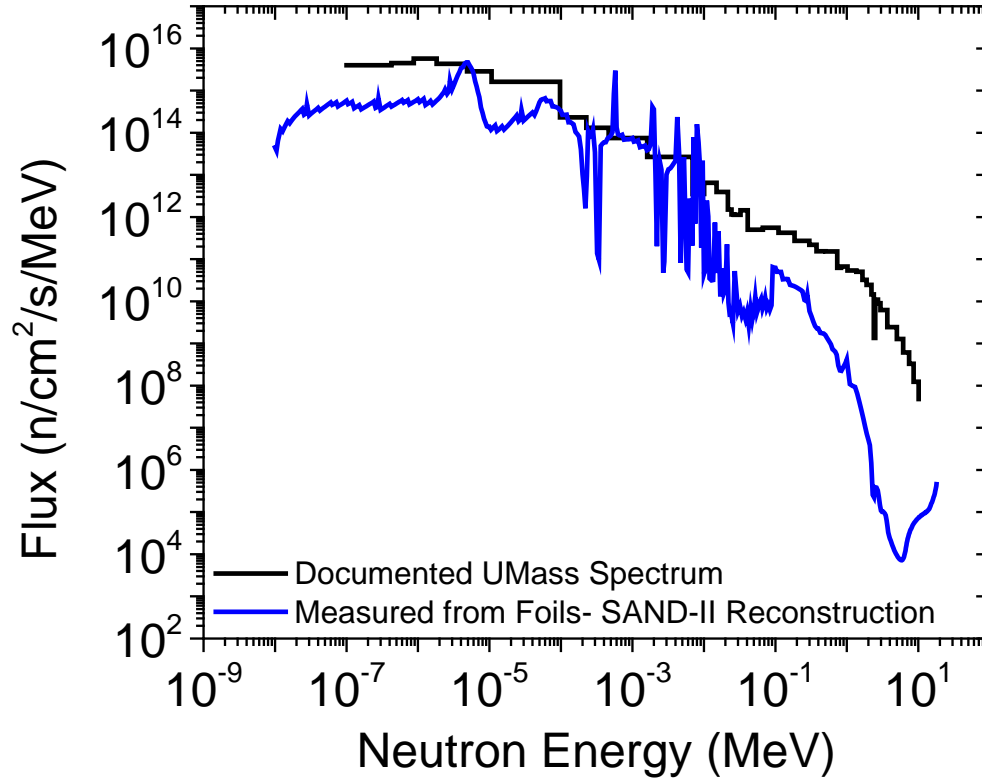


Figure 33: Source neutron spectrum comparison of SAND-II reconstruction and UMass documented spectrum [7].

To reduce the deviation of the activities, the inter-consistency of different foils and reactions was evaluated by eliminating and/or adding one or more reactions to the SAND-II input. After trial and error, a best solution was found using 6 foils and 6 reactions for FNI Run 1. Those results are shown at the top of Table XXII. The solution was achieved after 43 iterations and the deviations in the measured-to-calculated activities are less than 0.02%. The results for FNI Run 2 using the same 6 reactions are also listed in the middle of Table XXII for comparison. After 31 iterations, the difference between measured and calculated activities were less than 0.02% as well. The best solution for the second experiment was achieved with 7 foils and 7 reactions, shown in the bottom of Table XXII. The code stopped running after 421 iterations and the deviations in the measured-to-calculated activities had become stable, within 0.06%.

TABLE XXII
SAND-II RESULTS FOR ACTIVATION FOILS USED IN BOTH EXPERIMENTAL RUNS AT FNI

Experimental Run 1	Measured Activity (Bq/Nucleus)	Calculated Activity (Bq/Nucleus)	Difference (%)
$^{58}\text{Fe}(n,\gamma)^{59}\text{Fe}$	4.480×10^{-19}	4.480×10^{-19}	0.00
$^{58}\text{Ni}(n,p)^{58}\text{Co}$	8.940×10^{-20}	8.940×10^{-20}	0.00
$^{197}\text{Au}(n,\gamma)^{198}\text{Au}$	4.310×10^{-16}	4.311×10^{-16}	-0.02
$^{63}\text{Cu}(n,\gamma)^{64}\text{Cu}$	3.130×10^{-16}	3.130×10^{-16}	0.01
$^{48}\text{Ti}(n,p)^{48}\text{Sc}$	1.360×10^{-20}	1.360×10^{-20}	0.00
$^{94}\text{Zr}(n,\gamma)^{95}\text{Zr}$	1.430×10^{-19}	1.430×10^{-19}	0.00
	43 Iterations	Standard Dev. (%)	0.01
Experimental Run 2	Measured Activity (Bq/Nucleus)	Calculated Activity (Bq/Nucleus)	Difference (%)
$^{58}\text{Fe}(n,\gamma)^{59}\text{Fe}$	5.950×10^{-19}	5.950×10^{-19}	0.00
$^{58}\text{Ni}(n,p)^{58}\text{Co}$	1.320×10^{-19}	1.320×10^{-19}	0.00
$^{197}\text{Au}(n,\gamma)^{198}\text{Au}$	4.020×10^{-16}	4.021×10^{-16}	-0.02
$^{63}\text{Cu}(n,\gamma)^{64}\text{Cu}$	2.490×10^{-16}	2.490×10^{-16}	0.01
$^{48}\text{Ti}(n,p)^{48}\text{Sc}$	1.260×10^{-20}	1.260×10^{-20}	0.00
$^{94}\text{Zr}(n,\gamma)^{95}\text{Zr}$	2.020×10^{-19}	2.020×10^{-19}	0.00
	31 Iterations	Standard Dev. (%)	0.01
Experimental Run 2	Measured Activity (Bq/Nucleus)	Calculated Activity (Bq/Nucleus)	Difference (%)
$^{58}\text{Fe}(n,\gamma)^{59}\text{Fe}$	5.950×10^{-19}	5.950×10^{-19}	0.00
$^{58}\text{Ni}(n,p)^{58}\text{Co}$	1.320×10^{-19}	1.319×10^{-19}	0.04
$^{197}\text{Au}(n,\gamma)^{198}\text{Au}$	4.020×10^{-16}	4.020×10^{-16}	0.00
$^{63}\text{Cu}(n,\gamma)^{64}\text{Cu}$	2.490×10^{-16}	2.490×10^{-16}	0.00
$^{54}\text{Fe}(n,p)^{54}\text{Mn}$	2.760×10^{-20}	2.762×10^{-20}	-0.06
$^{46}\text{Ti}(n,p)^{46}\text{Sc}$	9.520×10^{-21}	9.518×10^{-21}	0.02
$^{94}\text{Zr}(n,\gamma)^{95}\text{Zr}$	2.020×10^{-19}	2.020×10^{-19}	0.00
	421 Iterations	Standard Dev. (%)	0.03

The spectrum generated from the SAND-II code was placed into 81 bins and is shown in Figure 34. The reconstructed spectra for experiments 1 and 2 using the same 6 reactions are close in shape, except that the flux level for experiment 1 is slightly lower than the second experiment. The reconstructed spectra for experiment 2 using the two different reaction sets agree with each other in both shape and flux level until around 1 MeV. This shows the impact that different foil reactions in the input has on the spectral reconstruction. An average of the logarithms of spectra were calculated and then the average was taken to the power of 10, providing the average spectrum shown in Figure 34.

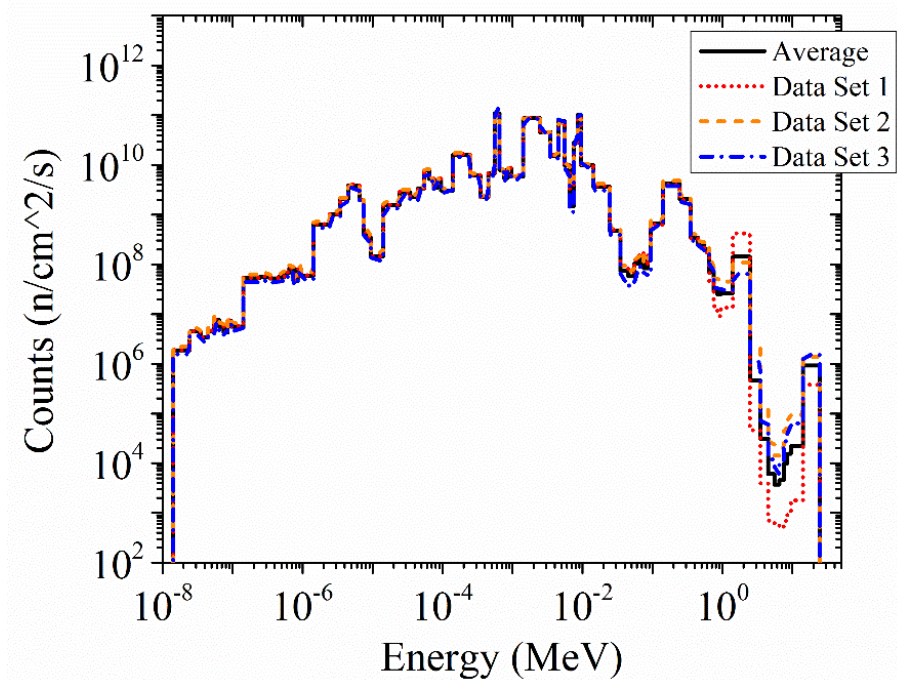


Figure 34: The reconstructed spectra from three data sets. Data set 1 is associated with 6 reactions from the first experiment. Data set 2 is the same 6 reactions for the second experiment, while data set 3 is from 7 reactions from the second experiment.

C.8.d. SAND-II Reconstructed Spectrum

As mentioned, a limited number of reactions was employed in the neutron spectrum reconstruction using the batteries. The results of the SAND-II code are given in Table XXIII, showing the four reactions over the two batteries used. Each of the batteries generated a separate neutron spectrum, which is shown in Figure 35. The spectra are averaged in the same way the activation foil spectra were averaged.

TABLE XXIII
SAND-II RESULTS FOR THE FITTING OF THE RADIOISOTOPES FROM THE BATTERIES

Small Profile (Cell02)	Measured Activity (Bq/Nucleus)	Calculated Activity (Bq/Nucleus)	Difference (%)
$^{58}\text{Ni}(n,p)^{58}\text{Co}$	1.290×10^{-19}	1.290×10^{-19}	0.00
$^{197}\text{Au}(n,\gamma)^{198}\text{Au}$	4.470×10^{-16}	4.470×10^{-16}	-0.01
$^{63}\text{Cu}(n,\gamma)^{64}\text{Cu}$	2.140×10^{-16}	2.140×10^{-16}	0.01
	24 Iterations	Standard Dev. (%)	0.01
ML2020 (CC03)	Measured Activity (Bq/Nucleus)	Calculated Activity (Bq/Nucleus)	Difference (%)
$^{58}\text{Ni}(n,p)^{58}\text{Co}$	9.530×10^{-20}	9.529×10^{-20}	0.01
$^{197}\text{Au}(n,\gamma)^{198}\text{Au}$	1.720×10^{-15}	1.720×10^{-15}	0.00
$^{54}\text{Fe}(n,p)^{54}\text{Mn}$	1.670×10^{-20}	1.670×10^{-20}	-0.01
	175 Iterations	Standard Dev. (%)	0.01

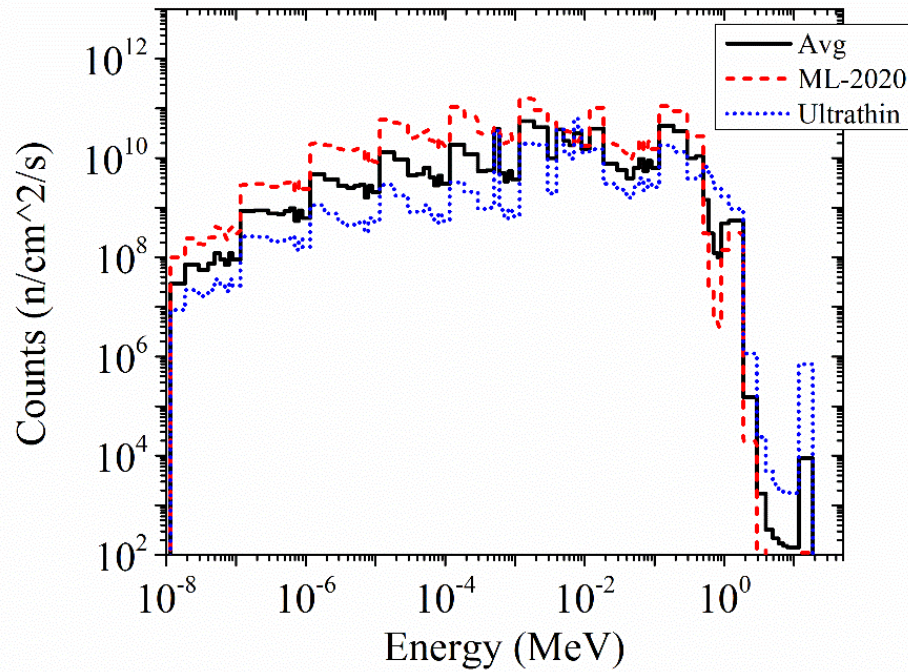


Figure 35: The spectra generated from the SAND-II code using battery activities. The solid line is the average from the two battery spectra.

The activation foil spectrum is compared to the battery spectrum in Figure 36. The spectra are in good agreement to within a factor of ten. The error bars shown in Figure 36 are the minimum and maximum values used in the average for each energy bin. From [6], the differences in the expected neutron flux from 10 keV up to 1 MeV is more than an order of magnitude. With this limited data set, the neutron spectrum can be readily obtained from only a couple batteries.

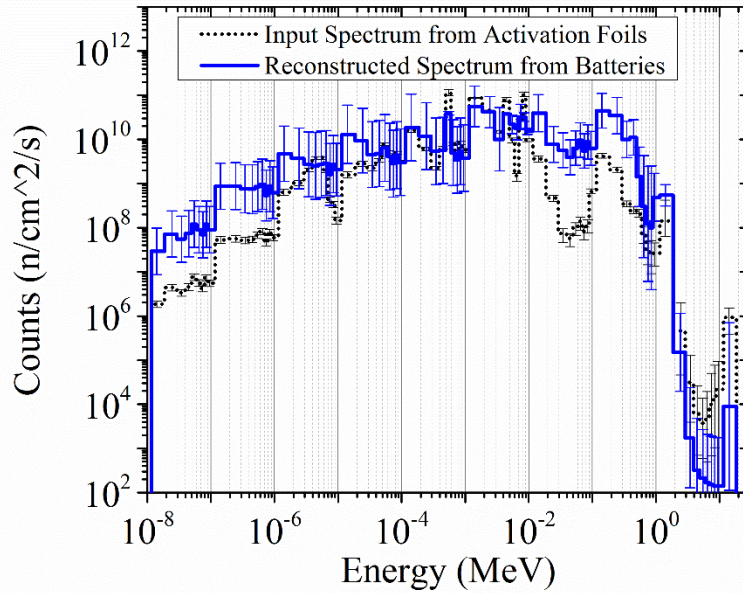


Figure 36: The average activation foil spectrum (dotted line) from Figure 34 compared to the battery spectrum (solid line) from Figure 35. The error bars are the maximum and minimum values used in calculating the averages.

There are deviations from the activation foil spectrum associated with separate energy regions. A part of the difference is due to the limited number of reactions used in the spectrum reconstruction done with the batteries. The cross sections for the four reactions is shown in Figure 37. In the initial region, the reconstructed spectrum is high from 10^{-8} MeV to 10^{-4} MeV, where ^{198}Au and ^{64}Cu reactions are utilized. From 10^{-4} MeV to 10^{-2} MeV, the cross sections for these two reactions have multiple resonances and on average have a fairly similar cross section, and the output spectrum is consistent with the one measured using the foils. The SAND-II code would have to weigh activities from these radioisotopes more similarly. From 10^{-2} MeV to 1 MeV, we return to a state where the ^{198}Au reaction cross section is higher, and the output spectrum is high. Above 1 MeV, all four reactions are considered, and the output spectrum is low. This suggests a systematic effect from the fit, and it is believed that more input data will correct these errors.

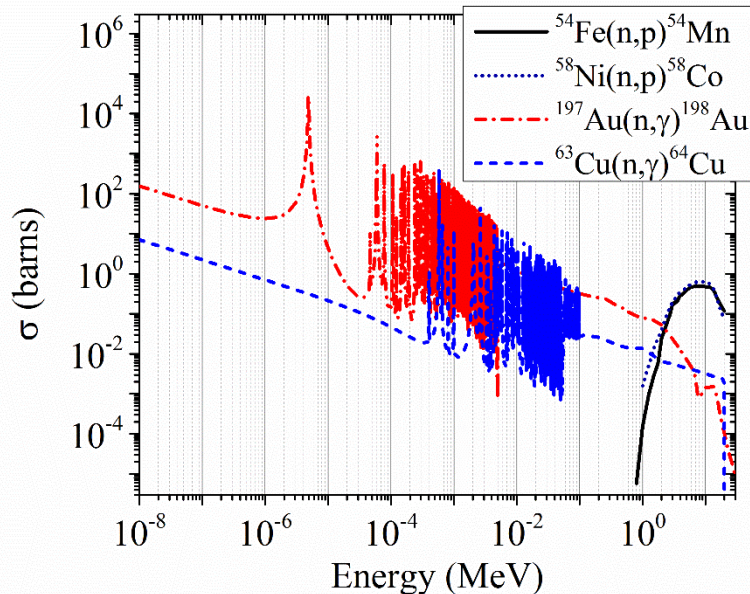


Figure 37: Plot of the cross sections for the four reactions used in the battery neutron spectrum reconstruction. The proton emission reactions have threshold values just below 1 MeV, where the radiative capture reactions are exothermic.

D. Key Outcomes

The research program has developed means to use a lithium battery for nuclear forensics. The key about batteries is that they are layers of materials assembled in a sealed package and are distributed in mass. As the batteries are manufactured from large sheets of material, i.e. cut from the same cloth, the batteries are expected to be similar in isotopic content particularly from a specified production lot. It is likely that batteries on a given shelf at a given store will have similar isotopic content. As we deviate further from these ideal conditions, one will expect a gradual difference. As an example, batteries made from the same manufacture obtained in the same town but from a different store may be similar, but from different parts of the country, one might expect very slight differences. When comparing a similar battery from company to company, these differences will be greater. Careful consideration of selection of batteries will improve results.

The initial goal of the program was to look at the battery and its basic composition and to determine how it can be used for nuclear forensics. The general concept of using it for an activation analysis was initially proposed and used as the basis for the study. One key component of the lithium battery is the tritium production from $^6\text{Li}(n,\alpha)\text{t}$ reactions, which have a fairly large cross section for thermal neutrons. The major drawback to tritium is that the radioactive decay (low energy β^- particles) is typically measured using liquid scintillator, where the tritium is directly mixed with the liquid scintillator. The β^- particles cannot escape the battery, requiring the destruction

of the battery such that the internal components can be submersed into a liquid scintillator. We have developed the basic framework to extract the tritium information.

The next part for demonstrating how the battery can be used for nuclear forensics is to look at measuring constituent concentrations either through mass spectrometry or gamma spectrometry. It was determined that a mass spectroscopy measurement is not practical. The detection limits are not robustly sensitive and grinding up radioactive materials (the exposed battery) and placing these radioactive materials into a mass spectrometer is not ideal. A faster and far more sensitive method is to use gamma spectroscopy, which can be used to correlate an incident neutron spectrum to radioisotope activities. A simple model was used to demonstrate that this process is viable by reconstructing an incident neutron spectrum and was explored in more detail.

To empirically demonstrate the forensic methods, data were collected on the batteries. One of the first steps is to complete a full breakdown of all the elements within the battery. Product datasheets are not sufficiently detailed for this analysis, where we are attempting to understand how these methods are flawed, requiring a detailed understanding of the battery inputs. The batteries were disassembled, broken down and some of the parts were placed in a mass spectrometer. The constituents of some of the other parts of the batteries were estimated based on the datasheets. A significantly more accurate measure of the battery constituents was obtained to be placed into MCNP models for comparative purposes. Of the batteries that were analyzed with the mass spectrometer, they were placed into high neutron flux fields to simulate conditions associated with nuclear weapons. Four exposures were made on a variety of batteries at two different facilities (FNI at UMass and TRIGA at OSU), where the neutron spectrum is unique for each of the facilities. The FNI facility at UMass allows for a large exposure area with a uniform flux, where activation foils were also placed. Gamma spectroscopy was conducted on all of the batteries and activation foils.

One of the initial observations was the ratio of ^{24}Na to ^{58}Co in 18650 batteries. The data were a comparison between the neutron spectra from the TRIGA reactor compared to the FNI environment, where the FNI neutron spectrum is harder. The analysis used two similar 18650 batteries, yet the battery manufacturers were different. There is a reasonable assumption that the relative abundance of nickel to aluminum in the batteries were fairly consistent for each battery, and that the aluminum and nickel concentrates dominate the production of the ^{24}Na and ^{58}Co , aside from any trace elements in the batteries. Given these assumptions, the ratio of ^{24}Na to ^{58}Co in the batteries exposed to the FNI harder spectrum compared to the batteries exposed at TRIGA is larger. This is a direct correlation expected with a spectrum with a large fraction of neutrons with higher energies.

A study on the specific radioisotopes ^{56}Mn formed in the batteries was done in significantly more detail. The study consisted of a MCNP simulation associated with estimated neutron spectra from different weapons types, such as those from Fat Boy and Little Man. The calculated emission spectra for these weapons are given in Figure 38 for reference. The MCNP model used the mass spectrometry results and a detailed battery model consisting of varying parts of different constituents. The results of the data and the simulations show reasonable agreement with the ^{56}Mn being one of the largest signals. The study shows that this signal can provide incident neutron spectral information by measuring the ^{56}Mn activity as a function of distance from the detonation site. This effect is because the Little Boy weapon has a harder output spectrum compared to Fat Man due to the large mass of explosives used to “implode” the nuclear material within the Fat Man weapon. Due to this different initial moderation, the attenuation in air from the different initial spectra results in different activities ^{56}Mn that are produced from $^{55}\text{Mn}(n,\gamma)$ reactions.

The analysis of the lithium batteries for nuclear forensics shows that the lithium battery can be used to reconstruct the incident neutron spectrum. This particular analysis only required four reactions from two batteries to reconstruct the spectrum to within a factor of ten when compared to the spectrum generated from a more standard method using activation foils. The accuracy of this analysis is sufficient for nuclear forensics, yet it is understood that this spectrum can be significantly more accurate given a larger input data set. From Figure 38, there is a one to two order of magnitude difference from approximately 1 keV to 1 MeV due to the implosion device in Fat Man. It is understood that this is only an approximation, and this spectrum will soften as it is attenuated in the environment. One does expect these differences to have traceable history for a reasonable

distance from the detonation site, allowing the batteries to maintain their relevancy. Furthermore, the analysis presented here is limited, and it is expected that results will systematically improve with a larger dataset.

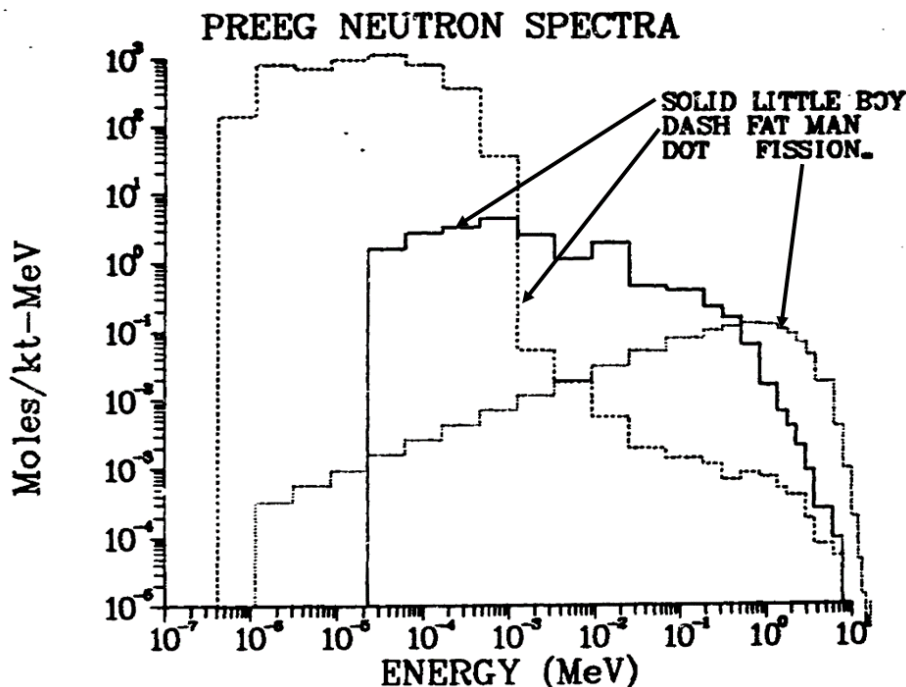


Figure 38: Plot of the calculated energy spectra from [6], which are originally obtained from Dr. W.E. Preeg from Los Alamos Laboratories. The data are results from 1D spherical calculations.

The advantageous nature of a battery is that it is mass produced and ubiquitous within all environments. The cell phone and other portable electronics are not only pervasive within developed countries, these devices can be found in all countries across the globe. For this analysis, we consider the special case of thin, lithium batteries to provide the spectrum. The majority of future analysis could be the development of a database of battery constituents for nuclear forensic purposes. These would include all battery types, and updated when new technology enters the market.

The spectral information from batteries provides a piece of information for a complete forensic analysis, where the battery can be considered a point source for this information. This is extremely useful in this context as the battery environment will significantly change the incident neutron spectrum. When few variables are needed to reconstruct the incident spectrum, the confidence level regarding a nuclear forensic analysis improves. This analysis on a few lithium batteries proves that a battery can provide this one key component, where spectral data can be obtained over a large geographical area.

E. References

- [1] S. Glasstone and P. Dolan, *The Effects of Nuclear Weapons*, 3rd ed. Washington, D.C.: US DoD and Energy Res. and Dev. Administration, 1977.
- [2] M. B. Chadwick, M. Herman, P. Oblozinsky, *et al.*, "ENDF/B-VII.1 Nuclear Data for Science and Technology: Cross Sections, Covariances, Fission Product Yields and Decay Data," *Nuclear Data Sheets: Special Issue on ENDF/B-VII.1 Library* (<http://www.nndc.bnl.gov/>), vol. 112, pp. 2887-2996, 2011.
- [3] T. B. Coplen, J. K. Bohlke, P. De Bièvre, *et al.*, "Isotope Abundance Variations of Selected Elements: (IUPAC Technical Report)," *Pure and Applied Chemistry*, vol. 74, pp. 1987-2017, 2002.

- [4] "MCNP – A General Monte Carlo N-Particle Transport Code, Version 5, Los Alamos National Laboratory," ed.
- [5] G. M. Hieftje, J.-M. Mermet, S. J. Hill, *et al.*, "Various Chapters," in *Inductively Coupled Plasma Spectrometry and its Applications*, S. J. Hill, Ed., 2nd ed Oxford: Blackwell Publishing, 2007.
- [6] P. P. Whalen, "Source terms for the initial radiations," US/Japan joint workshop on the reassessment of A-bomb radiation dosimetry in Hiroshima and Nagasaki, Nagasaki, Japan, Conference Report LA-UR-83-198, Feb 16 1983 1983.
- [7] J. R. White, A. Jirapongmed, L. Bobek, *et al.*, "Design and Initial Testing of an Ex-Core Fast Neutron Irradiator for the UMass-Lowell Research Reactor," presented at the Radiation Protection and Shielding Topical Conference, Sante Fe, NM, 2002.
- [8] H. L. Brode, "Review of Nuclear Weapons Effects," *Annual Review of Nuclear Science*, vol. 18, pp. 153-202, 1968.
- [9] R. Schickler, "Comparison of HEU and LEU neutron spectra in irradiation facilities at the Oregon State TRIGA® reactor," Master of Science, Nuclear Engineering, Oregon State University, Oregon, 2013.

F. Appendix:

TABLE XXIV
COMMON MATERIALS USED IN LITHIUM BATTERIES

Material	Use	Thickness (μm)
Aluminum	Electrode Tab	80 – 150
Aluminum	Cathode Collector	15 – 20
LiCoO_2	Cathode	~100
LiNiO_2	Cathode	~100
$\text{LiNi}_{0.8}\text{Co}_{0.2}\text{O}_2$	Cathode	~100
$\text{LiNi}_{0.8}\text{Co}_{0.15}\text{Al}_{0.05}\text{O}_2$	Cathode	~100
$\text{LiMn}_{0.5}\text{Ni}_{0.5}\text{O}_2$	Cathode	~100
$\text{LiMn}_{0.33}\text{Ni}_{0.33}\text{Co}_{0.33}\text{O}_2$	Cathode	~100
$\text{LiMn}_{0.4}\text{Ni}_{0.4}\text{Co}_{0.2}\text{O}_2$	Cathode	~100
LiMn_2O_4	Cathode	~100
LiFePO_4	Cathode	~100
Polypropylene $(\text{C}_3\text{H}_6)_n$	Separator	12 – 100's
Polyethylene $(\text{C}_2\text{H}_4)_n$	Separator	12 – 100's
Graphite (C_6)	Anode	~100
Hard Carbon (C_6)	Anode	~100
$\text{Li}_4\text{Ti}_5\text{O}_{12}$	Anode	~100
Si $(\text{Li}_{4.4}\text{Si})$	Anode	~100
Ge $(\text{Li}_{4.4}\text{Ge})$	Anode	~100
Copper	Anode Collector	15 – 20
Nickel	Electrode Tab	80 – 150
LiPF_6	Electrolyte solute	N/A
LiBF_4	Electrolyte solute	N/A
Ethylene carbonate $(\text{C}_3\text{H}_4\text{O}_3)$	Electrolyte solvent	N/A
Dimethyl carbonate $(\text{CH}_3\text{O})_2\text{CO}$	Electrolyte solvent	N/A
Diethyl carbonate $(\text{C}_2\text{H}_5\text{O})_2\text{CO}$	Electrolyte solvent	N/A
Ethyl methyl carbonate $(\text{C}_4\text{H}_8\text{O}_3)$	Electrolyte solvent	N/A
Dimethyl methylphosphonate, DMMP $(\text{CH}_3\text{P}(\text{O})(\text{OCH}_3)_2)$	Flame Retardant	N/A
Polyvinylidene Flouride $(\text{C}_2\text{H}_2\text{F}_2)_n$	Resin	N/A
Styrene-Butadiene Rubber $((\text{C}_8\text{H}_8)_m(\text{C}_4\text{H}_6)_n)_x$	Binder	N/A
Sodium carboxymethyl cellulose $(\text{C}_{28}\text{H}_{30}\text{Na}_8\text{O}_{27})$	Binder	N/A

TABLE XXV
RADIOACTIVE ISOTOPES WITHIN EXPOSED LITHIUM BATTERIES

Isotope	Half-life	Threshold (MeV)	Reaction
²⁸ Mg	20.9 h	16.8	³⁰ Si (n, ³ He) ²⁸ Mg
^{44m} Sc	58.6 h	13.8	⁴⁶ Ti (n,t) ^{44m} Sc
²⁶ Al	7.2e5 y	13.5	²⁷ Al (n,2n) ²⁶ Al
²⁶ Al	7.2e5 y	16.7	²⁸ Si (n,t) ²⁶ Al
²² Na	2.6 y	13.0	²³ Na (n,2n) ²² Na
⁵² Mn	5.591 d	12.7	⁵⁴ Fe (n,t) ⁵² Mn
⁵² Mn	5.591 d	13.0	⁵⁴ Fe (n,t) ^{52m} Mn (1)
⁵⁷ Ni	35.6 h	12.4	⁵⁸ Ni (n,2n) ⁵⁷ Ni
⁶⁰ Fe	2.6e6 y	12.4	⁶² Ni (n, ³ He) ⁶⁰ Fe
⁷² Zn	46.5 h	12.3	⁷⁴ Ge (n, ³ He) ⁷² Zn
⁶⁹ Ge	39.1 h	11.7	⁷⁰ Ge (n,2n) ⁶⁹ Ge
⁵⁶ Co	77.2 d	11.3	⁵⁸ Ni (n,t) ⁵⁶ Co
⁵³ Mn	3.74e6 y	6.8	⁵⁴ Fe (n,d) ⁵³ Mn
⁵³ Mn	3.74e6 y	13.6	⁵⁴ Fe (n,2n) ⁵³ Fe (2)
⁵³ Mn	3.74e6 y	16.7	⁵⁴ Fe (n,2n) ^{53m} Fe (3)
⁵⁷ Co	271.7 d	6.1	⁵⁸ Ni (n,d) ⁵⁷ Co
⁵⁷ Co	271.7 d	12.4	⁵⁸ Ni (n,2n) ⁵⁷ Ni (4)
⁴⁷ Ca	4.5 d	3.5	⁵⁰ Ti (n,α) ⁴⁷ Ca
⁴⁷ Ca	4.5 d	13.3	⁴⁹ Ti (n, ³ He) ⁴⁷ Ca
⁴⁸ Sc	43.7 h	3.3	⁴⁸ Ti (n,p) ⁴⁸ Sc
⁴⁸ Sc	43.7 h	9.3	⁴⁹ Ti (n,d) ⁴⁸ Sc
⁴⁸ Sc	43.7 h	14.1	⁵⁰ Ti (n,t) ⁴⁸ Sc
⁷² Ga	14.1 h	3.3	⁷² Ge (n,p) ⁷² Ga
⁷² Ga	14.1 h	7.9	⁷³ Ge (n,d) ⁷² Ga
⁷² Ga	14.1 h	11.9	⁷⁴ Ge (n,t) ⁷² Ga
⁷² Ga	14.1 h	12.3	⁷⁴ Ge (n, ³ He) ⁷² Zn (5)
⁴⁵ Ca	162.6 d	2.1	⁴⁸ Ti (n, α) ⁴⁵ Ca
⁴⁵ Ca	162.6 d	11.2	⁴⁷ Ti (n, ³ He) ⁴⁵ Ca
⁴⁶ Sc	83.8 d	1.6	⁴⁶ Ti (n,p) ⁴⁶ Sc
⁴⁶ Sc	83.8 d	8.4	⁴⁷ Ti (n,d) ⁴⁶ Sc
⁴⁶ Sc	83.8 d	13.9	⁴⁸ Ti (n,t) ⁴⁶ Sc
³ H	12.3 y	Min. 0	All (n,t) Reactions (6)
⁵⁹ Fe	44.5 d	0	⁵⁸ Fe (n,γ) ⁵⁹ Fe
⁵⁹ Fe	44.5 d	0.4	⁶² Ni (n, α) ⁵⁹ Fe
⁵⁹ Fe	44.5 d	0.8	⁵⁹ Co (n,p) ⁵⁹ Fe
⁵⁹ Fe	44.5 d	10.6	⁶¹ Ni (n, ³ He) ⁵⁹ Fe
⁷¹ Ge	11.4 d	0	⁷⁰ Ge (n,γ) ⁷¹ Ge
⁷¹ Ge	11.4 d	10.9	⁷² Ge (n,2n) ⁷¹ Ge
^{69m} Zn	13.8 h	0	⁷² Ge (n, α) ^{69m} Zn (7)
⁶⁴ Cu	12.7 h	0	⁶³ Cu (n,γ) ⁶⁴ Cu
⁶⁴ Cu	12.7 h	10.1	⁶⁵ Cu (n,2n) ⁶⁴ Cu
⁶³ Ni	101.2 y	0	⁶² Ni (n,γ) ⁶³ Ni
⁶³ Ni	101.2 y	0	⁶³ Cu (n,p) ⁶³ Ni
⁶³ Ni	101.2 y	8.8	⁶⁵ Cu (n,t) ⁶³ Ni
⁶³ Ni	101.2 y	9.8	⁶⁴ Ni (n,2n) ⁶³ Ni
⁶³ Ni	101.2 y	10.5	⁶⁴ Ni (n,d) ⁶³ Co (8)
⁶³ Ni	101.2 y	12.5	⁶⁵ Cu (n, ³ He) ⁶³ Co (8)

^{59}Ni	7.6e4 y	0	$^{58}\text{Ni} (n,\gamma) ^{59}\text{Ni}$
^{59}Ni	7.6e4 y	11.6	$^{60}\text{Ni} (n,2n) ^{59}\text{Ni}$
^{60}Co	1925.3 d	0	$^{59}\text{Co} (n,\gamma) ^{60}\text{Co} (9)$
^{60}Co	1925.3 d	2.1	$^{60}\text{Ni} (n,p) ^{60}\text{Co} (9)$
^{60}Co	1925.3 d	7.8	$^{61}\text{Ni} (n,d) ^{60}\text{Co} (9)$
^{60}Co	1925.3 d	12.2	$^{62}\text{Ni} (n,t) ^{60}\text{Co} (9)$
^{60}Co	1925.3 d	12.4	$^{62}\text{Ni} (n,^3\text{He}) ^{60}\text{Fe} (10)$
^{58}Co	70.8 d	0	$^{58}\text{Ni} (n,p) ^{58}\text{Co}$
^{58}Co	70.8 d	10.6	$^{59}\text{Co} (n,2n) ^{58}\text{Co}$
^{58}Co	70.8 d	11.7	$^{60}\text{Ni} (n,t) ^{58}\text{Co}$
^{55}Fe	2.7 y	0	$^{58}\text{Ni} (n, \alpha) ^{55}\text{Fe}$
^{55}Fe	2.7 y	0	$^{54}\text{Fe} (n,\gamma) ^{55}\text{Fe}$
^{55}Fe	2.7 y	11.4	$^{56}\text{Fe} (n,2n) ^{55}\text{Fe}$
^{47}Sc	3.3 d	0	$^{47}\text{Ti} (n,p) ^{47}\text{Sc}$
^{47}Sc	3.3 d	3.5	$^{50}\text{Ti} (n, \alpha) ^{47}\text{Sc}$
^{47}Sc	3.3 d	9.4	$^{48}\text{Ti} (n,d) ^{47}\text{Sc}$
^{47}Sc	3.3 d	11.3	$^{49}\text{Ti} (n,t) ^{47}\text{Sc}$
^{47}Sc	3.3 d	13.3	$^{49}\text{Ti} (n,^3\text{He}) ^{47}\text{Ca} (11)$
^{32}P	14.3 d	0	$^{31}\text{P} (n,\gamma) ^{32}\text{P}$
^{24}Na	15.0 h	0	$^{23}\text{Na} (n,\gamma) ^{24}\text{Na}$
^{24}Na	15.0 h	3.3	$^{27}\text{Al} (n,\alpha) ^{24}\text{Na}$
^{14}C	5700 y	0	$^{13}\text{C} (n,\gamma) ^{14}\text{C}$
^{14}C	5700 y	0	$^{17}\text{O} (n, \alpha) ^{14}\text{C}$
^{14}C	5700 y	11.1	$^{16}\text{O} (n,^3\text{He}) ^{14}\text{C}$
^{14}C	5700 y	13.8	$^{18}\text{O} (n,p) ^{18}\text{N} (12)$
^{77}As	38.8 h	0	$^{76}\text{Ge} (n,\gamma) ^{77}\text{Ge} (13)$
^{77}As	38.8 h	0	$^{76}\text{Ge} (n,\gamma) ^{77\text{m}}\text{Ge} (14)$
^{54}Mn	312.1 d	0	$^{54}\text{Fe} (n,p) ^{54}\text{Mn}$
^{54}Mn	312.1 d	10.4	$^{55}\text{Mn} (n,2n) ^{54}\text{Mn}$
^{54}Mn	312.1 d	12.1	$^{56}\text{Fe} (n,t) ^{54}\text{Mn}$
^{10}Be	1.4e6 y	0	$^{10}\text{B} (n,p) ^{10}\text{Be}$
^{10}Be	1.4e6 y	4.1	$^{13}\text{C} (n, \alpha) ^{10}\text{Be}$
^{10}Be	1.4e6 y	9.8	$^{11}\text{B} (n,d) ^{10}\text{Be}$
^{10}Be	1.4e6 y	21.1	$^{12}\text{C} (n,^3\text{He}) ^{10}\text{Be}$
^{51}Cr	27.7 d	0	$^{54}\text{Fe} (n, \alpha) ^{51}\text{Cr}$

- $^{52\text{m}}\text{Mn}$ has a half-life of 21 m, and decays to ^{52}Mn (branching ratio, BR = 1.75%) and to ^{52}Cr (BR = 98.25%).
- ^{53}Fe decays to ^{53}Mn (BR = 100%) with a half-life of 8.51 m.
- $^{53\text{m}}\text{Fe}$ decays to ^{53}Fe (BR = 100%) with a half-life of 2.54 m.
- ^{57}Ni decays to ^{57}Co (BR = 100%) with a half-life of 35.6 h.
- ^{72}Zn decays to ^{72}Ga (BR = 100%) with a half-life of 46.5 h.
- Not all of the (n,t) reactions are exothermic.
- $^{69\text{m}}\text{Zn}$ decays to ^{69}Zn (BR = 99.97%) with a half-life of 56.4 m.
- ^{63}Co decays to ^{63}Ni (BR = 100%) with a half-life 27.4 s.
- These reactions may also produce $^{60\text{m}}\text{Co}$ with no significant difference in the Q value, which decays to ^{60}Co (BR = 99.776%) with a half-life 10.467 m.
- ^{60}Fe decays to ^{60}Co (BR = 100%) with a half-life of 2.26e6 y. Notice that this reaction is repeated, since it will produce two long lived isotopes.
- ^{47}Ca decays to ^{47}Sc (BR = 100%) with a half-life of 4.536 d.
- ^{18}N decays to ^{14}C (BR = 12.2%) with a half-life of 0.62 s.
- ^{77}Ge decays to ^{77}As (BR = 100%) with a half-life of 11.3 h.
- $^{77\text{m}}\text{Ge}$ decays to ^{77}As (BR = 81%) with a half-life of 52.9 s, or decays to ^{77}Ge (BR = 19%).

TABLE XXVI

FRACTION OF ELEMENTAL COMPOSITION WITH RESPECT TO THE TOTAL NUMBER OF ATOMS WITHIN LITHIUM BATTERIES

Sym	LIR2032 (CC01)	CR2032 (CC02)	18650 (18650A)	RCR123A (RCR01)	AA LiFeS (AA01)	RCR123A (RCR02)	18650 (18650B)	AA LiSOCl (AA02)	ML2020 (CC03)	VL2020 (CC04)	Cell Phn. (Cell01)	Small-Pro (Cell02)	ED Batt (Cell03)	Elec. Dev. (Cell04)
Fe	3.27E-01	3.01E-01	1.41E-01	3.12E-01	1.56E-01	7.39E-01	2.01E-04	1.30E-01	4.43E-01	4.21E-01	1.13E-02	2.54E-03	9.98E-03	2.06E-01
O	1.10E-01	2.14E-01	1.28E-01	1.02E-01	1.32E-01	7.75E-03	2.15E-01	5.43E-01	1.35E-01	1.37E-01	6.80E-02	0.00E+00	3.35E-01	4.46E-02
Al	3.98E-02	4.31E-04	8.63E-02	8.49E-02	8.71E-03	7.10E-02	1.12E-01	5.52E-02	6.38E-02	6.74E-02	6.70E-01	2.00E-03	2.49E-01	5.41E-01
Cu	4.75E-02	3.92E-05	1.55E-01	1.31E-01	5.77E-03	1.39E-01	3.05E-03	4.11E-04	1.04E-03	8.09E-04	6.08E-03	6.13E-01	1.01E-01	5.94E-02
C	8.70E-02	2.87E-01	1.05E-01	1.46E-01	2.70E-02	1.55E-02	9.64E-02	0.00E+00	7.21E-02	1.50E-01	1.32E-01	0.00E+00	1.08E-01	1.43E-02
Li	1.25E-01	5.42E-02	1.83E-01	9.90E-02	2.49E-01	5.79E-04	1.11E-06	2.56E-02	1.39E-02	4.34E-03	2.04E-04	6.66E-02	2.67E-04	9.60E-05
Ni	4.19E-02	5.39E-03	1.12E-01	9.79E-03	1.91E-02	1.66E-02	1.99E-02	4.55E-02	2.78E-02	2.63E-02	1.08E-02	2.89E-01	4.10E-02	3.63E-02
Cr	1.12E-01	2.89E-02	1.24E-04	1.70E-04	3.49E-02	3.03E-04	8.26E-05	3.50E-02	1.13E-01	1.07E-01	2.17E-05	2.33E-04	2.36E-03	5.11E-02
H	0.00E+00	0.00E+00	0.00E+00	0.00E+00	3.22E-01	0.00E+00	1.01E-01	0.00E+00	0.00E+00	0.00E+00	0.00E+00	0.00E+00	0.00E+00	0.00E+00
Ga	0.00E+00	0.00E+00	0.00E+00	0.00E+00	4.70E-06	8.66E-06	3.74E-01	4.87E-06	1.37E-05	1.30E-05	2.75E-05	3.89E-07	6.48E-06	3.59E-05
Co	5.82E-02	3.13E-05	3.75E-02	6.06E-06	3.75E-04	5.95E-03	3.27E-02	3.83E-04	5.22E-04	6.11E-04	5.21E-02	1.39E-02	1.02E-01	1.43E-02
Mn	4.41E-03	1.08E-01	4.79E-02	3.67E-04	2.03E-03	1.42E-03	1.82E-04	2.05E-03	5.54E-02	3.60E-03	3.30E-03	8.47E-03	1.98E-04	3.49E-03
F	0.00E+00	0.00E+00	0.00E+00	0.00E+00	0.00E+00	6.83E-04	2.47E-02	0.00E+00	6.84E-02	5.08E-02	4.11E-02	0.00E+00	4.69E-02	6.24E-03
P	4.32E-02	0.00E+00	3.66E-03	1.09E-01	8.50E-05	4.85E-04	1.99E-03	2.91E-04	3.50E-04	2.86E-04	3.13E-04	2.01E-03	1.97E-03	1.46E-03
Cl	0.00E+00	0.00E+00	0.00E+00	0.00E+00	0.00E+00	0.00E+00	0.00E+00	1.56E-01	1.53E-04	0.00E+00	0.00E+00	0.00E+00	0.00E+00	0.00E+00
S	0.00E+00	0.00E+00	0.00E+00	0.00E+00	4.22E-02	3.91E-06	2.97E-04	3.48E-03	2.25E-04	4.94E-05	0.00E+00	0.00E+00	2.24E-04	2.99E-05
V	5.00E-04	5.82E-05	6.31E-06	7.54E-06	1.61E-04	4.27E-06	2.99E-05	1.63E-04	4.16E-04	2.69E-02	3.15E-05	1.97E-06	1.38E-05	2.43E-04
Mg	1.60E-05	1.35E-05	0.00E+00	4.66E-03	7.05E-06	7.01E-05	2.44E-04	1.58E-05	3.70E-06	6.81E-06	4.61E-03	1.14E-04	7.43E-05	3.62E-03
Dy	6.79E-08	5.38E-09	1.89E-08	2.15E-08	0.00E+00	2.08E-05	1.07E-02	3.83E-10	1.02E-09	0.00E+00	5.34E-09	1.64E-09	0.00E+00	2.46E-05
Zn	1.62E-04	0.00E+00	6.37E-05	5.85E-05	4.30E-06	5.33E-05	4.49E-05	4.49E-06	1.29E-05	7.90E-06	3.29E-05	1.07E-04	2.38E-04	8.69E-03
Mo	3.53E-04	1.65E-05	4.40E-06	5.50E-06	2.28E-04	4.30E-06	7.79E-04	5.90E-04	3.90E-03	3.33E-03	4.43E-07	9.65E-06	2.06E-07	2.16E-04
Ti	2.27E-04	1.68E-05	2.97E-05	1.12E-04	6.53E-05	8.47E-04	2.64E-04	1.84E-05	1.00E-05	7.57E-06	8.23E-05	1.52E-03	1.78E-04	4.09E-03
Na	1.72E-03	2.12E-04	6.01E-04	3.95E-04	7.93E-05	3.23E-04	1.60E-04	7.91E-05	1.50E-04	2.01E-04	7.60E-05	3.21E-04	5.32E-04	3.37E-04
Si	0.00E+00	0.00E+00	0.00E+00	0.00E+00	0.00E+00	0.00E+00	2.44E-03	1.68E-03	0.00E+00	0.00E+00	0.00E+00	0.00E+00	4.32E-04	5.75E-05
Ca	0.00E+00	0.00E+00	0.00E+00	0.00E+00	5.47E-05	1.67E-04	4.09E-04	2.76E-05	1.96E-05	2.28E-05	6.22E-06	6.26E-05	1.40E-05	2.60E-03
Cs	0.00E+00	4.11E-08	0.00E+00	0.00E+00	1.33E-09	6.54E-09	2.92E-03	1.30E-09	2.29E-09	3.65E-09	1.20E-09	5.65E-09	2.27E-09	9.84E-09
Sn	0.00E+00	0.00E+00	0.00E+00	0.00E+00	7.77E-06	1.66E-04	5.18E-05	6.30E-06	9.77E-05	1.77E-04	5.40E-07	8.11E-06	5.96E-04	1.06E-03
K	4.72E-04	2.57E-04	2.03E-04	1.67E-04	1.29E-06	7.14E-07	8.82E-09	1.35E-06	1.82E-04	3.56E-05	3.71E-06	9.45E-06	5.10E-05	2.31E-05
Ba	8.89E-07	3.00E-07	3.75E-07	4.56E-07	1.19E-06	3.06E-04	7.42E-05	1.08E-07	1.22E-07	1.54E-07	3.82E-08	1.65E-07	2.30E-06	9.24E-04
Pb	4.16E-07	2.78E-08	2.75E-07	3.91E-07	0.00E+00	1.22E-04	2.12E-05	6.17E-08	1.99E-07	0.00E+00	6.96E-07	0.00E+00	0.00E+00	7.11E-05
Ge	0.00E+00	0.00E+00	0.00E+00	0.00E+00	1.01E-05	6.03E-05	8.65E-09	9.23E-06	3.23E-05	3.37E-05	2.03E-06	3.65E-06	1.71E-06	2.02E-05
Se	0.00E+00	0.00E+00	0.00E+00	0.00E+00	0.00E+00	6.35E-05	0.00E+00	0.00E+00	0.00E+00	0.00E+00	0.00E+00	8.87E-06	9.89E-07	7.34E-05
As	0.00E+00	0.00E+00	0.00E+00	0.00E+00	2.21E-05	7.36E-06	7.25E-06	2.45E-05	1.28E-05	1.12E-05	1.94E-07	4.94E-06	4.53E-08	1.02E-05
Au	0.00E+00	0.00E+00	0.00E+00	0.00E+00	0.00E+00	6.63E-06	1.97E-06	1.52E-07	5.43E-08	0.00E+00	1.63E-08	0.00E+00	0.00E+00	8.10E-05
W	1.37E-05	1.68E-07	0.00E+00	0.00E+00	0.00E+00	2.59E-07	2.22E-06	9.94E-06	2.75E-05	0.00E+00	4.78E-08	5.30E-07	0.00E+00	1.22E-05
Nd	3.69E-07	6.89E-08	3.46E-08	1.05E-07	2.01E-09	1.41E-08	3.79E-05	2.84E-09	1.70E-08	1.72E-08	3.38E-08	6.15E-09	8.81E-09	3.85E-07
Sr	5.02E-07	4.83E-07	7.22E-08	1.19E-07	2.73E-07	1.47E-06	1.74E-06	5.51E-08	6.10E-08	6.30E-08	3.10E-08	1.57E-07	5.60E-08	2.28E-05

Sym	LIR2032 (CC01)	CR2032 (CC02)	18650 (18650A)	RCR123A (RCR01)	AA LiFeS (AA01)	RCR123A (RCR02)	18650 (18650B)	AA LiSOCl (AA02)	ML2020 (CC03)	VL2020 (CC04)	Cell Phn. (Cell01)	Small-Pro (Cell02)	ED Batt (Cell03)	Elec. Dev. (Cell04)
Pd	0.00E+00	0.00E+00	0.00E+00	0.00E+00	5.47E-08	1.52E-06	1.87E-06	0.00E+00	0.00E+00	0.00E+00	0.00E+00	7.40E-06	1.91E-06	1.49E-05
Ru	0.00E+00	0.00E+00	0.00E+00	0.00E+00	8.38E-07	2.64E-09	1.60E-07	1.15E-06	8.15E-06	5.83E-06	0.00E+00	4.55E-07	1.14E-07	2.36E-06
Zr	0.00E+00	1.68E-08	0.00E+00	0.00E+00	4.83E-08	7.68E-07	4.34E-07	5.98E-08	2.22E-07	1.92E-07	1.91E-06	3.04E-08	3.03E-07	7.54E-06
Sb	0.00E+00	0.00E+00	0.00E+00	0.00E+00	1.37E-06	8.26E-07	8.64E-07	1.54E-06	2.19E-06	1.49E-06	3.38E-08	1.32E-06	1.72E-07	1.31E-06
Nb	1.00E-05	0.00E+00	4.99E-08	3.97E-07	0.00E+00	0.00E+00	0.00E+00	0.00E+00	0.00E+00	0.00E+00	0.00E+00	0.00E+00	0.00E+00	0.00E+00
Cd	4.79E-07	1.65E-08	0.00E+00	0.00E+00	2.22E-07	1.40E-08	1.92E-07	5.74E-07	3.88E-06	3.48E-06	1.06E-08	9.29E-08	4.75E-09	2.64E-07
Y	0.00E+00	0.00E+00	0.00E+00	0.00E+00	2.62E-09	7.26E-08	4.08E-06	2.28E-09	5.37E-09	7.82E-09	2.14E-08	7.55E-09	1.85E-08	4.25E-06
La	6.70E-07	2.60E-08	1.16E-07	2.59E-07	2.87E-09	1.59E-07	4.67E-06	2.10E-09	1.10E-08	1.02E-08	9.65E-08	5.94E-09	9.79E-08	5.10E-07
Lu	6.24E-09	0.00E+00	0.00E+00	0.00E+00	0.00E+00	9.00E-10	5.08E-06	0.00E+00	8.44E-12	0.00E+00	2.00E-10	0.00E+00	0.00E+00	1.47E-09
Ce	9.98E-07	1.82E-06	1.18E-07	4.46E-07	1.89E-08	6.98E-08	1.01E-07	3.80E-09	1.17E-08	2.09E-08	1.04E-07	1.11E-08	8.66E-07	4.99E-07
Rh	0.00E+00	0.00E+00	0.00E+00	0.00E+00	4.38E-08	5.95E-07	1.83E-08	1.99E-08	1.01E-07	7.02E-08	6.16E-09	3.47E-06	7.04E-08	3.04E-07
Gd	8.03E-08	2.15E-08	4.53E-08	3.99E-08	0.00E+00	4.61E-09	2.93E-06	8.52E-10	4.77E-09	4.37E-09	6.76E-09	1.92E-09	0.00E+00	3.74E-08
Rb	1.32E-07	7.93E-07	3.08E-08	0.00E+00	6.64E-08	6.38E-08	8.06E-09	8.40E-08	5.06E-07	3.85E-07	1.70E-08	8.07E-08	2.15E-08	2.18E-07
Hg	0.00E+00	0.00E+00	0.00E+00	0.00E+00	0.00E+00	5.48E-07	6.09E-09	2.52E-07	7.17E-07	0.00E+00	9.19E-09	0.00E+00	0.00E+00	5.57E-07
Pr	0.00E+00	1.55E-08	0.00E+00	0.00E+00	6.43E-10	3.84E-09	4.90E-07	7.96E-10	4.50E-09	4.55E-09	8.63E-09	2.28E-09	2.70E-09	1.81E-07
Ho	1.43E-08	6.62E-10	1.40E-09	1.03E-08	0.00E+00	1.19E-09	1.68E-07	6.28E-11	1.25E-10	0.00E+00	9.33E-10	3.08E-10	0.00E+00	4.21E-07
Re	3.00E-08	1.25E-09	0.00E+00	2.15E-07	0.00E+00	1.41E-09	3.82E-08	3.39E-08	1.38E-07	0.00E+00	5.23E-10	0.00E+00	0.00E+00	2.18E-08
Te	0.00E+00	0.00E+00	0.00E+00	0.00E+00	4.29E-09	8.63E-09	2.81E-09	8.17E-10	1.62E-08	1.75E-08	0.00E+00	3.15E-07	2.32E-08	4.62E-08
Hf	3.60E-10	0.00E+00	1.16E-10	0.00E+00	0.00E+00	1.03E-07	0.00E+00	2.12E-10	4.14E-09	0.00E+00	7.39E-08	3.96E-10	0.00E+00	2.37E-07
Sm	8.04E-08	1.45E-08	3.21E-08	9.92E-08	8.27E-10	6.67E-09	6.36E-09	4.03E-09	3.46E-08	2.35E-08	5.63E-09	4.39E-09	1.67E-09	2.62E-08
Eu	7.75E-09	2.88E-09	8.66E-09	6.10E-08	0.00E+00	4.64E-08	1.68E-09	5.92E-11	1.27E-09	1.00E-09	0.00E+00	0.00E+00	5.21E-10	1.42E-07
U	2.61E-08	0.00E+00	1.81E-08	1.57E-08	0.00E+00	1.60E-08	2.28E-08	3.23E-10	5.79E-09	0.00E+00	4.80E-08	0.00E+00	0.00E+00	8.47E-08
Ir	0.00E+00	0.00E+00	0.00E+00	0.00E+00	0.00E+00	5.81E-10	1.56E-07	7.36E-09	1.45E-08	0.00E+00	6.89E-10	0.00E+00	0.00E+00	8.55E-09
Ta	0.00E+00	0.00E+00	0.00E+00	0.00E+00	0.00E+00	1.09E-09	2.47E-09	6.59E-10	9.58E-08	0.00E+00	6.63E-10	1.14E-09	0.00E+00	6.29E-08
Pt	0.00E+00	0.00E+00	0.00E+00	0.00E+00	0.00E+00	8.23E-10	3.89E-09	1.58E-08	4.81E-08	0.00E+00	7.37E-10	0.00E+00	0.00E+00	6.53E-08
Er	4.55E-08	1.96E-09	1.25E-08	1.06E-08	0.00E+00	1.01E-09	2.75E-09	1.75E-10	2.05E-09	0.00E+00	2.36E-09	0.00E+00	0.00E+00	9.44E-09
Th	2.21E-08	1.88E-09	6.70E-11	9.07E-09	0.00E+00	3.49E-09	4.57E-09	5.13E-10	1.22E-09	0.00E+00	6.82E-09	0.00E+00	0.00E+00	1.68E-08
Tb	1.13E-08	1.37E-09	1.21E-09	1.88E-08	0.00E+00	7.85E-10	3.59E-10	6.77E-11	1.48E-10	2.91E-10	9.38E-10	1.90E-10	0.00E+00	3.10E-09
Yb	1.79E-08	0.00E+00	4.29E-09	2.75E-09	0.00E+00	1.55E-09	1.11E-09	1.01E-10	2.10E-11	0.00E+00	8.57E-10	0.00E+00	0.00E+00	6.58E-09
Tm	4.90E-09	0.00E+00	9.69E-10	3.76E-10	0.00E+00	1.16E-10	1.78E-10	8.37E-11	1.48E-09	0.00E+00	2.97E-10	0.00E+00	0.00E+00	2.32E-09

TABLE XXVII

INITIAL ACTIVITIES OF RADIOISOTOPES AFTER EXPOSURE

Activities are corrected based on radioisotope half-life to the point right after exposure. Corrections associated with detector efficiencies and geometries are also applied. For the UMass FNI indication marks Blue, Gold, and Orange are used to distinguish batteries, and for the TRIGA results, Inner and Outer are illustrated in Figure 14.

LIR2032 (CC01) Outer (LiCoO ₂)	
TRIGA (Run 1)	Time After Exposure: 84181 sec
Radioisotope	Activity (μCi)
W-187	4.06E-01
Mn-56	2.85E+02
Mn-54	3.58E-03
As-76	6.68E-02
Ga-72	6.34E-02
Co-58	2.51E-02
Co-60	4.28E-01
Cu-64	7.71E+01
Fe-59	1.85E-02
Na-24	1.36E-01
Cr-51	9.80E-01
Sb-122	9.27E-03
Mo-99	2.98E-02
Tc-99m	3.14E-01
LIR2032 (CC01) Outer (LiCoO ₂)	
TRIGA (Run 1)	Time After Exposure: 247797 sec
Radioisotope	Activity (μCi)
W-187	4.14E-01
Mn-54	4.47E-03
As-76	7.40E-02
Ga-72	7.68E-02
Co-58	3.77E-02
Co-60	4.29E-01
Cu-64	7.20E+01
Fe-59	1.65E-02
Na-24	1.40E-01
Cr-51	9.75E-01
Sb-122	1.09E-02
Tc-99m	4.01E+01
Mo-99	3.09E-02
K-40	1.47E-02

LIR2032 (CC01) Inner (LiCoO ₂)	
TRIGA (Run 1)	Time After Exposure: 84358 sec
Radioisotope	Activity (μCi)
W-187	2.25E-01
Mn-56	2.89E+02
Mn-54	1.37E-04
As-76	6.03E-02
Ga-72	6.44E-02
Co-58	3.21E-02
Co-60	4.42E-01
Cu-64	7.39E+01
Fe-59	1.39E-02
Na-24	8.59E-02
Cr-51	9.02E-01
Sb-122	1.34E-02
Tc-99m	1.72E-01
Mo-99	1.94E-02
LIR2032 (CC01) Inner (LiCoO ₂)	
TRIGA (Run 1)	Time After Exposure: 247676 sec
Radioisotope	Activity (μCi)
W-187	2.26E-01
Mn-54	4.19E-03
As-76	6.80E-02
Ga-72	7.70E-02
Co-58	3.32E-02
Co-60	4.43E-01
Cu-64	6.82E+01
Fe-59	1.45E-02
Na-24	1.62E-01
Cr-51	9.02E-01
Sb-122	1.05E-02
Tc-99m	2.19E+01
K-40	1.50E-02

RCR123A (RCR01) (LiFePO ₄)	
TRIGA (Run 1)	Time After Exposure: 159416 sec
Radioisotope	Activity (μCi)
Mn-54	2.95E-02
As-76	3.01E-01
Ga-72	2.05E-01
Co-58	6.45E-02
Cu-64	1.33E+03
Fe-59	9.16E-02
Na-24	2.85E+00
Sb-122	8.41E-02
La-140	4.73E-03
K-40	1.14E-02
RCR123A (RCR01) (LiFePO ₄)	
TRIGA (Run 1)	Time After Exposure: 256872 sec
Radioisotope	Activity (μCi)
Mn-54	2.90E-02
As-76	2.97E-01
Ga-72	2.45E-01
Co-58	7.41E-02
Co-60	1.09E-03
Cu-64	1.33E+03
Fe-59	9.30E-02
Na-24	2.84E+00
Sb-122	2.08E-02
La-140	3.73E-03
K-40	1.30E-02

18650 (18650A) (LiMnNiO ₂)	
TRIGA (Run 1)	Time After Exposure: 164680 sec
Radioisotope	Activity (μCi)
Mn-56	2.82E+04
Mn-54	3.89E-02
As-76	3.41E-01
Ga-72	2.96E-01
Co-58	1.22E+00
Co-60	3.90E+00
Cu-64	2.06E+03
Fe-59	1.18E-01
Na-24	3.84E+00
Sb-122	3.94E-02
La-140	3.76E-03
18650 (18650A) (LiMnNiO ₂)	
TRIGA (Run 1)	Time After Exposure: 261018 sec
Radioisotope	Activity (μCi)
Mn-54	3.42E-02
As-76	2.98E-01
Ga-72	4.21E-01
Co-58	1.24E+00
Co-60	3.92E+00
Cu-64	2.04E+03
Fe-59	1.18E-01
Na-24	3.89E+00
Sb-122	4.29E-02
La-140	5.47E-03
K-40	1.01E-02

CR2032 (CC02) Outer (LiMnO ₂)	
TRIGA (Run 1)	Time After Exposure: 76442 sec
Radioisotope	Activity (μCi)
Mn-56	1.46E+04
Fe-59	2.50E-02
Na-24	8.55E-02
Cr-51	6.71E-01
CR2032 (CC02) Outer (LiMnO ₂)	
TRIGA (Run 1)	Time After Exposure: 251678 sec
Radioisotope	Activity (μCi)
W-187	1.39E-02
Mn-54	1.05E-02
As-76	8.18E-02
Co-58	1.22E-02
Co-60	1.27E-03
Fe-59	2.72E-02
Na-24	8.46E-02
Cr-51	6.99E-01
Sb-122	8.13E-03
Tc-99m	5.03E+00
K-40	1.15E-02

CR2032 (CC02) Inner (LiMnO ₂)	
TRIGA (Run 1)	Time After Exposure: 77350 sec
Radioisotope	Activity (μCi)
Mn-56	1.18E+04
Fe-59	1.87E-02
Na-24	7.40E-02
Cr-51	5.64E-01
CR2032 (CC02) Inner (LiMnO ₂)	
TRIGA (Run 1)	Time After Exposure: 251520 sec
Radioisotope	Activity (μCi)
Mn-54	8.71E-03
As-76	8.23E-02
Co-58	1.11E-02
Co-60	1.10E-03
Fe-59	2.45E-02
Na-24	7.44E-02
Cr-51	5.75E-01
Sb-122	7.45E-03
Tc-99m	4.03E+00
K-40	9.00E-03

Electronic Device Battery (Cell03)	
TRIGA (Run 2)	Time After Exposure: 100941 sec
Radioisotope	Activity (μCi)
As-76	1.88E-02
Au-198	2.45E-01
Co-58	1.13E-02
Co-60	1.60E+00
Cu-64	2.68E+02
Ga-72	3.01E-02
K-40	1.61E-02
Mn-56	2.21E+01
Na-24	1.50E-01
Electronic Device Battery (Cell03)	
TRIGA (Run 2)	Time After Exposure: 184557 sec
Radioisotope	Activity (μCi)
Au-198	2.27E-01
As-76	1.77E-02
Co-58	9.89E-03
Co-60	1.57E+00
Cu-64	2.60E+02
K-40	1.85E-02
Na-24	1.51E-01

LIR2032 (CC01) (LiCoO ₂)	
TRIGA (Run 2)	Time After Exposure: 93062 sec
Radioisotope	Activity (μCi)
As-76	6.03E-02
Co-58	2.37E-02
Co-60	8.10E-01
Cr-51	1.85E+00
Cu-64	1.43E+02
Fe-59	2.55E-02
Ga-72	7.87E-02
K-40	3.25E-02
Mn-56	5.61E+02
Mo-99	3.47E-02
Na-24	2.52E-01
Sb-122	1.09E-02
Tc-99m	3.28E-01
W-187	4.07E-01
LIR2032 (CC01) (LiCoO ₂)	
TRIGA (Run 2)	Time After Exposure: 176308 sec
Radioisotope	Activity (μCi)
As-76	5.25E-02
Co-58	2.39E-02
Co-60	8.09E-01
Cr-51	1.83E+00
Cu-64	1.46E+02
Fe-59	2.78E-02
Ga-72	8.97E-02
K-40	1.72E-02
Mo-99	2.39E-02
Na-24	2.30E-01
Sb-122	7.80E-03
Tc-99m	4.16E+00
W-187	4.21E-01

CR2032 (CC02) (LiMnO ₂)	
TRIGA (Run 2)	Time After Exposure: 85737 sec
Radioisotope	Activity (μCi)
As-76	3.57E-02
Cr-51	7.41E-01
Fe-59	4.00E-02
Mn-56	1.63E+04
Na-24	1.13E-01
CR2032 (CC02) (LiMnO ₂)	
TRIGA (Run 2)	Time After Exposure: 172265 sec
Radioisotope	Activity (μCi)
As-76	4.33E-02
Co-58	4.57E-03
Co-60	1.00E-03
Cr-51	7.40E-01
Cu-64	4.46E-01
Fe-59	2.79E-02
Ga-72	1.50E-02
K-40	1.79E-03
K-42	4.95E-03
La-140	2.29E-04
Mn-54	3.60E-03
Mn-56	1.47E+04
Mo-99	1.45E-03
Na-24	9.04E-02
Sb-122	4.18E-03
Sm-153	5.28E-04
W-187	9.38E-03

Electronic Device (Cell04)	
TRIGA (Run 2)	Time After Exposure: 113649 sec
Radioisotope	Activity (μCi)
As-76	2.43E-01
Au-198	9.66E+00
Co-58	7.33E-02
Co-60	1.48E+00
Cr-51	4.02E+00
Cu-64	7.64E+02
Fe-59	6.62E-02
Ga-72	6.23E-01
La-140	4.07E-04
Mn-56	2.49E+03
Mo-99	2.41E-01
Na-24	2.66E+00
Sb-122	4.50E-02
Sn-117m	9.70E-03
Ta-182	6.28E-01
Tc-99m	1.50E+00
W-187	3.18E+00
Zn-65	5.06E-02
Zn-69m	6.93E-01
Electronic Device (Cell04)	
TRIGA (Run 2)	Time After Exposure: 191901 sec
Radioisotope	Activity (μCi)
Ag-110m	9.04E-03
As-76	2.13E-01
Au-198	1.01E+01
Co-58	6.83E-02
Co-60	1.60E+00
Cr-51	3.45E+00
Cu-64	7.02E+02
Fe-59	5.66E-02
Ga-72	6.35E-01
K-40	1.93E+00
La-140	4.56E-04
Na-24	2.53E+00
Sb-122	3.89E-02
Sn-117m	1.42E-02
Ta-182	6.41E-01
Tc-99m	1.18E+01
W-187	3.05E+00
Zn-65	5.39E-02
Zn-69m	6.88E-01

Electronic Device (Cell04)	
TRIGA (Run 2)	Time After Exposure: 259310 sec
Radioisotope	Activity (μCi)
Ag-110m	8.12E-03
As-76	2.43E-01
Au-198	9.87E+00
Co-58	7.93E-02
Co-60	1.48E+00
Cr-51	4.25E+00
Cu-64	6.93E+02
Fe-59	6.87E-02
Ga-72	7.18E-01
K-40	1.07E+00
La-140	2.58E-04
Mn-54	2.36E-04
Na-24	2.36E+00
Sb-122	4.52E-02
Sn-117m	1.07E-02
Ta-182	6.24E-01
Tc-99m	1.09E+02

Lithium AA (AA01) Gold (Li-FeS ₂)	
FNI (Run 1)	Time After Exposure: 87609 sec
Radioisotope	Activity (μCi)
As-76	1.47E-01
Au-198	~Background
Co-58	4.78E-04
Co-60	~Background
Cr-51	
Cu-64	5.72E-01
Fe-59	6.93E-04
Ga-72	4.54E-03
I-126	
Mn-54	1.45E-03
Mn-56	2.36E+00
Mo-99	9.50E-03
Na-24	6.66E-03
Sb-122	4.37E-03
Sb-124	4.48E-04
Se-75	
Sn-117m	
W-187	1.41E-02
Lithium AA (AA01) Gold (Li-FeS ₂)	
FNI (Run 1)	Time After Exposure: 1031916 sec
Radioisotope	Activity (μCi)
As-76	7.74E-01
Au-198	2.99E-03
Co-58	2.90E-03
Co-60	4.93E-04
Cr-51	4.84E-03
Cu-64	
Fe-59	3.30E-03
Ga-72	
I-126	1.66E-04
Mn-54	2.19E-03
Mn-56	
Mo-99	7.94E-03
Na-24	
Sb-122	7.58E-03
Sb-124	1.95E-04
Se-75	7.30E-05
Sn-117m	3.85E-05
W-187	

Lithium AA (AA01) Gold (Li-FeS ₂)	
FNI (Run 1)	Time After Exposure: 1633178 sec
Radioisotope	Activity (μCi)
As-76	
Au-198	2.63E-03
Co-58	2.81E-03
Co-60	4.79E-04
Cr-51	4.69E-03
Cu-64	
Fe-59	3.25E-03
Ga-72	
I-126	No Count
Mn-54	2.07E-03
Mn-56	
Mo-99	
Na-24	
Sb-122	9.95E-03
Sb-124	2.17E-04
Se-75	9.80E-05
Sn-117m	4.37E-05
W-187	

Lithium AA (AA01) Blue (Li-FeS ₂)	
FNI (Run 1)	Time After Exposure: 522336 sec
Radioisotope	Activity (μCi)
As-76	7.22E-01
Au-198	2.71E-03
Co-58	2.63E-03
Co-60	5.14E-04
Cr-51	6.87E-03
Cu-64	
Fe-59	2.90E-03
Ga-72	
I-126	
Mn-54	1.80E-03
Mn-56	
Mo-99	8.85E-03
Na-24	3.20E-02
Sb-122	5.82E-03
Sb-124	2.18E-04
Se-75	7.72E-05
Lithium AA (AA01) Blue (Li-FeS ₂)	
FNI (Run 1)	Time After Exposure: 1565800 sec
Radioisotope	Activity (μCi)
As-76	
Au-198	3.28E-03
Co-58	2.53E-03
Co-60	4.92E-04
Cr-51	5.38E-03
Cu-64	
Fe-59	3.24E-03
Ga-72	
I-126	1.41E-04
Mn-54	1.95E-03
Mn-56	
Mo-99	
Na-24	
Sb-122	9.40E-03
Sb-124	2.01E-04
Se-75	7.08E-05
Sn-117m	3.58E-05
W-187	

ML2020 (CC03) Gold (LiMnO ₂)	
FNI (Run 1)	Time After Exposure: 340599 sec
Radioisotope	Activity (μCi)
As-76	1.29E-02
Au-198	8.40E-05
Co-58	1.60E-03
Co-60	2.75E-04
Cr-51	1.19E-02
Fe-59	4.76E-04
Mn-54	3.77E-04
Mo-99	4.20E-02
Na-24	4.21E-03
Nb-92m	4.76E-05
Sb-122	9.93E-04
Sb-124	1.42E-04
Sn-117m	1.99E-05
Ta-182	
W-187	4.57E-02
ML2020 (CC03) Gold (LiMnO ₂)	
FNI (Run 1)	Time After Exposure: 1117234 sec
Radioisotope	Activity (μCi)
As-76	
Au-198	
Co-58	2.10E-03
Co-60	3.57E-04
Cr-51	1.56E-02
Fe-59	5.70E-04
Mn-54	4.30E-04
Mo-99	4.74E-02
Na-24	
Nb-92m	
Sb-122	1.70E-03
Sb-124	3.26E-05
Sn-117m	
Ta-182	
W-187	

ML2020 (CC03) Gold (LiMnO ₂)	
FNI (Run 1)	Time After Exposure: 1729628 sec
Radioisotope	Activity (μCi)
As-76	
Au-198	
Co-58	2.08E-03
Co-60	3.71E-04
Cr-51	1.53E-02
Fe-59	5.88E-04
Mn-54	4.16E-04
Mo-99	4.82E-02
Na-24	
Nb-92m	
Sb-122	
Sb-124	
Sn-117m	2.95E-05
Ta-182	8.34E-05
W-187	

ML2020 (CC03) Blue (LiMnO ₂)	
FNI (Run 1)	Time After Exposure: 600558 sec
Radioisotope	Activity (μCi)
As-76	1.47E-02
Au-198	
Co-58	2.18E-03
Co-60	3.55E-04
Cr-51	1.48E-02
Fe-59	5.50E-04
Mn-54	4.26E-04
Mo-99	5.00E-02
Na-24	
Nb-92m	
Sb-122	1.06E-03
Sb-124	2.79E-05
Sn-117m	3.20E-05
Ta-182	
W-187	6.08E-02
ML2020 (CC03) Blue (LiMnO ₂)	
FNI (Run 1)	Time After Exposure: 1210606 sec
Radioisotope	Activity (μCi)
As-76	
Au-198	
Co-58	2.32E-03
Co-60	3.74E-04
Cr-51	1.68E-02
Fe-59	6.26E-04
Mn-54	4.81E-04
Mo-99	5.80E-02
Na-24	
Nb-92m	
Sb-122	1.14E-03
Sb-124	3.07E-05
Sn-117m	3.40E-05
Ta-182	9.71E-05
W-187	

VL2020 (CC04) Gold (LiMnO ₂)	
FNI (Run 1)	Time After Exposure: 91521 sec
Radioisotope	Activity (μCi)
As-76	3.51E-03
Au-198	~Background
Co-58	4.71E-04
Co-60	~Background
Cr-51	3.46E-03
Cu-64	4.66E-02
Fe-59	1.36E-04
Ga-72	2.14E-03
Mn-54	
Mn-56	2.24E+00
Mo-99	1.27E-02
Na-24	1.51E-03
Sb-122	5.84E-04
Sb-124	
Sn-117m	
W-187	2.37E-02
VL2020 (CC04) Gold (LiMnO ₂)	
FNI (Run 1)	Time After Exposure: 1120380 sec
Radioisotope	Activity (μCi)
As-76	
Au-198	
Co-58	2.14E-03
Co-60	4.55E-04
Cr-51	1.57E-02
Cu-64	
Fe-59	6.32E-04
Ga-72	
Mn-54	4.41E-04
Mn-56	
Mo-99	4.74E-02
Na-24	
Sb-122	1.06E-03
Sb-124	1.75E-05
Sn-117m	3.77E-05
W-187	

VL2020 (CC04) Gold (LiMnO ₂)	
FNI (Run 1)	Time After Exposure: 1736954 sec
Radioisotope	Activity (μCi)
As-76	
Au-198	
Co-58	2.16E-03
Co-60	4.71E-04
Cr-51	1.53E-02
Cu-64	
Fe-59	6.36E-04
Ga-72	
Mn-54	4.44E-04
Mn-56	
Mo-99	4.81E-02
Na-24	
Sb-122	
Sb-124	
Sn-117m	4.19E-05
W-187	

VL2020 (CC04) Blue (LiMnO ₂)	
FNI (Run 1)	Time After Exposure: 598414 sec
Radioisotope	Activity (μCi)
As-76	1.29E-02
Au-198	7.50E-05
Co-58	2.05E-03
Co-60	4.18E-04
Cr-51	1.54E-02
Cu-64	
Fe-59	6.39E-04
Ga-72	
Mn-54	4.29E-04
Mn-56	
Mo-99	5.40E-02
Na-24	
Sb-122	1.25E-03
Sb-124	2.98E-05
Sn-117m	4.89E-05
W-187	8.52E-02
VL2020 (CC04) Blue (LiMnO ₂)	
FNI (Run 1)	Time After Exposure: 1212571 sec
Radioisotope	Activity (μCi)
As-76	
Au-198	
Co-58	2.30E-03
Co-60	4.62E-04
Cr-51	1.72E-02
Cu-64	
Fe-59	6.79E-04
Ga-72	
Mn-54	4.78E-04
Mn-56	
Mo-99	5.67E-02
Na-24	
Sb-122	1.19E-03
Sb-124	3.14E-05
Sn-117m	7.67E-05
W-187	

Lithium AA (AA02) Gold (Li-SOCl ₂)	
FNI (Run 1)	Time After Exposure: 338400 sec
Radioisotope	Activity (μCi)
As-76	8.10E-02
Bi-206	1.47E-04
Co-58	5.42E-03
Co-60	7.59E-04
Cr-51	1.16E-02
Fe-59	4.26E-04
Ga-72	4.69E-03
Mn-54	3.90E-04
Mo-99	8.35E-03
Na-24	1.49E-02
Sb-122	2.07E-03
Sb-124	7.95E-05
W-187	4.78E-02
Lithium AA (AA02) Gold (Li-SOCl ₂)	
FNI (Run 1)	Time After Exposure: 1134766 sec
Radioisotope	Activity (μCi)
As-76	
Bi-206	
Co-58	2.19E-02
Co-60	3.05E-03
Cr-51	4.89E-02
Fe-59	1.95E-03
Ga-72	
Mn-54	1.39E-03
Mo-99	3.11E-02
Na-24	
Sb-122	6.29E-03
Sb-124	2.64E-04
W-187	
Lithium AA (AA02) Gold (Li-SOCl ₂)	
FNI (Run 1)	Time After Exposure: 1726786 sec
Radioisotope	Activity (μCi)
As-76	
Bi-206	
Co-58	2.20E-02
Co-60	3.10E-03
Cr-51	4.93E-02
Fe-59	2.02E-03
Ga-72	
Mn-54	1.46E-03
Mo-99	
Na-24	
Sb-122	
Sb-124	2.01E-04
W-187	

Lithium AA (AA02) Blue (Li-SOCl ₂)	
FNI (Run 1)	Time After Exposure: 525462 sec
Radioisotope	Activity (μCi)
As-76	2.56E-01
Au-198	3.85E-04
Bi-206	
Co-58	1.49E-02
Co-60	2.45E-03
Cr-51	3.73E-02
Fe-59	1.52E-03
Ga-72	No Count
Mn-54	9.98E-04
Mo-99	2.42E-02
Na-24	4.05E-02
Sb-122	4.35E-03
Sb-124	1.79E-04
W-187	1.40E-01
Lithium AA (AA02) Blue (Li-SOCl ₂)	
FNI (Run 1)	Time After Exposure: 1629683 sec
Radioisotope	Activity (μCi)
As-76	
Au-198	
Bi-206	
Co-58	1.84E-02
Co-60	2.85E-03
Cr-51	4.61E-02
Fe-59	1.99E-03
Ga-72	
Mn-54	1.19E-03
Mo-99	2.74E-02
Na-24	
Sb-122	
Sb-124	2.51E-04
W-187	

Cell Phone Battery (Cell01) Gold (LiCoO ₂)	
FNI (Run 1)	Time After Exposure: 83701 sec
Radioisotope	Activity (μCi)
Au-198	1.21E-03
Co-58	1.03E-03
Co-60	8.97E-02
Cu-64	1.08E+01
Fe-59	
Ga-72	1.05E-02
Mn-56	6.44E+00
Na-24	4.93E-02
Sb-122	1.84E-03
Cell Phone Battery (Cell01) Gold (LiCoO ₂)	
FNI (Run 1)	Time After Exposure: 1193183 sec
Radioisotope	Activity (μCi)
Au-198	
Co-58	4.32E-03
Co-60	4.92E-01
Cu-64	
Fe-59	3.27E-03
Ga-72	
Mn-56	
Na-24	
Sb-122	
Cell Phone Battery (Cell01) Gold (LiCoO ₂)	
FNI (Run 1)	Time After Exposure: 1724186 sec
Radioisotope	Activity (μCi)
Au-198	
Co-58	4.40E-03
Co-60	4.76E-01
Cu-64	
Fe-59	5.38E-03
Ga-72	
Mn-56	
Na-24	
Sb-122	

Cell Phone Battery (Cell01) Blue (LiCoO ₂)	
FNI (Run 1)	Time After Exposure: 602674 sec
Radioisotope	Activity (μCi)
Au-198	
Co-58	2.23E-04
Co-60	2.24E-02
Cu-64	
Fe-59	1.72E-04
Ga-72	
Mn-56	
Na-24	
Sb-122	
Cell Phone Battery (Cell01) Blue (LiCoO ₂)	
FNI (Run 1)	Time After Exposure: 1206972 sec
Radioisotope	Activity (μCi)
Au-198	
Co-58	4.41E-03
Co-60	4.92E-01
Cu-64	
Fe-59	4.42E-03
Ga-72	
Mn-56	
Na-24	
Sb-122	

18650 (18650B) Gold (LiMnNiO ₂)	
FNI (Run 1)	Time After Exposure: 96223 sec
Radioisotope	Activity (μCi)
Au-198	2.24E-03
Br-82	3.18E-01
Co-58	1.12E-02
Co-60	1.76E-01
Cr-51	
Cu-64	2.41E+01
Fe-59	2.17E-03
Ga-72	1.77E-02
Mn-54	
Mn-56	4.05E+00
Na-24	4.47E-02
Sn-113	
Sn-117m	
Ag-110m	
18650 (18650B) Gold (LiMnNiO ₂)	
FNI (Run 1)	Time After Exposure: 1024201 sec
Radioisotope	Activity (μCi)
Au-198	8.07E-03
Br-82	7.33E-01
Co-58	4.88E-02
Co-60	7.03E-01
Cr-51	3.57E-03
Cu-64	
Fe-59	8.63E-03
Ga-72	
Mn-54	2.02E-03
Mn-56	
Na-24	
Sn-113	
Sn-117m	1.09E-03
18650 (18650B) Gold (LiMnNiO ₂)	
FNI (Run 1)	Time After Exposure: 1650408 sec
Radioisotope	Activity (μCi)
Au-198	
Br-82	
Co-58	4.65E-02
Co-60	7.14E-01
Cr-51	
Cu-64	
Fe-59	8.62E-03
Ga-72	
Mn-54	2.23E-03
Mn-56	
Na-24	
Sn-113	
Sn-117m	9.80E-04
Ag-110m	

18650 (18650B) Blue (LiMnNiO ₂)	
FNI (Run 1)	Time After Exposure: 609871 sec
Radioisotope	Activity (μCi)
Au-198	4.67E-03
Br-82	4.47E-01
Co-58	1.80E-02
Co-60	2.77E-01
Cr-51	
Cu-64	
Fe-59	2.96E-03
Ga-72	
Mn-54	8.28E-04
Mn-56	
Na-24	
Sn-113	
Sn-117m	8.60E-04
18650 (18650B) Blue (LiMnNiO ₂)	
FNI (Run 1)	Time After Exposure: 1202259 sec
Radioisotope	Activity (μCi)
Au-198	
Br-82	9.06E-01
Co-58	3.53E-02
Co-60	5.55E-01
Cr-51	3.62E-03
Cu-64	
Fe-59	6.63E-03
Ga-72	
Mn-54	1.61E-03
Mn-56	
Na-24	
Sn-113	7.42E-04
Sn-117m	1.34E-03

RCR123A (RCR02) Gold (LiFePO ₄)	
FNI (Run 1)	Time After Exposure: 342769 sec
Radioisotope	Activity (μCi)
Ag-110m	
Au-198	3.41E-03
Br-82	3.71E-01
Co-58	1.61E-03
Co-60	6.36E-02
Cu-64	1.43E+01
Fe-59	1.11E-03
Mn-54	8.59E-04
Na-24	1.92E-02
Sb-122	2.71E-02
Sb-124	8.23E-04
Sn-113	
Sn-117m	7.29E-04
RCR123A (RCR02) Gold (LiFePO ₄)	
FNI (Run 1)	Time After Exposure: 1199857 sec
Radioisotope	Activity (μCi)
Ag-110m	
Au-198	9.37E-03
Br-82	7.83E-01
Co-58	3.41E-03
Co-60	1.72E-01
Cu-64	
Fe-59	3.19E-03
Mn-54	1.13E-03
Na-24	
Sb-122	6.75E-02
Sb-124	1.94E-03
Sn-113	4.82E-04
Sn-117m	1.87E-03
RCR123A (RCR02) Gold (LiFePO ₄)	
FNI (Run 1)	Time After Exposure: 1650408 sec
Radioisotope	Activity (μCi)
Ag-110m	4.76E-04
Au-198	1.06E-02
Br-82	
Co-58	3.75E-03
Co-60	1.94E-01
Cu-64	
Fe-59	3.57E-03
Mn-54	1.36E-03
Na-24	
Sb-122	6.48E-02
Sb-124	1.98E-03
Sn-113	6.19E-04
Sn-117m	1.92E-03

RCR123A (RCR02) Blue (LiFePO ₄)	
FNI (Run 1)	Time After Exposure: 612037 sec
Radioisotope	Activity (μCi)
Ag-110m	
Au-198	3.37E-03
Br-82	2.99E-01
Co-58	1.57E-03
Co-60	5.02E-02
Cu-64	
Fe-59	8.12E-04
Mn-54	
Na-24	
Sb-122	2.02E-02
Sb-124	5.40E-04
Sn-113	
Sn-117m	3.69E-04
RCR123A (RCR02) Blue (LiFePO ₄)	
FNI (Run 1)	Time After Exposure: 1047203 sec
Radioisotope	Activity (μCi)
Ag-110m	
Au-198	7.00E-03
Br-82	6.65E-01
Co-58	5.11E-03
Co-60	1.43E-01
Cu-64	
Fe-59	2.48E-03
Mn-54	8.52E-04
Na-24	
Sb-122	4.97E-02
Sb-124	1.18E-03
Sn-113	3.28E-04
Sn-117m	1.25E-03

Small-Profile Battery (Cell02) Gold (LiCoO ₂)	
FNI (Run 1)	Time After Exposure: 344825 sec
Radioisotope	Activity (μCi)
Au-198	5.49E-05
Co-58	3.13E-03
Co-60	1.39E-03
Cu-64	1.12E+01
Sb-122	~Background
Sb-124	
Small-Profile Battery (Cell02) Gold (LiCoO ₂)	
FNI (Run 1)	Time After Exposure: 1131400 sec
Radioisotope	Activity (μCi)
Au-198	
Co-58	3.24E-03
Co-60	1.43E-03
Cu-64	
Sb-122	
Sb-124	
Small-Profile Battery (Cell02) Gold (LiCoO ₂)	
FNI (Run 1)	Time After Exposure: 1799711 sec
Radioisotope	Activity (μCi)
Au-198	
Co-58	3.34E-03
Co-60	1.49E-03
Cu-64	
Sb-122	
Sb-124	

Small-Profile Battery (Cell02) Blue (LiCoO ₂)	
FNI (Run 1)	Time After Exposure: 520244 sec
Radioisotope	Activity (μCi)
Au-198	2.16E-04
Co-58	2.71E-03
Co-60	1.07E-03
Cu-64	
Sb-122	1.29E-01
Sb-124	3.10E-03
Small-Profile Battery (Cell02) Blue (LiCoO ₂)	
FNI (Run 1)	Time After Exposure: 1626659 sec
Radioisotope	Activity (μCi)
Au-198	
Co-58	3.64E-03
Co-60	1.53E-03
Cu-64	
Sb-122	1.59E-01
Sb-124	4.03E-03

CR2032 (CC02) (LiMnO ₂)	
FNI (Run 2)	Time After Exposure: 92318 sec
Radioisotope	Activity (μCi)
As-76	7.23E-04
Co-58	
Cr-51	1.21E-03
Fe-59	
Mn-54	1.41E-04
Mn-56	2.48E+01
Na-24	1.40E-04
CR2032 (CC02) (LiMnO ₂)	
FNI (Run 2)	Time After Exposure: 956318 sec
Radioisotope	Activity (μCi)
As-76	
Co-58	6.72E-04
Cr-51	2.11E-02
Fe-59	9.38E-04
Mn-54	7.65E-04
Mn-56	
Na-24	

CR2032 (CC02) Orange (LiMnO ₂)	
FNI (Run 2)	Time After Exposure: 250782 sec
Radioisotope	Activity (μCi)
As-76	1.95E-02
Co-58	8.95E-04
Co-60	~Background
Cr-51	2.39E-02
Fe-59	9.91E-04
Ga-72	2.73E-02
Mn-54	
Na-24	1.46E-03
W-187	1.02E-02
CR2032 (CC02) Orange (LiMnO ₂)	
FNI (Run 2)	Time After Exposure: 946462 sec
Radioisotope	Activity (μCi)
As-76	
Co-58	8.20E-04
Co-60	1.23E-04
Cr-51	2.26E-02
Fe-59	1.05E-03
Ga-72	
Mn-54	9.25E-04
Na-24	
W-187	

Lithium AA (AA01) (Li-FeS ₂)	
FNI (Run 2)	Time After Exposure: 248768 sec
Radioisotope	Activity (μCi)
As-76	8.17E-01
Au-198	2.38E-03
Co-58	2.90E-03
Co-60	5.21E-04
Cr-51	4.75E-03
Cu-64	2.68E+00
Fe-59	4.52E-03
Ga-72	1.73E-02
Mn-54	2.64E-03
Mo-99	1.05E-02
Na-24	3.04E-02
Sb-122	
Sb-124	
W-187	6.31E-02
Lithium AA (AA01) (Li-FeS ₂)	
FNI (Run 2)	Time After Exposure: 955336 sec
Radioisotope	Activity (μCi)
As-76	8.72E-01
Au-198	2.64E-03
Co-58	2.80E-03
Co-60	3.64E-04
Cr-51	4.16E-03
Cu-64	
Fe-59	2.69E-03
Ga-72	
Mn-54	2.03E-03
Mo-99	6.14E-03
Na-24	
Sb-122	6.52E-03
Sb-124	1.81E-04
W-187	

Electronic Device Battery (Cell03)	
FNI (Run 2)	Time After Exposure: 87827 sec
Radioisotope	Activity (μCi)
As-76	1.49E-03
Au-198	1.51E-02
Co-58	1.20E-03
Co-60	2.30E-02
Cu-64	4.17E+00
Fe-59	
Ga-72	2.80E-03
Mn-56	4.11E-01
Na-24	7.57E-03
Te-123m	
Electronic Device Battery (Cell03)	
FNI (Run 2)	Time After Exposure: 959578 sec
Radioisotope	Activity (μCi)
As-76	
Au-198	2.21E-02
Co-58	1.75E-03
Co-60	3.29E-02
Cu-64	
Fe-59	2.58E-04
Ga-72	
Mn-56	
Na-24	
Te-123m	2.62E-04

Electronic Device (Cell04)	
FNI (Run 2)	Time After Exposure: 81707 sec
Radioisotope	Activity (μCi)
Ag-110m	
As-76	8.93E-03
Au-198	1.71E-01
Ba-131	
Co-58	2.67E-03
Co-60	9.90E-03
Cr-51	
Cu-64	3.71E+00
Fe-59	
Ga-72	2.45E-02
Mn-54	
Mn-56	1.04E+01
Na-24	5.18E-02
Sb-122	
Sn-113	
Ta-182	1.63E-02
W-187	7.72E-02
Zn-65	
Zn-69m	1.37E-02
Electronic Device (Cell04)	
FNI (Run 2)	Time After Exposure: 957391 sec
Radioisotope	Activity (μCi)
Ag-110m	5.90E-04
As-76	
Au-198	7.35E-01
Ba-131	1.97E-03
Co-58	8.26E-03
Co-60	3.58E-02
Cr-51	2.32E-02
Cu-64	
Fe-59	2.93E-03
Ga-72	
Mn-54	8.55E-04
Mn-56	
Na-24	
Sb-122	4.13E-03
Sn-113	8.25E-04
Ta-182	6.48E-02
W-187	
Zn-65	1.36E-03
Zn-69m	

18650 (18650A) (LiMnNiO ₂)	
FNI (Run 2)	Time After Exposure: 79180 sec
Radioisotope	Activity (μCi)
Co-58	2.11E-02
Co-60	4.73E-02
Cu-64	2.03E+01
Fe-59	
Mn-54	3.19E-03
Mn-56	3.26E+02
Na-24	3.93E-02
18650 (18650A) (LiMnNiO ₂)	
FNI (Run 2)	Time After Exposure: 937701 sec
Radioisotope	Activity (μCi)
Co-58	8.85E-02
Co-60	1.81E-01
Cu-64	
Fe-59	4.57E-03
Mn-54	2.52E-03
Mn-56	
Na-24	

RCR123A (RCR01) (LiFePO ₄)	
FNI (Run 2)	Time After Exposure: 83772 sec
Radioisotope	Activity (μCi)
As-76	9.23E-03
Co-58	9.19E-04
Cu-64	9.03E+00
Fe-59	
Ga-72	8.89E-03
Mn-54	
Mn-56	1.82E+00
Na-24	1.66E-02
Sb-122	
Sb-124	
RCR123A (RCR01) (LiFePO ₄)	
FNI (Run 2)	Time After Exposure: 955446 sec
Radioisotope	Activity (μCi)
As-76	
Co-58	4.34E-03
Cu-64	
Fe-59	2.28E-03
Ga-72	
Mn-54	1.60E-03
Mn-56	
Na-24	
Sb-122	4.46E-03
Sb-124	1.03E-04

LIR2032 (CC01) (LiCoO ₂)	
FNI (Run 2)	Time After Exposure: 85862 sec
Radioisotope	Activity (μCi)
As-76	5.76E-03
Co-58	1.04E-03
Co-60	4.17E-03
Cr-51	
Cu-64	9.63E-01
Fe-59	
Ga-72	2.27E-03
Mn-54	
Mn-56	9.42E+00
Mo-99	1.94E-03
Na-24	1.30E-03
W-187	2.08E-03
LIR2032 (CC01) (LiCoO ₂)	
FNI (Run 2)	Time After Exposure: 944506 sec
Radioisotope	Activity (μCi)
As-76	
Co-58	5.75E-03
Co-60	2.24E-02
Cr-51	2.02E-02
Cu-64	
Fe-59	8.95E-04
Ga-72	
Mn-54	6.19E-04
Mn-56	
Mo-99	
Na-24	
W-187	

LIR2032 (CC01) Orange (LiCoO ₂)	
FNI (Run 2)	Time After Exposure: 252703 sec
Radioisotope	Activity (μCi)
As-76	3.98E-02
Co-58	6.85E-03
Co-60	2.55E-02
Cr-51	2.13E-02
Cu-64	5.33E+00
Fe-59	1.12E-03
Ga-72	4.93E-02
Mn-54	
Mo-99	3.52E-03
Na-24	8.17E-03
W-187	1.18E-02
LIR2032 (CC01) Orange (LiCoO ₂)	
FNI (Run 2)	Time After Exposure: 948416 sec
Radioisotope	Activity (μCi)
As-76	
Co-58	6.61E-03
Co-60	2.49E-02
Cr-51	2.24E-02
Cu-64	
Fe-59	9.56E-04
Ga-72	
Mn-54	5.34E-04
Mo-99	
Na-24	
W-187	

Lithium AA (AA02) (Li-SOCl ₂)	
FNI (Run 2)	Time After Exposure: 94296 sec
Radioisotope	Activity (μCi)
As-76	8.69E-02
Co-58	6.42E-03
Cr-51	1.09E-02
Fe-59	
Ga-72	9.43E-03
Mn-54	
Mn-56	1.35E+01
Mo-99	1.27E-02
Na-24	1.45E-02
Sb-122	
Sb-124	
W-187	4.90E-02
Lithium AA (AA02) (Li-SOCl ₂)	
FNI (Run 2)	Time After Exposure: 950354 sec
Radioisotope	Activity (μCi)
As-76	8.19E-01
Co-58	2.11E-02
Cr-51	4.49E-02
Fe-59	1.82E-03
Ga-72	
Mn-54	1.41E-03
Mn-56	
Mo-99	3.14E-02
Na-24	
Sb-122	9.01E-03
Sb-124	1.96E-04
W-187	

18650 (18650B) (LiMnNiO ₂)	
FNI (Run 2)	Time After Exposure: 96255 sec
Radioisotope	Activity (μCi)
Br-82	2.89E-01
Co-58	1.08E-02
Cu-64	2.21E+01
Fe-59	2.87E-03
Ga-72	1.37E-02
Mn-56	2.63E+00
Na-24	4.40E-02
Te-123m	
18650 (18650B) (LiMnNiO ₂)	
FNI (Run 2)	Time After Exposure: 940255 sec
Radioisotope	Activity (μCi)
Br-82	5.71E-01
Co-58	2.91E-02
Cu-64	
Fe-59	5.45E-03
Ga-72	
Mn-56	
Na-24	
Te-123m	8.34E-04

FNI (Run 1)			
Foil	Radioisotope	Activity (μCi)	Time After Exposure (s)
Nickel (Foil AB)	Co-58	4.77E-03	516150
Iron (Foil AD)	Fe-59	5.09E-05	518180
	Mn-54	2.49E-05	
Magnesium (Foil AI)	Na-24	2.02E-03	350606
Zirconium (Foil AX)	Zr-95	4.93E-04	594144
	Zr-97	1.06E-01	
Indium (Foil A)	In-114m	5.75E-02	1029959
Gold (Foil H)	Au-198	4.43E+00	596363
Copper (Foil L)	Cu-64	7.88E+00	606596
Titanium (Foil V)	Sc-47	2.37E-03	614324
	Sc-48	4.79E-04	

FNI (Run 2)			
Foil	Radioisotope	Activity (μCi)	Time After Exposure (s)
Nickel (Foil AA)	Co-58	7.06E-03	258462
Iron (Foil AF)	Fe-59	6.76E-05	264755
	Mn-54	6.49E-05	
Magnesium (Foil AJ)	Na-24	2.26E-03	336069
Aluminum (Foil AO)	Na-24	1.15E-02	256548
Zirconium (Foil AW)	Zr-95	6.95E-04	332207
	Zr-97	1.20E-01	
Indium (Foil C)	In-114m	5.34E-02	268902
Gold (Foil E)	Au-198	4.14E+00	266855
Copper (Foil I)	Cu-64	6.26E+00	334106
Titanium (Foil Y)	Sc-46	3.74E-05	260345
	Sc-47	3.17E-03	
	Sc-48	4.41E-04	

DEPARTMENT OF DEFENSE

DEFENSE THREAT REDUCTION
AGENCY
8725 JOHN J. KINGMAN ROAD
STOP 6201
FORT BELVOIR, VA 22060
ATTN: D. PETERSEN

DEFENSE TECHNICAL
INFORMATION CENTER
8725 JOHN J. KINGMAN ROAD,
SUITE 0944
FT. BELVOIR, VA 22060-6201
ATTN: DTIC/OCA

**DEPARTMENT OF DEFENSE
CONTRACTORS**

QUANTERION SOLUTIONS, INC.
1680 TEXAS STREET, SE
KIRTLAND AFB, NM 87117-5669
ATTN: DTRIAC